

Electronic Thesis and Dissertation Repository

4-11-2013 12:00 AM

A Variability Study of the Typical Red Supergiant Antares A

Teznie J D Pugh, *The University of Western Ontario*

Supervisor: Dr. D. F. Gray, *The University of Western Ontario*

A thesis submitted in partial fulfillment of the requirements for the Doctor of Philosophy degree in Astronomy

© Teznie J D Pugh 2013

Follow this and additional works at: <https://ir.lib.uwo.ca/etd>



Part of the [Physical Processes Commons](#), and the [Stars, Interstellar Medium and the Galaxy Commons](#)

Recommended Citation

Pugh, Teznie J D, "A Variability Study of the Typical Red Supergiant Antares A" (2013). *Electronic Thesis and Dissertation Repository*. 1190.

<https://ir.lib.uwo.ca/etd/1190>

This Dissertation/Thesis is brought to you for free and open access by Scholarship@Western. It has been accepted for inclusion in Electronic Thesis and Dissertation Repository by an authorized administrator of Scholarship@Western. For more information, please contact wlsadmin@uwo.ca.

A VARIABILITY STUDY OF THE TYPICAL RED SUPERGIANT ANTARES A

(Thesis format: Monograph)

by

Teznie Pugh

Graduate Program in Astronomy

A thesis submitted in partial fulfillment
of the requirements for the degree of
Doctorate of Philosophy

The School of Graduate and Postdoctoral Studies
The University of Western Ontario
London, Ontario, Canada

© Teznie Pugh 2013

Abstract

Red giants and red supergiants have long been known to be variable. In the last 40 years many of the features of this variability have been associated with large convective cells. Unfortunately, due to the long timescales of these variations they are not well studied, with the exception of the bright M-class supergiant Betelgeuse (α Orionis, M2 Iab). Betelgeuse has been well studied both observationally and theoretically, and has many features that are well described by models of convection. It was these studies of Betelgeuse that provided the main motivation for this thesis. We ask if the dramatic motions seen in the atmospheres of Betelgeuse (Gray 2008 amongst others) are typical of red supergiants and if their variations can be described by convective motions as is the case for that enigmatic star.

Sixty-five spectra of the M-class supergiant Antares A (α Scorpii A, M1.5 Iab) were obtained at the Elginfield observatory from April 2008 until July 2010. These data were combined with historical radial velocity measures, Hipparcos photometry, and AAVSO photometry. From these data we determine four scales of variability: ~ 7140 days, 2167 days, ~ 1260 days, and ~ 100 days.

The longest of these periods is found from the AAVSO photometry and cannot be confirmed by any of the other data. A period of similar length has been reported in one previous study but no analysis was completed. A period of this length (~ 7140 days; 19 years) is consistent with suspected rotation rates for red supergiants, though it is also plausible that episodic dust ejection could cause such a variation. The 2167-day variation was found from historical and present radial velocity measures. Due to the shape of the radial velocity curve, and a phase shift compared to the temperature curve, we interpret this period as a pulsation or a long secondary period. The ~ 1260 -day period found from both sets of photometry and the 100-day timescale found from our spectral analysis are both interpreted along with a handful of periods found in the literature as arising from convection.

Keywords

stars: convection - stars: individual (α Sco A) - stars: oscillations - stars: variables: general - techniques: spectroscopic - techniques: radial velocities

Acknowledgments

I would, first of all, like to thank my supervisor, Dr. D. F. Gray for his assistance, for his guidance, for his support, and for his inspiration.

I would also like to thank Michel DeBruyne for his technical support and training at the Elginfield Observatory, without his regular maintenance my observations would not have been possible.

I acknowledge with thanks the variable star observations from the AAVSO International Database contributed by observers worldwide and used in this research.

For their comments and assistance in the interpretation of the data I would like to thank Gregg Wade, Jaymie Matthews and our Astronomical Journal referee. For an explanation of the convective models of Betelgeuse I would like to thank Andrea Chiavassa. Discussions with Jan Cami, John Landstreet and David Stock have also been helpful.

I am grateful for the funding I received through the Western Graduate Research Scholarship, for the financial support of my fiancé Darren, and to the Canadian Astronomical Society for their travel grants.

My acknowledgement would not be complete without thanking the people who have aided me in maintaining my sanity: my fiancé Darren for providing emotional support and taking the lead with parenting so that I could concentrate on my research; my daycare provider Alison for being my daughter's second mum; my family for not making a fuss about my immigration to Canada; and to all my friends for putting up with me through it all and making Canada so welcoming.

Table of Contents

Abstract.....	ii
Acknowledgments.....	iii
Table of Contents.....	iv
List of Tables.....	viii
List of Figures.....	ix
Chapter 1.....	1
1 Red Giants and Supergiants.....	1
1.1 Evolution History.....	3
1.1.1 Intermediate Mass Stars ($2.5M_{\odot}$ to $10M_{\odot}$).....	4
1.1.2 Low Mass Stars ($0.5M_{\odot}$ to $2.3M_{\odot}$).....	5
1.1.3 High Mass Stars ($>10M_{\odot}$ - $15M_{\odot}$).....	7
1.2 Stellar Winds in the Upper HR Diagram.....	8
1.2.1 Driving Mechanisms.....	10
1.3 The Red Variables.....	11
Chapter 2.....	14
2 Observations of Semiregular and Irregular Variables.....	14
2.1 Photometry.....	14
2.1.1 Photometric Power Spectra.....	15
2.1.2 Long Secondary Periods and Multiperiodicity.....	18
2.1.3 Period-Luminosity Relations and Mode of Pulsation.....	19
2.2 Temperature Variations.....	20
2.3 Radial Velocity.....	21
2.4 Interferometry.....	21
2.5 Polarization.....	24

2.6 Spectral Variability	24
2.7 Photospheric Excursions	24
Chapter 3	27
3 Mechanisms of Variability	27
3.1 Companion Stars	27
3.2 Surface Features	28
3.2.1 Starspots	28
3.2.2 Convection Cells	30
3.2.3 Binary Heating & Ellipsoidal Variability	32
3.3 Pulsation	32
3.3.1 Radial Modes	33
3.3.2 Nonradial Modes	34
Chapter 4	38
4 Observations and Reductions	38
4.1 The Equipment	40
4.2 Observational Techniques	41
4.2.1 The Telluric Lines	43
4.2.2 A Night at the Dome	46
4.3 Reductions	47
4.4 Program Star	50
Chapter 5	54
5 The Parameters and Their Measurement	54
5.1 Measuring Granulation	54
5.1.1 Macroturbulence	55
5.1.2 Spectral Line Asymmetries	56
5.1.3 The Third Signature of Stellar Granulation	59

5.2 Predicting Rest Wavelengths.....	61
5.3 Line Positions and Depths.....	66
Chapter 6.....	72
6 Analysis.....	72
6.1 Brightness, Temperature and Radial Velocity.....	72
6.1.1 Brightness Variations	72
6.1.2 The Radial Velocities and Line-Depth Ratios	79
6.1.3 A Six-Year Variation.....	82
6.1.4 A 7140-Day Variation	89
6.1.5 The 1260-Day Variation.....	92
6.1.6 100-200 Day Variations.....	95
6.1.7 Summary.....	103
6.2 The Depth Dependent Velocity and the Third Signature of Antares A	104
6.2.1 The Line-Strength Dependence of the Radial Velocity Curve	104
6.2.2 The Season Mean Third Signature Plot.....	105
6.2.3 The Residual Third Signature Plot	107
6.2.4 Summary.....	110
6.3 Line Shapes	110
6.4 The Significance of Third Signature Reversal	117
6.5 Differences between Antares and Betelgeuse	121
Chapter 7.....	125
7 Conclusion.....	125
7.1 The Variations of Antares A.....	125
7.2 Third-Signature Reversal	127
7.3 Future Work.....	128
Bibliography & References.....	130

Appendices.....	150
Appendix A: The Richardson Image Slicer	150
Appendix B: Fourier analysis of Spectral Lines.....	152
Appendix C: Spectral Line Bisectors.....	156
Curriculum Vitae	159

List of Tables

Table 1: Observational details of the Antares system, with a focus on the primary.	51
Table 2: Absolute wavelengths of non- Fe I lines.	65
Table 3: Mean radial velocities. Errors include seasonal scatter and measurement errors. ..	82
Table 4: Comparison of Orbital solutions.	86
Table 5: Photometric periods between 1000 and 2000 days.	92
Table 6: Photometric periods between 100 and 200 days	96
Table 7: Photospheric velocity spans and mass-loss rates.	119
Table 8: Observational details of Antares and Betelgeuse	122
Table 9: Variability of Antares and Betelgeuse	122

List of Figures

Figure 1: Hertzsprung-Russell diagram.	2
Figure 2: Hertzsprung-Russell diagram showing the regions of hot, cool and coronal winds. 8	
Figure 3: Power spectra of one Mira (R Leo) and two semiregular variables.	16
Figure 4: Smoothed power density spectra in log-log representation.	17
Figure 5: Line-depth ratio plotted as a function of time and AAVSO brightness estimates binned in 10 day intervals for Betelgeuse.....	20
Figure 6: WHT and COAST near-infrared interferometric observations of Betelgeuse.....	23
Figure 7: Line-depth ratio (temperature) is plotted as a function of mean core velocity for Betelgeuse.	25
Figure 8: <i>Top</i> – Schematic diagram of a large star spot showing different epochs of stellar rotation. <i>Bottom</i> – Sample graphs of the luminosity and the stellar radial velocity that coincide with each epoch.	29
Figure 9: Hipparcos light curve of a classical Cepheid using data from Perryman (1997). (Aerts <i>et al.</i> 2010).....	33
Figure 10: Radial motions of the $l=3$ octupole modes. (Fig 1.4 Aerts <i>et al.</i> 2010).....	34
Figure 11: Amplitudes of the radial eigenfunction (FIG 3 Demarque & Guenther 1999). ...	36
Figure 12: The power spectrum of the solar five-minute oscillation..	37
Figure 13: A sketch of the spectrum of Betelgeuse (α Ori) from Secchi (1866).	38
Figure 14: <i>Left</i> – schematic of the 1.2 m telescope of the Elginfield Observatory. <i>Right</i> – picture of the 1.2 m telescope of the Elginfield Observatory.	40
Figure 15: Schematic of a typical spectrograph.	41

Figure 16: Spectrum of the M1.5 supergiant Antares	42
Figure 17: Telluric spectrum.....	44
Figure 18: Cleaning of a cosmic ray hit by the R9 reduction software	47
Figure 19: A typical normalization window.....	49
Figure 20: ELODIE spectra of the M-supergiant Betelgeuse (<i>upper</i>) and the B-dwarf Regulus (<i>lower</i>).....	52
Figure 21: An image of granulation on the solar surface	54
Figure 22: A schematic of granular motions.....	56
Figure 23: <i>Left</i> - Correlation between Doppler shift and line flux of the hot and cool plasma results in an asymmetric spectral line. <i>Right</i> - Asymmetry is more obvious when viewing the bisector of the spectral line.	57
Figure 24: This sample of bisectors demonstrates the changes of asymmetry with spectral type in cool stars.....	59
Figure 25: Sample of four third-signature plots.....	60
Figure 26: Six Fe I line bisectors computed from the mean lines of five exposures of α Ari. Core positions are marked with circles. The typical error on core position is <50 m/s.	63
Figure 27: Bisector core points (<i>circles</i>) from Figure 26 plotted over the Universal curve (<i>solid-line</i>) from Gray (2009).....	63
Figure 28: A bisector from a non-Fe I line taken from one of the five exposures. This bisector is assigned a core velocity using its depth on the Universal Curve.	64
Figure 29: Final third signature plot including Fe I and non-Fe I lines.....	64
Figure 30: Example of core parabola fitting	67
Figure 31: A sample of exposure mean radial velocity measures.....	69

Figure 32: A sample of the core radial velocities for lines of three different depths.	70
Figure 33: Sample of the temporal variations of the line-core flux in the <i>top</i> panel (for the 6241Å line) and the line-depth ratio (6252Å/6253Å) in the <i>bottom</i> panel.	71
Figure 34: AAVSO light curve of Antares A the data are binned in 10-day intervals.	74
Figure 35: Fourier amplitude spectrum of the 10-day binned AAVSO light curve of Antares A.	75
Figure 36: AAVSO data (as Figure 34) shown with the sinusoid corresponding to the 7140-day timescale.	76
Figure 37: Power spectrum after prewhitening of the 7140-day variation.	77
Figure 38: Light curve of Antares A. ▲ - Hipparcos & Tycho magnitudes in 1-day bins. ● - AAVSO magnitude estimates in 10-day bins.	78
Figure 39: AAVSO (●) and Hipparcos (▲) light curves with a 1260-day sinusoid r.	79
Figure 40: Radial velocity curve of Antares during 2008-2010.	80
Figure 41: Line-depth ratios (◆) and radial velocities (●) as a function of Julian Day. The abscissa offset amounts to the minimum temperature occurring 70 days after the minimum in the radial velocity.	82
Figure 42: Mean radial velocities phased to a period of 2167 days.	85
Figure 43: Mean radial velocities as a function of orbital phase.	86
Figure 44: Radial velocity (▲) and AAVSO magnitudes (●) means as a function of Julian Day for three of the four radial velocity data sets.	88
Figure 45: Fourier power spectrum of the AAVSO photometry, prewhitened and focused on the 1260-day peak.	94
Figure 46: Radial velocity residuals as a function of Julian Day.	97

Figure 47: Residuals of the Smith <i>et al.</i> (1989) are shown by the <i>black points</i> . The <i>grey curves</i> are 100-day sinusoids.	98
Figure 48: Fourier power spectrum of the radial velocity residuals from the data of Smith <i>et al.</i> (1989). The main peak occurs at 260 days and is flanked by several smaller peaks.	99
Figure 49: AAVSO binned magnitude estimates (●) and line-depth ratios (▲) as a function of Julian Day.	100
Figure 50: <i>Top</i> – Line-depth ratios measured from 2008 - 2010. <i>Bottom</i> - Hipparcos magnitudes from 1989-1991 (●) and AAVSO magnitudes over the same epoch (○).	101
Figure 51: Line-depth ratio residuals as a function of radial velocity residuals for individual seasons.	102
Figure 52: <i>Left</i> - Mean residual velocities from 2009 as a function of Julian Day. <i>Right</i> – Mean residual velocities from the three strongest lines in the spectrum of Antares.	105
Figure 53: <i>Top</i> - Season mean third-signatures. <i>Bottom</i> – Mean third signature constructed by averaging the core position of lines with similar strengths.	106
Figure 54: Residual third-signature plots.	109
Figure 55: Telluric lines seen in the spectrum of Antares.	111
Figure 56: Spectral lines shifted to negate the radial velocity shifts and scaled to ensure that the 6253Å line is the same depth in all lines.	112
Figure 57: A 7Å window showing two spectra from 2008, 2009, and 2010.	114
Figure 58: A 5Å window showing two spectra from 2008, 2009 and 2010. The dashed line shows the result of convolving the 2008 data with a gaussian with a width of 650 m/s.	115
Figure 59: Third signature of Betelgeuse.	117
Figure 60: Mass-loss rate as a function of third-signature velocity span.	118

Figure 61: A section of the HR diagram from Figure 1. The symbol size represents the third-signature velocity span.120

List of Appendices

Appendix A: The Richardson Image Slicer	150
Appendix B: Fourier Analysis of Spectral Lines	152
Appendix C: Spectral Line Bisectors	156

Chapter 1

1 Red Giants and Supergiants

Red giants and red supergiants are two related groups of stars, both are in the latter stages of their evolution. Figure 1 shows the position of these stars on a Hertzsprung-Russell (HR) diagram. Both groups contain stars cooler than $\sim 5,000^\circ\text{K}$, or K and M spectral class stars, but the members differ greatly in their respective radii and luminosities. Stars within both groups are much larger and much brighter than a main-sequence star of the same mass. The red supergiants fall into luminosity classes Iab-II and the red giants into class III.

Due to the variability demonstrated by essentially all evolved stars, these stars have been collectively termed the red variables – a title that does little to suggest the nature or origin of the variations. They have also been referred to as long period variables owing to the fact that they are variable and have periods considerable longer than most hot stars. As the light variations of these stars were more extensively studied, three classifications of variability were established: Mira type, semiregular and irregular. More recent studies (Kiss & Percy 2012 and references therein) have blurred the boundaries between these groups. Further details regarding the classifications and the variable nature of these stars will follow.

Many of the attributes of these stars arise due their advanced state of evolution, thus the evolutionary history of stars in the upper right of the HR diagram is vital to our understanding. Unfortunately, stellar evolutionary models are fraught with simplifications and inconsistencies with observations. Despite this one sees commonalities in the predictions made by the models; thus, we have some general sense of how stars evolve after the main sequence. These changes are reviewed in the following section.

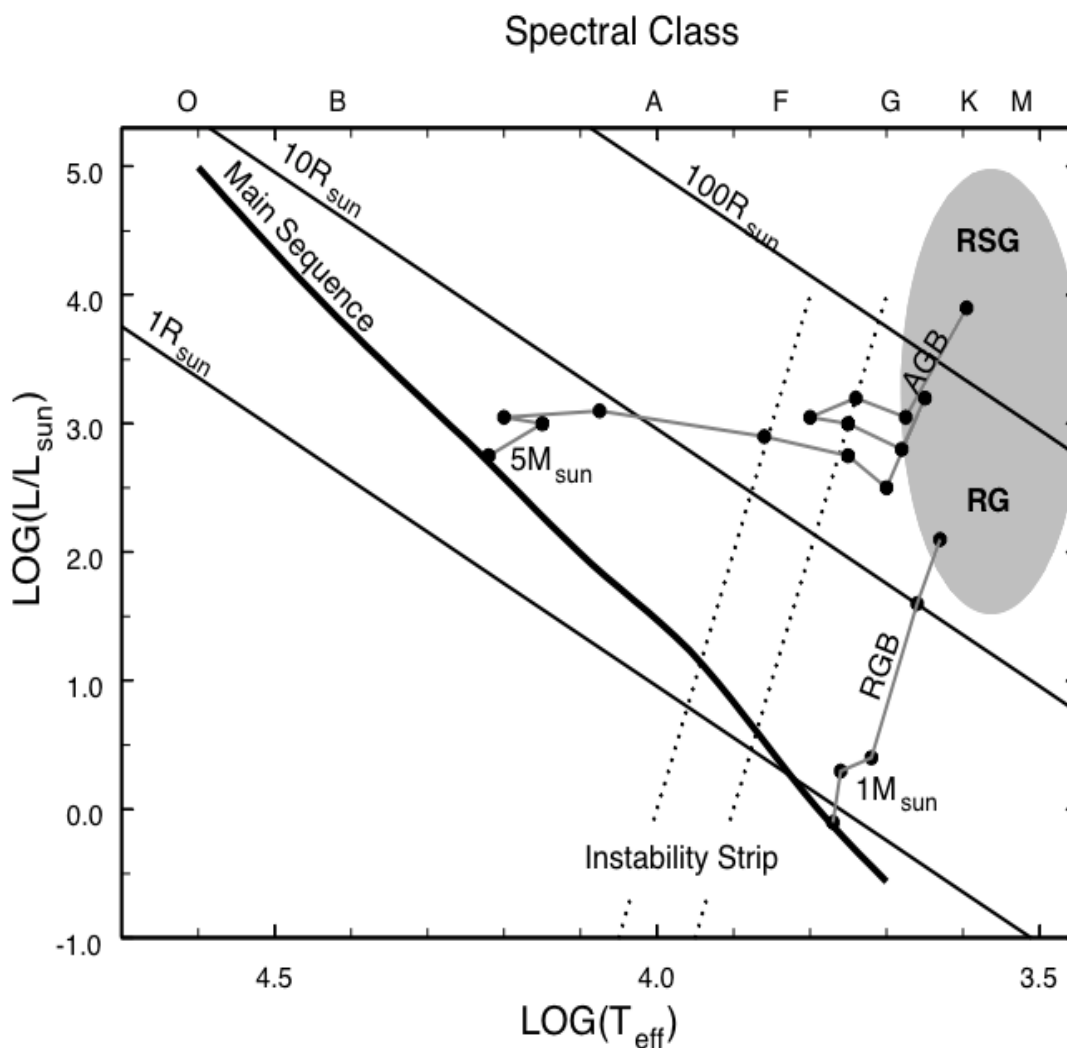


Figure 1: Hertzsprung-Russell diagram. The heavy line indicates the zero-age main sequence. Points from two evolutionary models are shown as black dots (data from Paczynski 1970) with connecting grey lines approximating the evolutionary tracks. The $1 M_{\odot}$ track is truncated at the helium flash (full evolutionary details follow). The region of classical pulsational instability is enclosed by the two dashed lines (approximated from Figure 5.11 LeBlanc 2010). The gray region encompasses the domain of the red variables and incorporates both red giants and red supergiants during their ascent of the red giant branch and/or the asymptotic giant branch.

1.1 Evolution History

In order to understand the nature of red giant and supergiant stars, one needs to understand their origin and their evolutionary history. Red variables are in the late stages of stellar evolution which can result in complicated internal structure. The offset and onset of various core fusion processes results in fusion taking place in shells above the core (for further details see the sections that follow). This arrangement is pulsationally and thermally unstable; a number of variable phenomena are associated with such shells, for example pulsation in Mira-variables (Ulmschneider 1998) and thermal pulses during very advanced stages of evolution (Aerts *et al.* 2010). Additionally, the depth of the outer-most shell will limit the depth of the convective envelope, since this shell will move outward over time the scale of convection will change for stars at different stages of their evolution (Kippenhaun & Wiegert 1994). Most importantly it is the highly evolved states of these stars that results in their large radii, large luminosities and low surface gravities: when considering the physics underlying their variability these factors must be kept in consideration. In the following sections we will review the details of stellar evolutionary models for stars of various masses that ultimately result in red giants and red supergiant stars.

In Figure 1 the zero-age main sequence is indicated by the heavy line, two evolutionary tracks are shown originating at the main-sequence and tracking rightward and/or vertically across the Hertzsprung-Russell (HR) diagram. The almost vertical branches of these evolutionary tracks are the Red Giant Branch (RGB) and the Asymptotic Giant Branch (AGB). During their evolutionary progression across the HR diagram all but the most and least massive stars ($0.5M_{\odot} < M_{*} < 10-15M_{\odot}$) will spend some time on one or both of the giant branches.

Let us consider a typical star: it will begin its life on the main-sequence, fusing hydrogen at its core. During its main-sequence lifetime it will evolve slowly due to the build-up of helium in the core. As the abundance of helium within the core increases we eventually reach a point where the core is considered hydrogen deficient. Hydrogen deficiency occurs, typically, after 10^6 years for an O-type star up to 10^{14} years for a low-mass M-

dwarf (Hansen & Kawaler 1994). From this point on the evolution is considerably different for stars of differing mass; thus we consider three groups, stars with a mass greater than $10\text{-}15M_{\odot}$, stars with a mass between $\sim 3M_{\odot}$ and $\sim 10M_{\odot}$, and stars with mass less than $\sim 3M_{\odot}$. [Most values given here are taken from Kippenhaun & Weigert (1994), and while typical are by no means absolute, see Iben (1974) for other examples].

1.1.1 Intermediate Mass Stars ($2.5M_{\odot}$ to $10M_{\odot}$)

When the stellar core is too deficient in hydrogen to continue fusing, the star has an inert helium core surrounded by a hydrogen-rich shell that is fusing hydrogen at its base (Ryan & Norton 2010). The increase in molecular mass, resulting from the hydrogen fusion above the core causes the core to contract. Energy released by this contraction prevents the core from becoming isothermal and the low initial central density means that the contraction is insufficient to cause degeneracy. The core heats and eventually helium is ignited. This entire period lasts only $\sim 10^5$ years, during which time the stellar radius increases by ~ 25 times. These stars have reached the red-giant region of the HR diagram, a star climbs the RGB before settling into stable core helium burning for $\sim 10^7$ years, during this period the star moves slowly leftward on the HR diagram until the core helium content is $\sim 25\%$ when it moves rightward again.

This phase in stellar evolution is crucial in explaining the existence of the classical δ Cephei type variables. The first crossing of the HR diagram occurs during helium core collapse, this phase is very short and we are thus unlikely to see stars during this crossing, this leads to the well-known Hertzsprung gap. Thus, the evolutionary loops account for the occurrence of these yellow (spectral class G-K) giants and bright giants.

Evolutionary models, like those shown in Figure 1, place a lower mass estimate on the Cepheid variables of $\sim 5M_{\odot}$ (Wallerstein 2002).

The extent of the loops depends upon the stellar mass, for stars lower than $\sim 5M_{\odot}$ there is essentially no loop and the star first ascends and then descends the RGB before ascending the AGB. Helium core burning will terminate when the helium is substantially processed

into an ‘ash’ of carbon, oxygen and neon. Helium burning continues, in a shell around this core, as this shell burns outward the core accretes mass. The hydrogen burning shell is extinguished due to its temperature falling as it moves outward through the star. With this shell extinguished the outer envelope expands dramatically and the stellar luminosity increases strongly, a counterintuitive result caused by the interaction between the two fusing shells (Kippenhaun & Wiegert 1994). Eventually, the combination of the outward progression of the helium burning shell and the deepening of the lower convection boundary results in the re-ignition of the hydrogen burning shell.

Further loops are possible for stars with sufficient mass in which internal contraction will raise the temperature enough to allow ignition of heavier elements. Each successive loop will have successively shorter life-time and each will return the star to the AGB. If the core becomes degenerate before the next ignition temperature is reached then the star may undergo a carbon, oxygen, silicon or neon flash (see below for details regarding the helium flash and post flash evolution) before settling on the AGB and forming a heavy white dwarf. Further evolution, beyond the AGB, is beyond the scope of this work but details may be found in Kippenhaun & Wiegert (1994).

While on the AGB most stars will become pulsationally unstable and will undergo large amplitude radial pulsation. Many red variables stem from these stars during their ascent of the AGB, Miras and some types semiregular variables belong to this evolutionary group. It is not uncommon for Mira variables in the late stages of AGB evolution to have emission lines in their spectra. These emission lines arise due to atmospheric heating caused by the shocks that result from the interaction of pulsation and convection (Freytag & Hoefner 2008).

1.1.2 Low Mass Stars ($0.5M_{\odot}$ to $2.3M_{\odot}$)

The evolution of low mass stars is quite different than the evolution outlined above for intermediate mass stars, for such stars degeneracy becomes important. In these stars the hydrogen shell burning, above an inert helium core, is a slow and stable process and we

do see stars in this phase. The energy produced in the hydrogen burning shell causes the outer layers of the star to expand, the star is limited in its redward progression (or cooling) and thus the expansion is instead accompanied by a huge increase in luminosity, often by as much as a factor of 100. As the star climbs the RGB the core continues to contract and eventually the temperature is sufficient to ignite helium fusion.

The degeneracy of the stellar core has an important effect, termed the Helium flash. Degeneracy pressure supports the core and the star experiences nuclear runaway: the core temperature increases rapidly while the central density remains constant. As the central temperature continues to increase the degeneracy is lifted and thermal pressure begins to dominate the core. The core can now cool to 'normal' helium fusing temperatures and settles into stable helium burning on the horizontal branch. While on the horizontal branch the hydrogen burning shell deposits helium onto the helium burning core. During this phase of evolution some of the stars will cross into the instability strip, these are the W Virginis stars (Wallerstein 2002). Helium is consumed in the core and carbon and oxygen are produced. In the same way that the build-up of a central helium 'ash' ended the main-sequence, now a build-up of a carbon-oxygen 'ash' ends the horizontal branch. Nuclear burning now takes place in two shells, the star approaches its Hayashi limit and begins to climb the AGB. As the star climbs the AGB the two shells burn outward, the hydrogen shell ceases burning and later begins again as it is heated from below by the encroaching helium burning shell. The star continues to expand and has a white dwarf slowly forming at its core.

The stars considered in this thesis are of higher mass than the stars in this group, though these low mass stars do ascend the HR diagram resulting in AGB stars. Many red variables (Mira variables and M-giant semi regular variables) are evolved, AGB stars of the type outlined above.

1.1.3 High Mass Stars ($>10M_{\odot}$ - $15M_{\odot}$)

In this regime we run into the problem that theoretical evolutionary models have experienced a lot of difficulty in explaining the observed positions of stars on the HR diagram. The extreme mass-loss rates these stars experience at the various stages of their evolution (Massey 2003) makes modeling difficult, combine this with uncertainties surrounding core convection and interior mixing and the difficulty becomes extreme. Similar to the less massive stars they will inevitably reach a state of hydrogen deficiency in their cores, leading to hydrogen shell burning and a shifting of the convective zone. As before the helium build up in the inert core causes the temperature to rise until helium burning begins, as for intermediate mass stars this is a short evolutionary phase. Due to the nature of the processes in these stars, which are as of yet not fully understood, only the least massive (that is $15M_{\odot}$ - $40M_{\odot}$) ever become red supergiants (Humphreys & Davidson 1979). For details regarding the evolution of the extremely massive stars see Meynet *et al.* (2011) and Maeder & Meynet (2012).

The red supergiant phase is relatively short ($\sim 100,000$ years) and these stars will eventually either explode as hydrogen-rich supernovae or, due to their substantial mass-loss, evolve blueward once more giving rise to yellow hypergiants, high-mass cepheids, blue supergiants, Wolf-Rayet stars, and/or luminous blue variables. Some of these stars will return briefly to the red supergiant phase before their dramatic climax (Smartt *et al.* 2008), while others will result in their supernovae while still in their hot blue phases (Meynet *et al.* 2011). Rarely, the most massive red supergiants will later result in the least massive Wolf-Rayet stars.

The star that is the primary consideration of this thesis, Antares A and its close comparison star Betelgeuse are both red supergiants. The importance of stellar evolution lays in this fact, since the similarities and differences between Antares, Betelgeuse and other red variables could trace their physical origins back to their internal differences due to their different evolutionary backgrounds.

1.2 Stellar Winds in the Upper HR Diagram

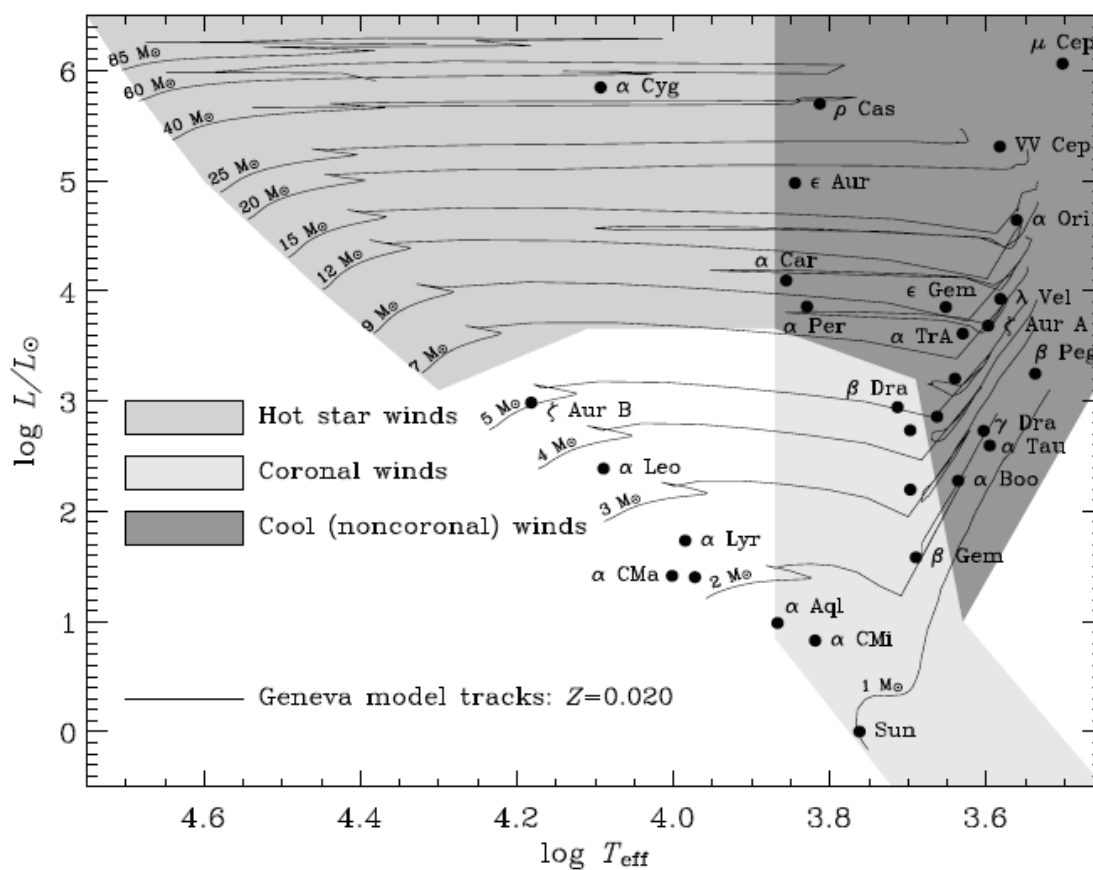


Figure 2: Hertzsprung-Russell diagram showing the regions of hot, cool and coronal winds. The line separating coronal winds from cool winds is known as the Linsky & Haisch dividing line, it occurs at approximately spectral class K1 for giants and F0. (Bennett 2010).

For many red giants and supergiants mass-loss rates are extreme ($\sim 10^{-6} M_{\odot} \text{ yr}^{-1}$; de Jager *et al.* 1988) and each stage of their evolution is governed by this mass-loss, further the total mass lost during any one part of their evolution affects their advancement through the following stage (Mauron & Josselin 2011). Also, RGB stars, AGB stars and red supergiants all undergo mass-loss, however a well-understood mechanism exists only for dusty variables (i.e. Mira variables and OH/IR stars). The interaction, if any, between

stellar winds and photospheric dynamics is not fully understood. All of the proposed mechanisms of wind driving in red variables (outlined below) should cause a dynamical effect in the photosphere. If, for example, they are pulsationally driven then the pulsation velocity will be detectable in the photospheric dynamics even though the wind itself does not originate there. As observers we should be aware of the expected mechanisms as much as theoreticians should be aware of the measured velocity scales.

In the upper portion of the HR diagram two types of wind dominate the observations: hot winds and cool winds. Figure 2 shows the Linksy & Haisch (1979) dividing line, which separates hot winds from cool winds on the HR diagram. In this figure coronal winds are also included and though some evolved stars are found to have corona those under consideration here do not. Betelgeuse (α Ori) can be seen in the upper-right of Figure 2 and Antares falls in approximately the same location on the HR diagram. Stars hotter than spectral-type B3 (on the main-sequence this translates to $M > 6 M_{\odot}$) undergo significant mass-loss due to their high-velocity winds. In these stars, radiation pressure from mid-UV photons on high-opacity metal lines above the photosphere dominates the momentum (Castor *et al.* 1975).

Winds in cool-evolved stars have been measured since the second half of the 20th century (Deutsch 1956). The winds of these stars are low velocity (20-50 km/s) but still cause considerable mass-loss, at present no single mechanism successfully explains the observations (Judge & Stencel 1991, Bennett 2010). Mass-loss rates vary across the upper HR diagram: line-driven hot winds reach their maximum for hot O stars and cool winds reach their maximum in the extremely cool red supergiants (see the data presented by de Jager *et al.* 1988 or more recently Figure 8 of Cranmer & Saar 2011). The lowest mass-loss rates occur between late A and early G spectral types. However, due to differences in evolutionary age, initial mass, multiplicity and so on, the actual cut-off from one regime to another is not well defined. Additionally, both high-mass stars and AGB stars undergo mass-loss events via ejection. Luminous blue variables (or S Dor stars) are known to undergo massive ejection events throughout their lifetimes, such as the 19th Century eruption of η Carina discussed by Rest *et al.* (2012). Mira variables are also seen to undergo eruptive events detectable mainly through radio and H_{α} emission

(Etoka & Le Squeren 1997). Photometric flare events of order tenths of magnitudes (Mais *et al.* 2004) have also been reported for several dozen Mira variables.

1.2.1 Driving Mechanisms

It is widely accepted that the winds of hot stars are driven by UV-photon momentum transfer to high opacity metal lines (Castor *et al.* 1975). For cool stars, coronal winds are thought to be driven by Alfvén waves (Cranmer & Saar 2011), whereas no single mechanism is accepted as the cause of noncoronal winds. Some success has been had in modeling the dusty winds of Miras and OH/IR stars (Bowen 1988; Bowen & Willson 1991) but for dust-free corona-free stars there is still no real consensus. It remains useful to review the findings for Miras, since they represent a close evolutionary analogue to the semiregular variables, and to discuss the other possible driving mechanisms.

Dust Opacity - radiation pressure on the dust grains around red giants and supergiants has been popular as a proposed mechanism for the large winds that these stars demonstrate (Hofner 2008). Dust grain opacity peaks in the infrared, the same region as the stellar spectrum, strengthening the argument. However, both dust-free AGB & RGB stars and the majority of red supergiants have low opacity winds. Further, in those supergiants where dust is detected it is generally beyond the wind radius: Bester *et al.* (1996) report a dust shell around Betelgeuse (α Orionis; M2Iab) at a distance of $\sim 30R_*$, which lies well beyond the wind radius found empirically by Harper *et al.* (2001). Although dust opacity is often cited as the cause of strong winds around Miras, OH/IR stars and other dusty AGB stars, modeling suggests that while the dust facilitates the mass-loss it is initiated by pulsation lifting the stellar atmosphere (Bowen 1988; Bowen & Willson 1991).

Pulsation – as mentioned above, pulsation as a mechanism for material to escape the stellar gravitational potential has been successful in modeling the winds of Mira variables. In these stars the mass-loss is augmented further by radiation pressure on dust grains. Interestingly, the models of Bowen & Willson (1991) also developed high mass-

loss rates for stars when the pressure-scale heights became large, even in the regime of no dust. Thus, we see that if the surface gravity is low then strong winds can develop. It has been argued that the smaller pulsation amplitudes in red supergiants make this simulation implausible (e.g Josselin & Plez 2007).

Alfvén Waves - magnetic waves have been proposed as a chromospheric heating mechanism and thus an energy transfer mechanism for these cool wind stars (Schroder & Cuntz, 2007) due to their large damping lengths. However, these waves couple to ionized gas, whereas the cool winds of K and M supergiants are neutral. Thus, momentum and energy transfer via this mechanism would be extremely inefficient.

Acoustic Waves - convection in cool stars drives atmospheric turbulence and acoustic waves, some of which will penetrate the higher atmospheric layers. On the whole models show that while short period acoustic waves in the Sun can efficiently heat the chromosphere they are unlikely to drive the stellar winds (Athay & White 1978; Hartmann & MacGregor 1980; Cuntz 1990). However, the nature of convection in red supergiant stars is quite extreme (Gray 2008 amongst others) and, although short period acoustic waves may not be sufficient to drive their winds the thermal and kinetic energy imparted on the atmosphere by the convection cells directly likely has a much larger impact.

1.3 The Red Variables

As was previously mentioned, at various points throughout a stars evolution it may experience times of variability. During horizontal branch evolution some low-mass stars will cross into the instability strip, these are observed as either RR Lyrae variables (for further reading see Smith 1995) or W Virginis stars (for further reading see Wallerstein 2002). Similarly, the evolutionary looping of intermediate mass stars causes them to pass through the instability strip, giving rise to the classical Cepheid variables (see Wallerstein 2002). It is however the red variables that are of interest to this thesis. Unfortunately, given the evolutionary state of these stars their physical parameters (initial mass, mass,

metallicity and so on) are wildly different and thus assigning an evolutionary phase to any individual red giant or red supergiant is not trivial. Instead when considering these stars we consider these stars in terms of the nature of their variability.

Long period variable stars are stars in which brightness variations occur over many months or years, here we use this term in its broadest sense, that is in referring to all luminous red variables, however some literature uses this term to apply to the Mira-variables only. Typically these stars are of luminosity class III or brighter, and of spectral class F and cooler. The General Catalogue of Variable Stars (GCVS, Samus *et al.* 2012) lists three categories of red variables: Mira variables (M), Semi-regular variables (SR), and Slow Irregular variables (L). These classifications are discussed below.

Mira Variables – The GCVS (Samus *et al.* 2012) gives three distinguishing characteristics for these stars: Their periods are typically between 80 and 1,000 days. They are of spectral types Me, Ce, or Se indicating low effective temperature and emission features, likely from atmospheric shocks typical of the later stages of AGB evolution. The amplitudes of their light curves fall between 2.5 to 11 mag in V, though the bolometric magnitude variation is ~ 1 mag (Willson & Marengo 2012). Thus the bolometric luminosities increase by approximately a factor of 2. The large optical amplitudes arise from large variations in the opacity over a pulsation cycle. These stars are late-AGB stars typically of low mass ($< 2M_{\odot}$), they are radial pulsators, however, identifying the mode of pulsation, that is fundamental mode or overtone pulsation, of these variables has been difficult (Wood 1995 gives details pertaining to this problem and reviews the observational and theoretical evidence). Fundamental mode pulsation is favoured.

Semiregular Variables – In the GCVS (Samus *et al.* 2012) this class of stars encompasses several group of stars and thus is further classified. However, they all display some common features: they are giants and supergiants that are of intermediate-to-late spectral-types, and demonstrate notable variability. These stars are subcategorized as follows:

SRa – these stars are small amplitude Mira variables, as such they have periods that are fall into the same range as those of Mira variables but have visual magnitudes <2.5 mag. The classification of these stars as semiregular variables rather than Miras seems to be based solely on their visual amplitudes (Kerschbaum & Hron 1992).

SRb – SRb stars are also evolved giants but have smaller amplitudes than SRa stars and poorly defined periods, typically between 20 and 2300 days. These stars often vary between periodic and irregular and in some cases are multiperiodic.

SRc – these are small amplitude (<1 mag), semi-periodic evolved supergiants with periods similar to those of SRa and SRb variables.

SRd – these are weak-lined, F, G, and K giants and supergiants. They are considered to be a metal poor, short period analogues (<1100 days) of Miras (Lloyd Evans 1975). They have visual amplitude of ≤ 4 mag.

These categories seem somewhat arbitrary, being based solely on the amplitude of the variation and the spectral and/or luminosity classification. Only two of these classifications appear to be truly semiregular with the other two falling into this group based solely on them being *not* Miras. The group of importance to this thesis is the SRc variables which is mostly comprised of M class supergiants; in fact the well-studied supergiant Betelegeuse is classified as an SRc variable.

Slow Irregular Variables – These stars have light curves that are highly chaotic and that show little to no periodicity. Similar to the semiregulars these stars are further grouped depending on their luminosity class: Lb designating the giants and Lc designating the supergiants. Many stars within this group are classified as such simply due to lack of observation, thus the true nature of the variability is not known and many are likely semiregular stars with few observations. Antares A is classified as an Lc variable in the GCVS (Samus *et al.* 2012).

Chapter 2

2 Observations of Semiregular and Irregular Variables

Despite their differing classification, semiregular and irregular variables share many physical traits and thus in this section we will consider these stars simultaneously. Here we will see how many of the observed features of these stars cannot be satisfactorily explained by radial pulsation. A star becomes known as a variable if its apparent brightness changes over time, with most stars displaying at least some variability. α Ceti (Mira) was the first star for which variability was recorded, in 1596 Fabricius noted the appearance and disappearance of this star while monitoring Mercury. This was followed by the discovery of, the S Dor variable, P Cygni in 1600. In the following 200 years a further 13 variable stars were recorded, 8 of these 15 are now considered red variables by spectral type. The most recent edition of the GCVS (Samus *et al.* 2012) lists >40,000 variable stars in the Milky Way, the majority of which are red variables.

2.1 Photometry

Light curve analysis has been the principal method for period estimation in these stars for more than 50 years (e.g. Payne-Gaposchkin 1954, Fredrick 1960a & 1960b, Stothers & Leung 1971) and such photometry has played a critical role in our understanding of red variables. Detailed studies of the light curves of red variables have shown some interesting results: Mira-variables have regular, periodic lightcurves, but even the cleanest examples have some irregularity superimposed. Similarly, semiregular variables appear mostly irregular although a characteristic timescale of variation can be identified (Mattei 1983).

For a convincing physical interpretation of the variability to be made, quality observational material is required. As stated above, the light changes in these red variables typically occur with periods between 20 and several thousand days. In the case of red supergiants, such as Antares A, several thousand day variations are more common.

Such long timescales make it difficult to obtain well-sampled light curves, this is especially problematic for semiregular and irregular variables which demonstrate erratic variations. Hence, only a small number of good, long and well-sampled light curves have been published, and in the past many of the published pulsation parameters were questionable, an issue highlighted by Lebzelter *et al.* (1995). However, in recent years, visual magnitude estimates made by amateur astronomers have been made available electronically through archives such as that maintained by the American Association of Variable Star Observers (AAVSO). While the quality of individual measurements within the database is low, the power of this data lies in its unprecedented coverage (see Percy & Mattei 1993). In fact, several studies of red variables are based on such data (e.g. Mattei *et al.* 1997; Kiss *et al.* 1999, 2000, 2006). In Chapter 6 we present the AAVSO light curve of Antares and use these data to study the photometric variations.

2.1.1 Photometric Power Spectra

Fourier power/amplitude spectra of time variable data provide a wealth of information about the nature of the variability. The peak positions tell us directly the frequency of any oscillation and the sharpness gives information about the phase stability and/or the duration of the observations. Stars undergoing regular, radial pulsations have sharp peaks, like that of the Mira variable R Leo (Bedding 2003) shown in the upper panel of Figure 3. In the past decade, numerous examples of photometric periodograms have shown (see the lower two panels of Figure 3 for example) that peaks in the power spectra of semiregular variables closely resemble the power peaks associated with the solar 5-minute oscillation (Bedding *et al.* 2003, Kiss *et al.* 2006). Such similarity is suggestive of a similarity in the underlying mechanism, that is convection (or granulation) driven variations. With the new era of high precision photometry, from telescopes such as MOST, KEPLER, and CoRoT, 1000s of red giants have been identified as demonstrating such behavior (Huber *et al.* 2011).

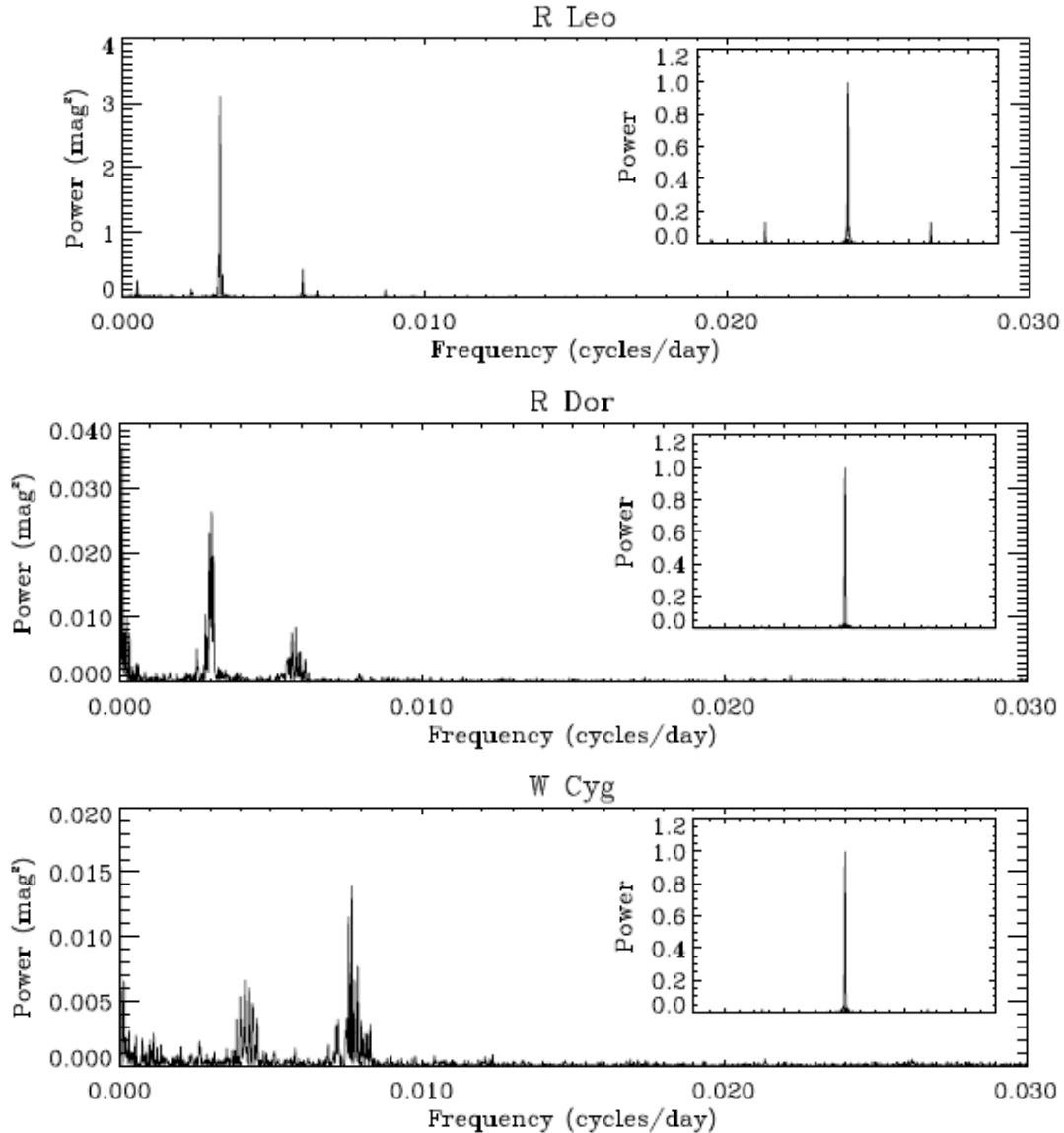


Figure 3: Power spectra of one Mira (R Leo) and two semiregular variables. The plots demonstrate the differences between the power peaks of an opacity-driven radial pulsation compared to stochastically driven oscillations. The inset panels show the window functions for each data set. Panels taken from figure 4 of Bedding (2003).

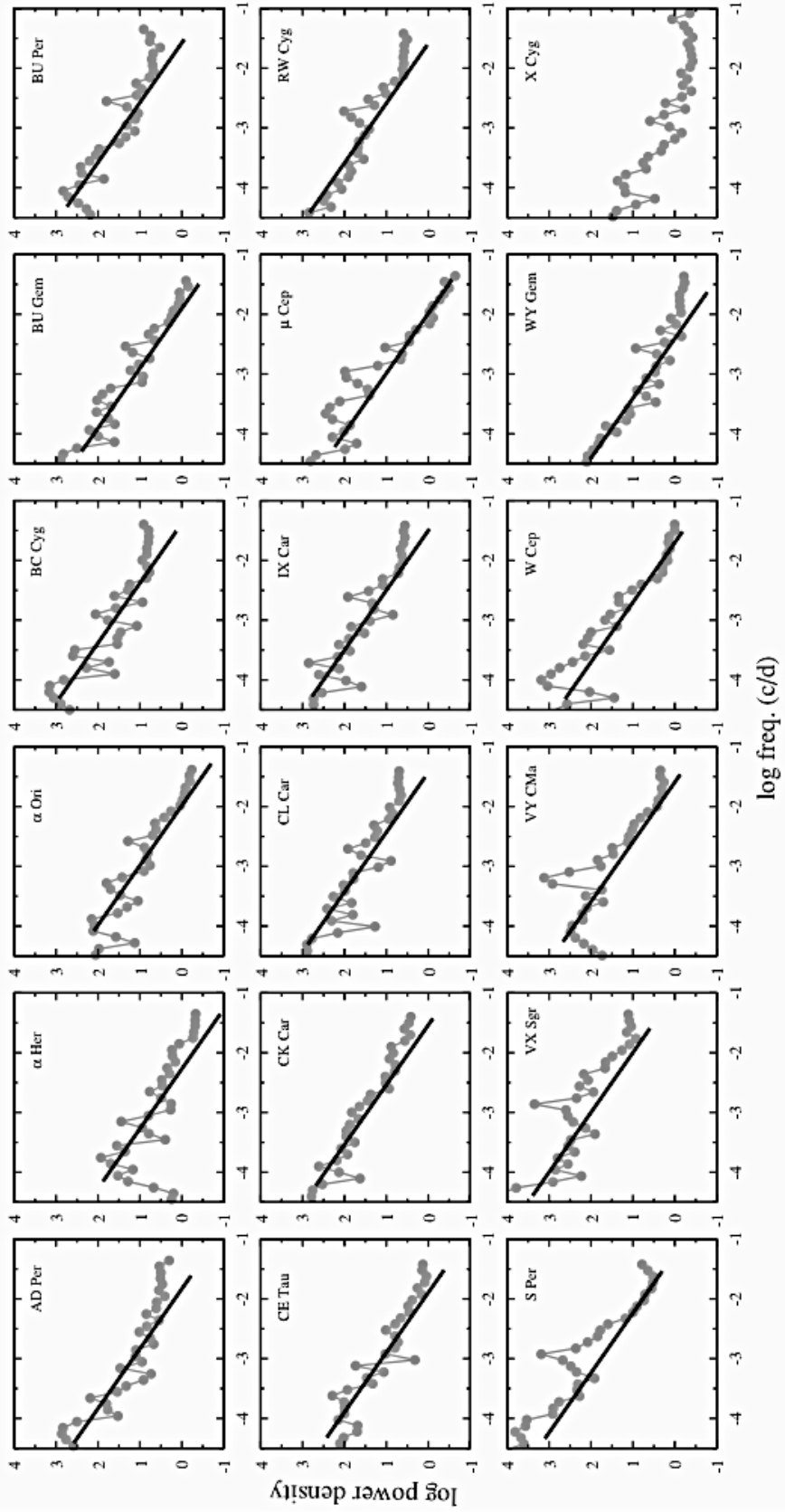


Figure 4: Smoothed power density spectra in log-log representation. The thick line shows the best-fit $1/f$ noise. For comparison the lower right panel shows the case of the Cepheid variable X Cyg. (Figure 10 of Kiss *et al.* 2006)

The physical nature of the variations can also be investigated through studying the shape of the power density spectrum. The analysis of fluctuations in power density spectra is a common tool in studies of unpredictable and seemingly aperiodic variability, that is, noise that arises from stochastic processes. In this context, the noise is intrinsic to the source and not a result of measurement error. Kiss *et al.* (2006) studied the power density spectra of a number of red variables. Figure 4 shows the close similarity in the log-log slope; Kiss and collaborators concluded that there is a universal scaling behavior in the brightness fluctuations. Yet again these results are similar to results found for the solar-granulation background (Rabello-Soares *et al.* 1997) and are even expected to arise from convection. For further details of the phenomenon of $1/f$ noise the reader is directed to the papers of Bak *et al.* (1988) and Press (1978).

2.1.2 Long Secondary Periods and Multiperiodicity

Long secondary periods are seen in the light curves of many semiregular variable stars (Houk 1963) these periods are of the order 500-2000 days (some 5-15 times the primary period). In the Large Magellanic Cloud (LMC) some 25% of semiregular variables have been found to show such periods (Wood *et al.* 1999). Multiperiodicity has also been reported in a number of investigations (e.g. Kiss *et al.* 1999) suggesting that the visual light changes may be described with the coupling of two or three excited periods. The use of the Fourier amplitude spectra allows for the selection of many periods, and this can improve the fit of the light curves. However, a physical explanation for a large number of periods seems unlikely. The very longest periods found are unlikely to be due to pulsation (see Wood 2000), however the shorter periods could represent different modes of pulsation. To-date no single mechanism has been accepted as the cause of multiperiodicity, though a number of suggested causes are to be found in the literature: the possible explanations include orbital dynamics, radial pulsation, rotation combined with surface irregularities, and episodic dust ejection. In recent years non-radial pulsation has gained more support than the other proposals (Olivier & Wood 2003), though it is also suggested that an as yet unknown pulsation mechanism is required to explain the observations (Nicholls *et al.* 2009). There are some cases where binarity has

had success in explaining an observed long secondary period – in particular for the RVb type variables (RV Tauri stars with long secondary periods) it is binarity that produces the long secondary period (Maas *et al.* 2002 and Van Winkle *et al.* 1999 amongst others).

2.1.3 Period-Luminosity Relations and Mode of Pulsation

Interest in semiregular variables was driven by the hunt for a period-luminosity relations similar to those seen for classical Cepheids and Mira variables. The large intrinsic brightness of semiregular variables makes them desirable as distance indicators. Wood *et al.* (1999) presented five different period-luminosity sequences for the LMC red variables based on the MACHO photometric database and they found that the third and even fourth overtones could be the dominant excited modes. A detailed review given by Percy & Parkes (1998) draws similar conclusions. Following the results shown for LMC red variables Kiss *et al.* (2006) investigated the long secondary period phenomenon in a selection of red supergiant stars including Antares and Betelgeuse. The work of Kiss and collaborators suggests that galactic red supergiants may follow period-luminosity relations that are an extension of those seen for less luminous red variables in the LMC. In this case one sees, usually, two period-luminosity relations one for a short (or primary) period of radial pulsation (~ 300 -400 days) and one for the long secondary period (≥ 1000 days).

Further, Bedding *et al.* (1998) reportedly observed mode switching in R Dor and claim that it occurs between the first and third overtones. Mode switching has been reported in other semi-regular variable stars (Cadmus *et al.* 1991; Percy & Desjardins 1996; Kiss *et al.* 2000) and in conjunction with multiperiodicity (Kiss *et al.* 1999; Percy *et al.* 2001) and the studies of semi-regular variables in the Magellanic Clouds (Wood *et al.* 1999; Wood 2000) the idea that the light variations seen in semi-regular variables may be due to many simultaneously excited modes seems increasingly attractive. However, the mode of pulsation of these stars is still a matter of some debate and even the cleanest examples of multiple period semi-regulars exhibit additional irregularity in their light curves (Kerschbaum *et al.* 2001; Lebzelter & Kiss 2001). Thus, multimode pulsation with a

stationary frequency and amplitude content cannot fully explain the light variations that are observed.

2.2 Temperature Variations

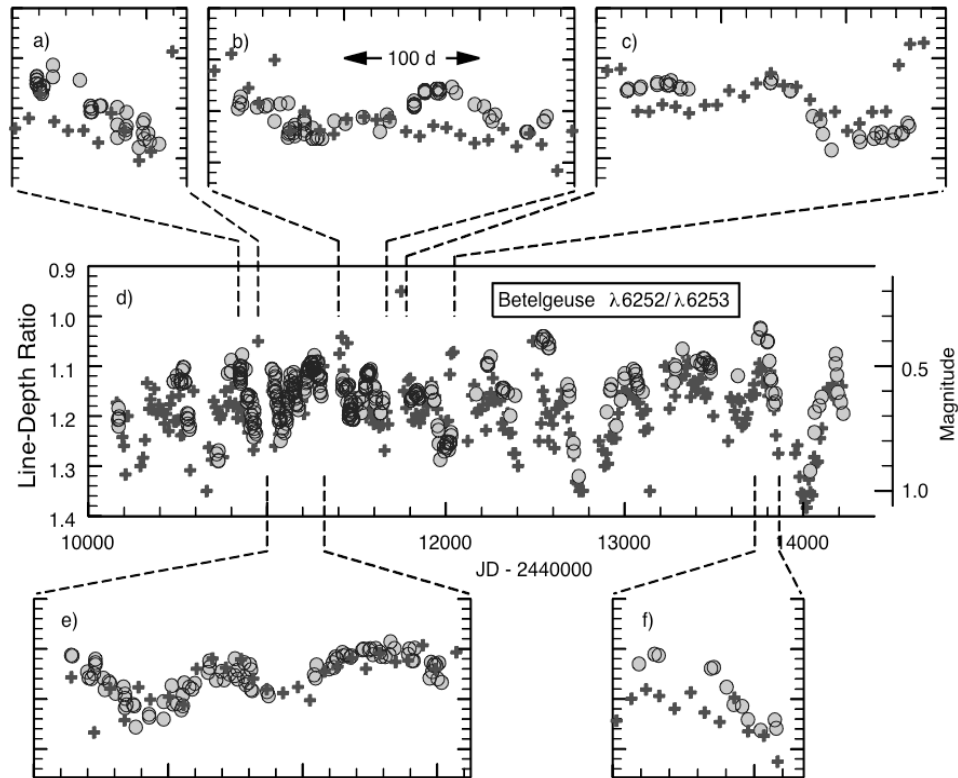


Figure 5: Line-depth ratio plotted as a function of time (O) and AAVSO brightness estimates binned in 10 day intervals (+) for Betelgeuse. Temperature and brightness maxima often agree but occasionally there is an excess of one or the other. (Gray 2008)

Radial pulsation shows a ratio between the light variation and the color variation that is a constant function for any given star. However, in a selection of AGB stars Kerschbaum *et al.* (2001) found some light phases to be accompanied by strong color changes while

others showed very little variation. Interpreting the color value as an indication of the temperature, this implies that light change is observed even during times of constant temperature. Additionally, by comparing the line-depth ratio (temperature index, see Gray & Brown 2001) and brightness variations over the same period, Gray (2008) found that the temperature variations of Betelgeuse did not account for all the observed brightness variation, see Figure 5. These observations suggest that radial pulsation alone cannot account for the observed variation of the brightness of these stars.

2.3 Radial Velocity

Studies of short-term (~200 days) radial velocity variability in semiregular variables (Lebzelter *et al.* 2000; Lebzelter & Hinkle 2002) show radial velocity curves with minima that occur very near maximum light, a behavior typical of radial pulsators (see for example. Bersier *et al.* 1994a, 1994b). This suggests that the light variations are dominated by radial pulsations. However, “jitter”, or excess irregularity in the radial-velocities of stars at the tip of the red giant branch has been seen repeatedly (Gunn & Griffin 1979; Pryor *et al.* 1988; Carney *et al.* 2003, among others). Many of these studies have found jitter to be concentrated to the most luminous of the target stars. Currently, the leading candidates for the cause of the jitter are: (i) some form of modulation (see Carney *et al.* 2003) added to the photometric variability, and (ii) giant convective cells (Gray *et al.* 2008; Eaton *et al.* 2008). The idea of time-variable dark or bright regions seems probable in either case.

2.4 Interferometry

Hot/bright spots on the surfaces of a handful of M-type supergiants have been seen in interferometric studies for many years (Buscher *et al.* 1990; Wilson *et al.* 1992; Tuthill *et al.* 1997; Young *et al.* 2000). However, the cause of these hotspots has been the source of some conjecture with various suggestions of their origin being made: including the presence of companions, effects arising from rotation, magnetic activity, radial and non-

radial pulsation, and transient convective cells on the stellar surface. Studies of the evolution of these features gives insight into the physical mechanisms behind them, as well as some of the other variable features of such stars. Freytag *et al.* (2002) presented a short overview of observations of such hotspots (data for the figure taken from Buscher *et al.* 1990; Wilson *et al.* 1992; Tuthill *et al.* 1997; Wilson *et al.* 1997; Klueckers *et al.* 1997; Burns *et al.* 1997; Young *et al.* 2000), as seen in Figure 6.

The figure produced by Freytag *et al.* (2002) shows quite clearly the evolution of these bright spots as well as their often multiple nature. Changes in spot number and position are observed on timescales of years; such evolutionary timescales should not be expected for a multiple system. For example, take VV Cephei a well known red supergiant with a hot companion star: a system with a period of 7430 days (or approximately 20 years). Thus, hotspots due to companion transits seem unlikely for similarly large stars. However, interactions of the primary star with companions cannot be ruled out as chromospheric heating is known to occur in binary systems (e.g. Eaton *et al.* 2008). Similarly, rapid spot evolution also makes a rotational mechanism seem highly unlikely. Again if we consider an example, derived rotation velocities for Betelgeuse are typically ~ 5 km/s (Gray 2000 for example) resulting in a rotation period ~ 20 years. Not all such stars will have rotational periods this large but, considering conservation of angular momentum as the star expands during its evolution, any rotation period is expected to be much larger than the observed hotspot evolution timescales.

Observations, for example Gray (2000), tend to show that hotspot occurrence is correlated with low overall brightness. Such a phenomenon is difficult to explain until one considers the results of stellar atmospheric models. Such models of convection in red supergiants stars show that hotspots on the simulated stellar surface occur preferentially at the edges of darker features (Freytag *et al.* 2002; Freytag & Höfner 2008; Chiavassa *et al.* 2009). They have also shown that the timescales, sizes and numbers of the observed hotspots can be explained very well using models of giant convection cells on these stars.

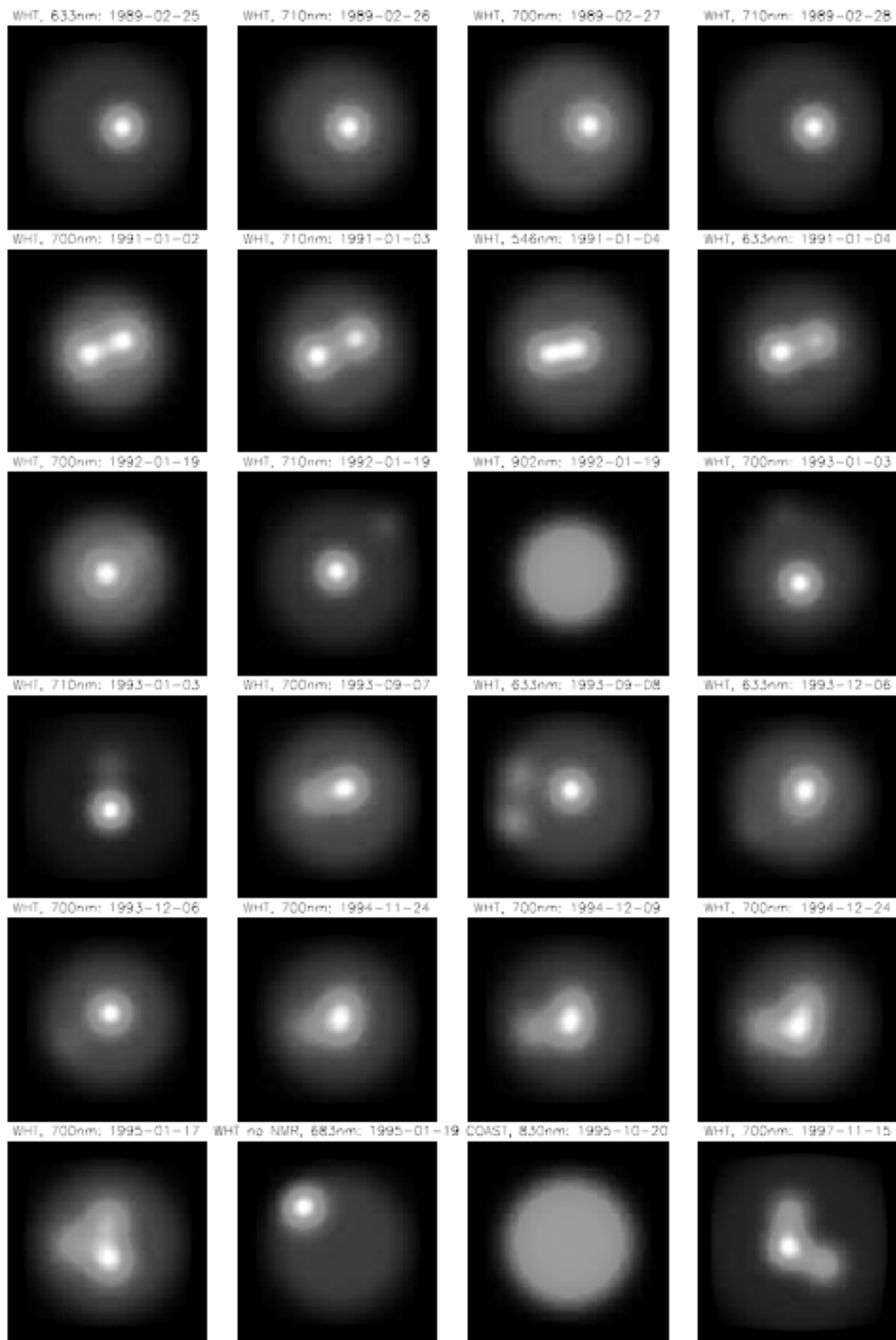


Figure 6: WHT and COAST near-infrared interferometric observations of Betelgeuse compiled from published data of spot positions and intensities covering a time interval of nine years. (Freytag *et al.* 2002)

2.5 Polarization

Strong circumstantial evidence for localized hotspots on the surfaces of late-type supergiants has, in the past, come mainly from analyses of polarization observations (Hayes 1984; Holenstien 1993). The observed polarization of red supergiants is seen to vary in both strength and direction, suggesting a highly nonspherical physical mechanism. The observations indicate that at least one characteristic of the star or the ejected mass must be nonspherical since the polarization is observed to vary in both strength and direction. Details regarding the source of the polarization, atmospheric versus dust, may be found in Holenstien (1993). Interestingly the polarization is seen to vary on time scales similar to the photometric variations.

2.6 Spectral Variability

Observationally the spectral lines of the red supergiant Betelgeuse are seen to vary in position and depth (Gray 2000; Josselin & Plez 2007; Gray 2008). Despite the variations, the spectral lines observed in both cases showed only small changes in their widths suggesting that the macroturbulence is constant. The line core positions are seen to vary over a range of 9 km/s; such a large shift compared with only small changes in line width, implies that one bright feature dominates the spectrum. In his concluding remarks, Gray (2008) suggests that the constant macroturbulence arises from motions within large atmospheric structures (or convection cells), which as we will see in the next section are readily predicted from models.

2.7 Photospheric Excursions

Gray (2008) expanded on his observations by plotting the line-depth ratio (the temperature index) as a function of line-core position (radial velocity), Figure 7. Using these tools, one easily sees a pattern of heating followed by the material rising, then a cooling and finally a descent. The symbol size is representative of the macroturbulence,

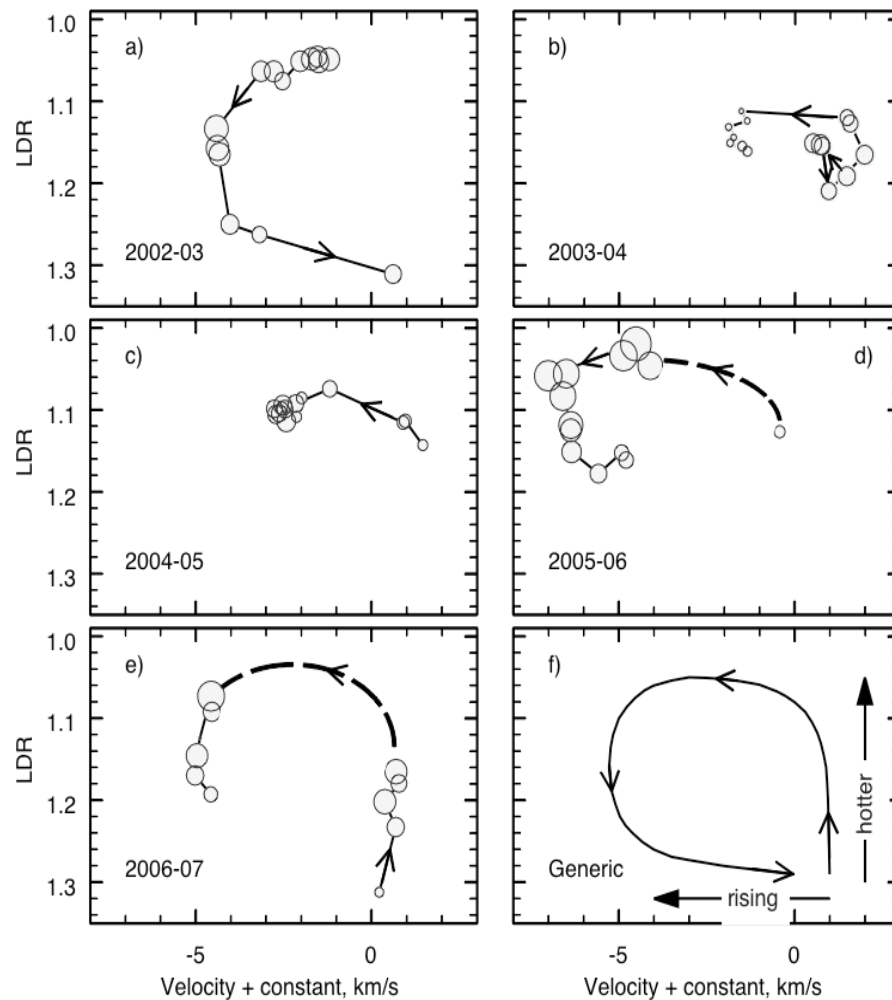


Figure 7: Line-depth ratio (temperature) is plotted as a function of mean core velocity for Betelgeuse. Each panel encloses a single observing season. Arrows indicate the direction of increased time. The characteristic timescale of these variations is ~ 350 days. Symbol size indicates measured line-widths (macroturbulence). Panel f) shows a schematic for convection. (Gray 2008)

showing that the more vigorous excursions are hotter, rise faster. The opposite case also arises where material reaches lower temperatures, rises more slowly, and the excursion eventually peters out. The relationship seen by Gray (2008) between velocity and

temperature varies significantly from the behavior of radially pulsating stars, where temperature and velocity variations are essentially in phase (e.g. Wesselink 1946; Walraven *et al.* 1958). It is easy to imagine how the behavior outlined in Figure 7 would result from large-scale convection, such behavior coupled with the observed bisector variations is highly suggestive of large convective cells erupting and sinking through the photosphere.

Chapter 3

3 Mechanisms of Variability

As was alluded to in the previous chapter, many physical explanations have been put forth as the cause of the variability detected in semiregular and irregular variables from binarity, to rotational modulation, from pulsation to magnetic fields. In this chapter we review the physical nature and the expected period and magnitudes of these various mechanisms.

3.1 Companion Stars

It has been well known since the mid-to-early nineteenth century that the majority of stars occupy multiple systems. It is common practice to classify these systems according to the method of their observation, many stars are classified in more than one group, however, the observational techniques are quite different:

Visual Binaries - are binary systems where both stars are readily resolved through visual telescopic observation. Obviously, resolving power of the instrument directly affects the number of these stars observed.

Spectroscopic Binaries - these stars demonstrate variations in their radial velocity (Doppler shifts) as they orbit their combined center of mass. In some cases we may see spectra of both stars present in the observations, and thus single and double peaked lines are evident due to the orbit.

Astrometric Binaries - these relatively close stars are seen to wobble around a point in space. This observed wobble is a result of the orbit around the center of mass, though the secondary is usually not visible.

Spectrum Binaries - these stars have composite spectra, but either extremely small changes in their radial velocities or large differences in the spectral types. Thus, we see the spectrum of both a hot and a cool star.

Eclipsing Binaries - the systems appear edge on, thus as one star passes in front of the other we observe a fall in the combined brightness. These eclipses are seen in light curves of the system.

For further information on these systems and their classifications see Batten (1973).

Given the preference of stars to form in multiple systems it seems highly likely that many evolved giants and supergiants, including the red variables, are members of such systems. In fact, most of the stars that are the focus of this study are known to be such. Thus, depending on the orientation, contents and dynamics of the system, companion stars can cause both photometric and radial-velocity variability. In fact, orbital motion has been suggested by a number of authors as a major contributor toward some of the variability exhibited by luminous red variables. Orbital motions were proposed to explain the existence of long secondary periods and muliperiodicity (e.g. Wood *et al.* 1999, 2004a, 2004b), as well as the interferometrically observed hotspots (Buscher, Baldwin, Warner, & Haniff, 1990). However, as was discussed in the previous chapter, binary transits are unlikely to be the cause many of the variable features observed. For example, hotspot evolution times are too short to be described by transits of a hot companion.

3.2 Surface Features

There are a number of stellar atmospheric phenomena that can cause variations in the photometry and radial velocity of their host star, as well as other stellar observable parameters.

3.2.1 Starspots

The movement of surface features on the sun is a well known phenomenon, and photometric and spectroscopic modulations are attributed to such features in other stars (Vogt *et al.* 1987; Vogt 1981 and many others). These features are dark spots on the stellar surface caused by a perturbation in the local magnetic field: intense magnetic

activity within the region of the spot compared to the surrounding area prevents the flow of energy from the stellar interior by inhibiting convection (Biermann 1938).

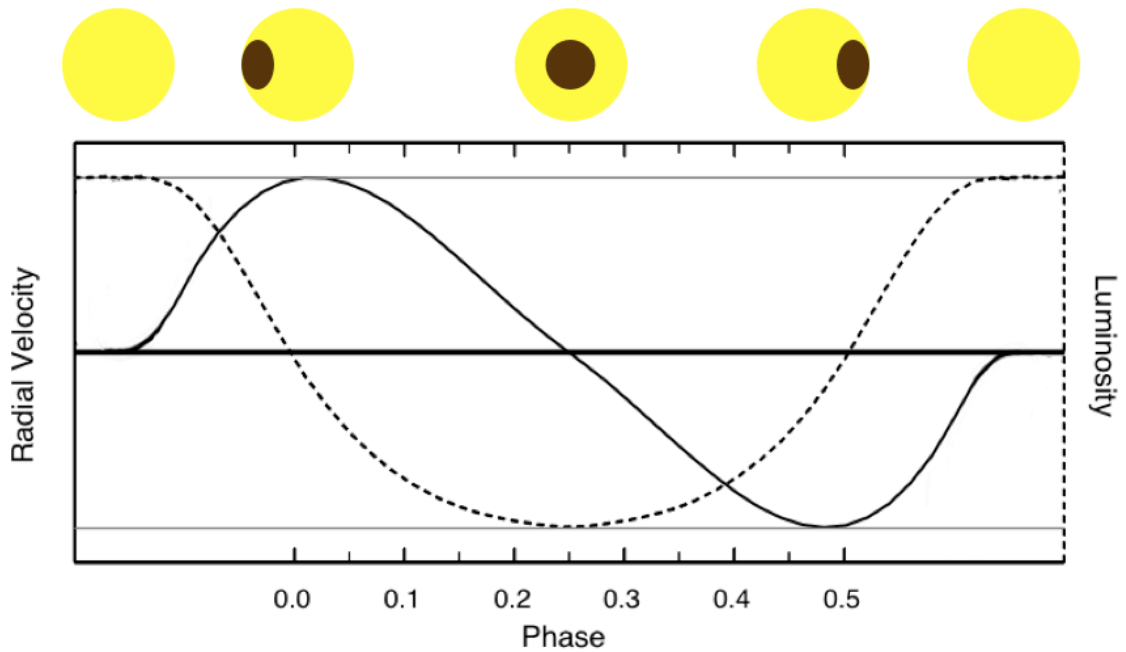


Figure 8: *Top* – Schematic diagram of a large star spot showing different epochs of stellar rotation. *Bottom* – Sample graphs of the luminosity and the stellar radial velocity that coincide with each epoch.

The photometric effects of spots are well documented for late-type dwarf stars (Kron 1947, 1952; Chugainov 1966; Henry *et al.* 1995). In these cases the light curves appear modulated with the rotation period of the star and also show small variations due to inhomogenous spot lifetimes which can vary from a few months to a few years (Bartolini *et al.* 1983; Olah *et al.* 1986; Strassmeier & Bopp 1992; Olah *et al.* 1997).

Spectroscopically the spots manifest as changes in line-shapes, either the presence of variable emission humps within absorption lines (in extreme cases) or, more usually, a variable asymmetry in the spectral lines. Such variability can ultimately cause an observed radial-velocity variation, whose amplitude is smaller than the $v \sin i$ of the star.

Combined, one should see maximum luminosity coincident with the mean radial-velocity, as seen in Figure 8.

Much like companion stars, spots have been identified as the cause of interferometric hotspots and of the irregular brightness variations of red variables. However the variations in both cases have timescales much too short to be attributed to a rotational origin. One must be cautious not to dismiss an argument to hastily, should spot lifetimes in red giants and supergiants be similar to those of K and M dwarfs, then their lifetimes would be close to the timescales demonstrated by red variables.

3.2.2 Convection Cells

In 1975 Martin Schwarzschild (Schwarzschild 1975) predicted the existence of large-scale convective elements dominating the light from evolved giants and supergiants. His work was driven by the suspicion that convection played a major role in ejection and mass loss from the atmospheres of these stars. Early scaled solar wind models had failed to accurately model the circumstellar envelopes of red giant stars (Weymann 1962), driving the need for a different approach. The first steps were taken by using the observed diameters of granules and supergranules for the Sun, and through some scaling assumptions, forming a depth model of their relative positions with respect not only to one another but also to physical parameters, such as ionization fractions and temperature of the stellar layers. The models showed that it is possible for the large scale (supergranulation) to provide the dominant photospheric convection in these stars. His arguments permitted an extreme picture of convection in red giants and supergiants, where the dominant convective elements are so large that only a handful of them occupy the surface of the star at any one time.

The theoretical description of convective motion in the atmospheres of red supergiants and AGB-stars has made considerable progress since the time of Schwarzschild, thanks in part to the pioneering hydrodynamic models of solar convection by Nordlund and Stein (for examples see Dravins & Nordlund 1986; Nordlund & Stein 1989; Nordlund &

Stein 1999). For examples of models of convection in red giants and supergiants see Höfner *et al.* (1998), Höfner (1999), Winters *et al.* (2000), Freytag *et al.* (2002), Freytag (2006), and Chiavassa *et al.* (2009). Recent modeling has focused on the well-observed red supergiant Betelgeuse. Most such works agree well with the initial predictions of Schwarzschild (1975) and while able to recreate the interferometric observations (Chiavassa *et al.* 2009) they still struggle to match the spectral observations (Chiavassa *et al.* 2006).

Models of large-scale convection in red supergiants typically report large dark and light areas on the stellar surface. The bright areas are as much as 50 times brighter than the dark regions (Chiavassa *et al.* 2010), theoretical images look remarkably similar to interferometric observations like that of Figure 6. The patterns are highly time variable, with bright regions having lifetimes of only weeks in the visible. These models suggest that at these wavelengths the light emerges from high in the atmosphere ($\tau < 1$) where the effects of waves and atmospheric shocks can become important. The interaction of convection on this scale with other modes of variability is not well understood, though it is not unlikely that the continual perturbing effect of convective cell emergence drives a variation (as suggested by Gray 2008 amongst others). Since the rotation rates of red supergiants are so small any interaction with rotation is unlikely to occur (thus, no stellar dynamo will be active).

The effect of such large convective cells on the atmospheres allows for some predictions regarding likely observations. We should expect brightness, temperature, and radial-velocity changes, however the nature of the envelopes of evolved supergiants and the stochastic nature of convection mean that the variations will not necessarily be either in phase or coherent. The cells themselves are expected to vary in size, temperature, and projection through the atmosphere. These stars are also subject to extreme limb-darkening, thus the effects of a cell at disk center will be quite different from the effects of a cell at the limb. In fact, noncoherent and irregular variations are a natural consequence of such large convective elements.

3.2.3 Binary Heating & Ellipsoidal Variability

The physical influence of a companion star (i.e. radiative heating and tidal interactions) is known to be responsible for variability in many stars (Morris 1985). A review of such processes in ζ Aurigae binaries, systems with a cool bright giant or supergiant primary and a hot main sequence or sub dwarf secondary with orbital distances small enough that the hot dwarf is within the wind of the cool supergiant, was given by Eaton *et al.* (2008). Given that Antares has a hot companion, albeit more distant than in these systems, such effects may be important.

3.3 Pulsation

Pulsation in stars is the general state of undergoing, usually periodic, expansions and contractions; these motions typically result in variations in the brightness and the radial-velocity. When such oscillations become extremely large they can cause mass-loss, dust clouds and shock waves. One type of red variable, the Mira-type stars, are undergoing all three due to the large-scale of their oscillations (Bowen 1988, 1990; Bowen & Willson 1991).

Since stars are three dimensional bodies their natural oscillation modes have nodes in three orthogonal directions: concentric shells in r , cones in θ , and planes in Φ . In most pulsating stars, the pulsation axis coincides with the rotation axis. In dealing with the mathematics and modeling/reconstruction of stellar pulsations we use three principle numbers: n gives the number of radial nodes and is the overtone of the pulsation; l gives the number of surface nodes and is the degree of the pulsations ($l = 1, 2, \dots, n-1$); and finally m is the order of the pulsations ($m = \pm 1, \dots, \pm l$) and $|m|$ gives the number of surface nodes that are lines of longitude. Here we review the expected observational effects of, firstly, radial and, secondly, non-radial pulsations.

3.3.1 Radial Modes

The simplest pulsation modes are the radial modes, in this mode the star swells and contracts, heats and cools spherically symmetrically. This is the usual pulsation mode for Mira and Cepheid variables. In Mira variables, according to Ostlie & Cox (1986), the variability is heat driven in the ionization zones. Pulsation in this mode is usually responsible for large and regular variations in brightness, see Figure 9, and radial velocity. While such variation is able to describe the observations of Mira variables, the expected amplitudes are too large and the periods too regular to explain the variability seen in semiregular and irregular variables. However, some semiregular variables appear to undergo periodic variability which is perturbed by irregular processes. Such perturbations could result from several modes of pulsation; in fact one or more radial modes have been identified in a large number of semiregular variables (Kiss *et al.* 1999).

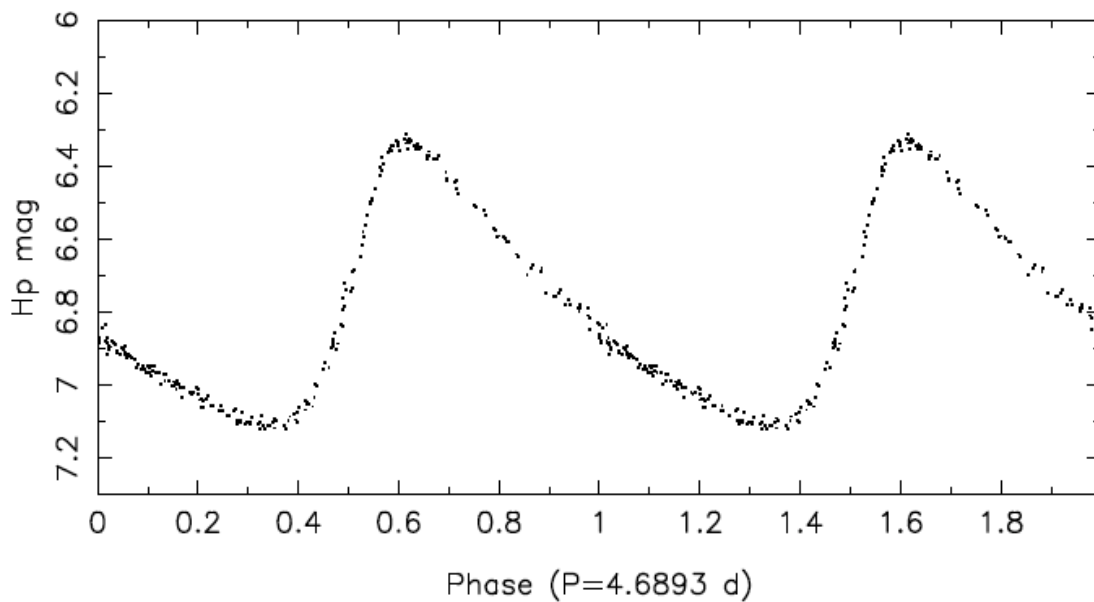


Figure 9: Hipparcos light curve of a classical Cepheid using data from Perryman (1997). (Aerts *et al.* 2010)

3.3.2 Nonradial Modes

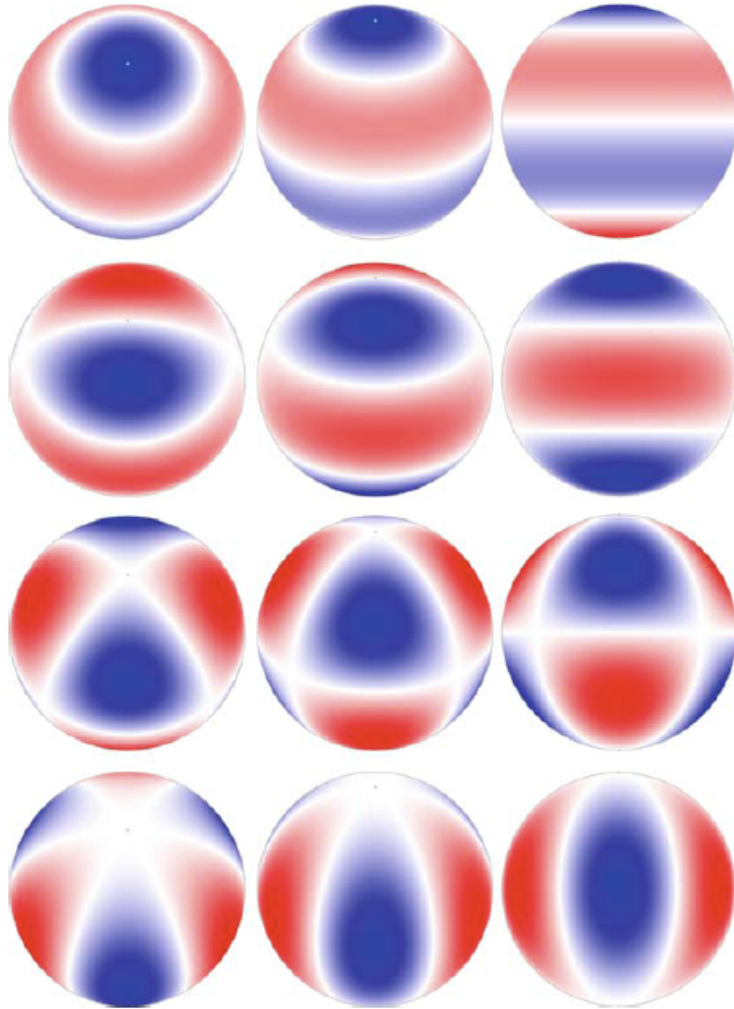


Figure 10: Radial motions of the $l=3$ octupole modes. The columns show the modes from differing viewing angles: with the pulsation pole at 30° , 60° , and 90° respectively from left to right. The red and blue sections represent the surface motions (red – inward and blue – outward), while the white bands represent the locations of surface nodes. For the top row $m=0$ and the nodes lie at latitudes of 0° and $\pm 51^\circ$. For the second row $m=\pm 1$ so there are two latitudinal nodes and one longitudinal. For the third row $m=\pm 2$ so there is a single latitudinal node and two nodes that are lines of longitude. Finally, in the fourth row $m=\pm 3$ (or $|m|=l$) and all nodes are lines of longitude (Fig 1.4 Aerts *et al.* 2010).

Nonradial pulsations occur for all cases of $n \geq l$, the simplest form is the dipole oscillation for which $l=1, m=0$. While these pulsations are referred to as ‘nonradial’ this does not mean that their motions do not occur in radial directions. In fact, some modes have large motions in the radial directions. However, unlike radial modes, nonradial modes cause no change in the stellar radius. There are equal portions of outward and inward directed motion in the radial direction. Examples of the radial motions of some nonradial modes are shown in Figure 10. There are two main solutions to the equations of motion in pulsating stars which lead to two pulsation modes: p-modes in which pressure is the restoring force (Cox 1980) and g-modes in which buoyancy is the restoring force (Hansen & Kawaler 1994).

p-modes are predominately radial in that they undergo larger radial movements than tangential movements (Nordlund & Stein 2001) and are characterized by large changes in density and pressure. Such oscillations are highly sensitive to surface conditions and have amplitudes that are maximised near the stellar surface. Figure 11 shows the radial eigenfunction as a function of radius which, for p-modes, is largest at the surface. These modes are also referred to as acoustic waves due to the resemblance of high order modes to sound waves. High overtone, low degree ($n \gg l$) pulsations, such as those of the solar five-minute oscillation show a “comb” of frequencies in their power spectra, Figure 12. Note the similarity between the form of the peak shown in Figure 12 and those in Figure 3 of the previous chapter for the studied semiregular variables. Thus, it seems reasonable to describe the variations of semiregular and irregular variables in terms of nonradial pulsations with high n and low l . Since in the solar case these pulsations are driven by convection, it is likely that they are similarly driven by convection in semiregular and irregular variables as well.

g-modes in solar-like stars are trapped in the convective envelopes (see Figure 11), though they may be viewed from the perturbations they cause to the envelopes as is the case for γ Dor stars (Aerts *et al.* 2010). They are sensitive to the interior conditions, this mode is predominantly transverse and has no radial counterpart.

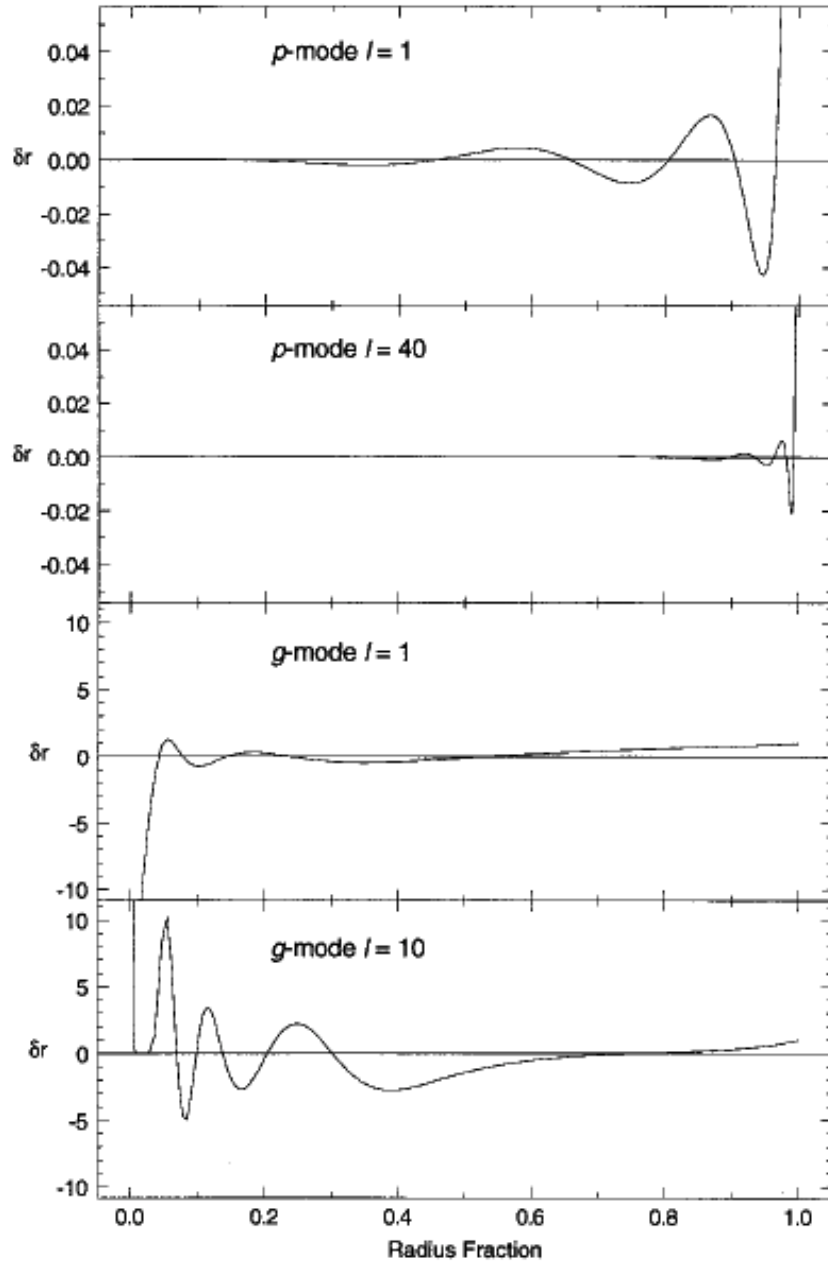


Figure 11: Amplitudes of the radial eigenfunction for typical p-modes (*top*) and g-modes (*bottom*). p-mode radial eigenfunctions peak near the stellar surface, while g-mode radial eigen functions peak near the interior. (FIG 3 Demarque & Guenther 1999).

Recently, Bedding *et al.* (2010) suggest the detection of mixed-mode oscillations caused by an interaction between the g-modes of the convective zone and the envelope p-modes. A discussion of these modes is beyond the scope of this thesis but it will be interesting to see the progression of this discovery.

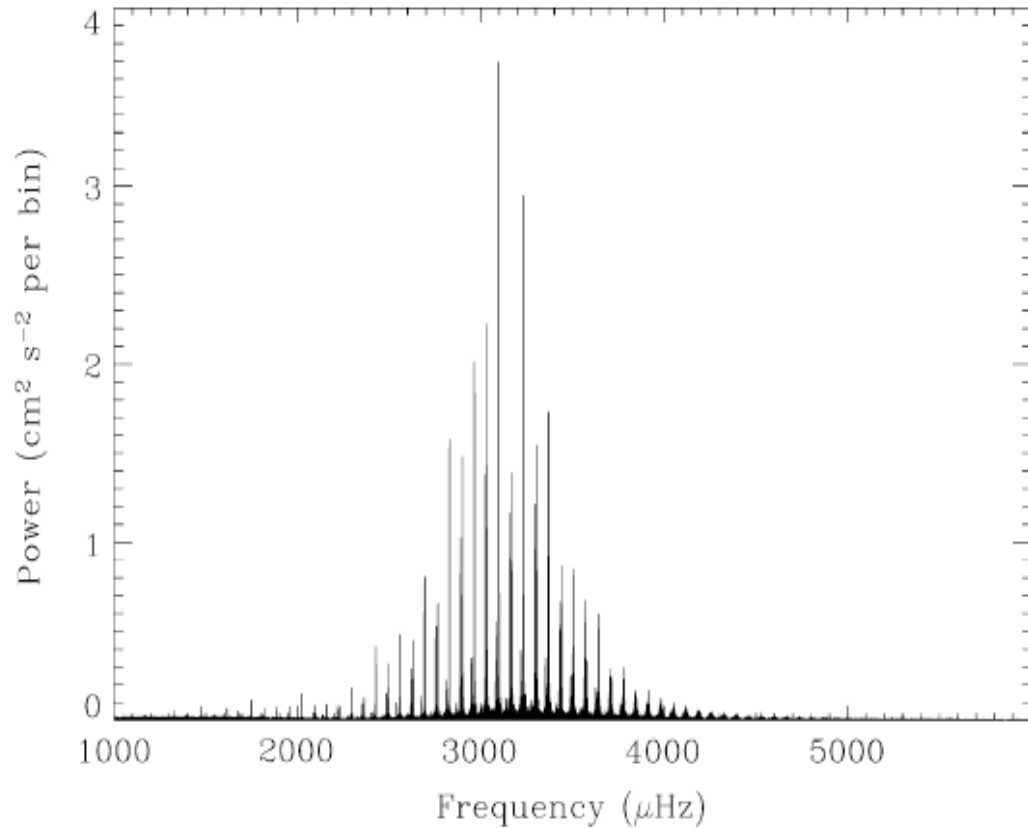


Figure 12: The power spectrum of the solar five-minute oscillation. (Fig 1.9 of Aerts *et al.* 2010). Power peaks look very similar to those seen for semiregular variables, Figure 3.

Chapter 4

4 Observations and Reductions

Solar spectroscopy began more than three centuries ago, when scientists of the era (including Newton) noted the dispersion of the Sun's light by a prism. Whether or not Newton, at this time, noticed the absorption lines in the dispersed sunlight is unknown, however by 1820 Fraunhofer had begun identifying lines within the solar spectrum. By the mid-to-late 1800s the classification of stars using prominent spectral features had begun, these initial identifications were made using multiple-prism optics and resulted in extremely low resolution spectra in which only the most prominent spectral lines, such as those of hydrogen could be identified, see Figure 13. By the 1900s the stellar spectral classification system as we know it today had started to take shape (see Franks 1907 for an example). It was through early and primitive spectroscopic techniques that astronomers first realized the nature of stellar atmosphere. Noticing the existence of metallic lines they deduced that high temperatures were necessary and that the observed features likely stemmed from an atmosphere (e.g. Huggins & Miller 1864).

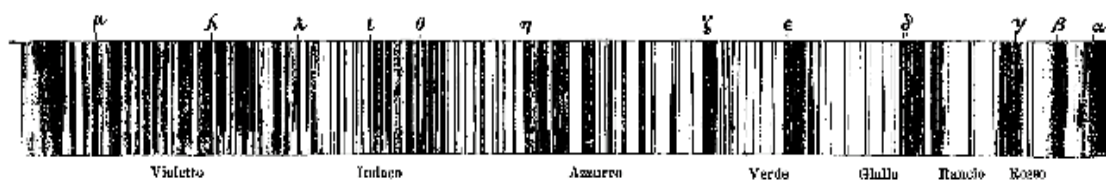


Figure 13: A sketch of the spectrum of Betelgeuse (α Ori) from Secchi (1866). Notice the low resolution and remarkable detail. The spectrum proceeds from blue on the left to red on the right, colours are designated in Italian. The Greek letters give the line designation.

It was from these humble beginnings that spectroscopy grew into the observational cornerstone that it is today. The power of spectra to offer up knowledge about the physical circumstances of an object was quickly realised. Doppler (1846) applied his description of frequency changes due to motion in sound waves to the light emitted by stars in order to measure line-of-sight velocities (his original work provided numerical examples without any measures). Although Doppler's (1846) interpretations of the behavior of stars was somewhat misguided the overall concept is used to this day. Measurements of radial-velocities and Doppler broadening (by stellar rotation and/or mass motions) have become mainstays of all branches of astronomy. Similarly, the effect of Zeeman splitting and thus Zeeman broadening was realized before the 1900s and was being used actively in the measures of sunspots not long thereafter (Hale 1908). Combined with the pioneering works of many people of the era it quickly became obvious that spectral observations of the heavenly bodies could provide information regarding composition, temperature, pressure, dynamics and magnetic activity.

Since that time the improvements of optics and the development of the astronomical grating (Wood 1946) have allowed for masterful progress to be made. Under current circumstances, resolving powers of 400,000 or more have been realized. More recently, CCD chips have replaced photographic plates increasing quantum efficiency by 1-2 orders of magnitude. Along with this increased sensitivity the use of CCD chips also allowed for the digitization of astronomical data, greatly improved reduction times and lowered observational costs. Improvements in the optical trains and larger telescopes mean that signal-to-noise ratios of 200 or more are readily achievable even at the best resolution.

As the aim of this thesis is to study the atmospheric dynamics of the target star(s), it seems natural to perform spectral analyses, since herein lies the most information one could hope to gain from a single observational technique. Thus, in this chapter we outline the technical specifications and capabilities of the spectrograph and telescope used to collect the majority of the data used in this thesis.

4.1 The Equipment

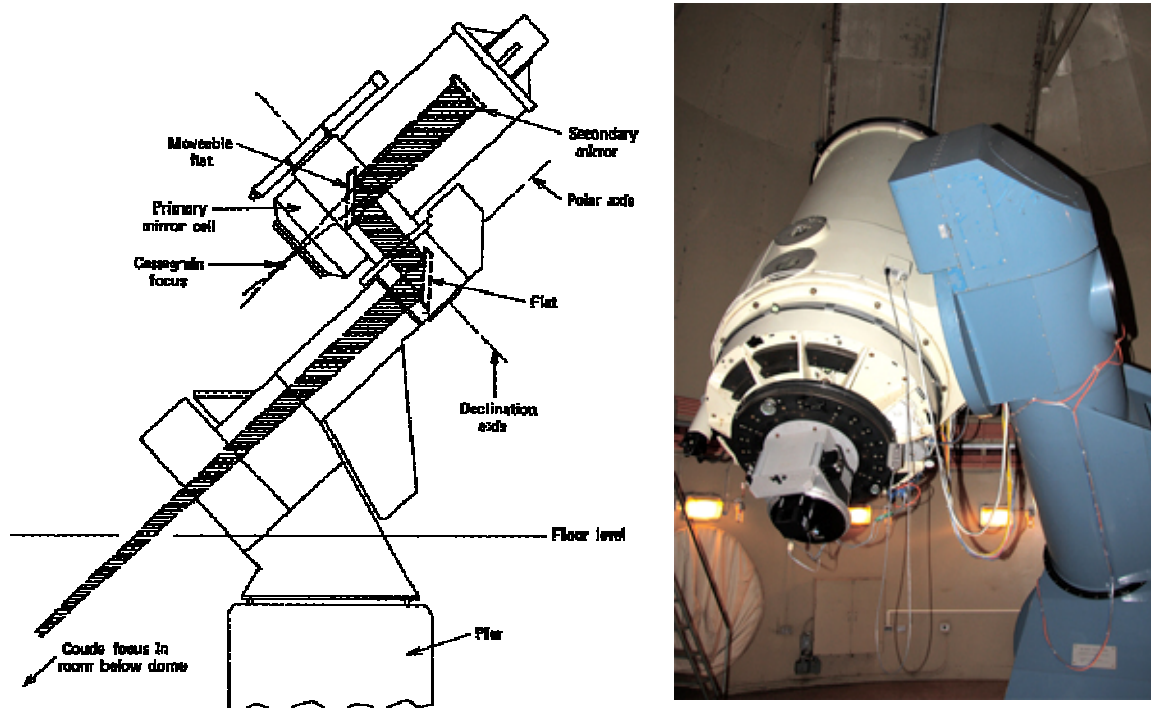


Figure 14: *Left* – schematic of the 1.2 m telescope of the Elginfield Observatory. *Right* – picture of the 1.2 m telescope of the Elginfield Observatory.

Observations were made using the 1.2 m Boller and Chivens telescope at the Elginfield observatory of the University of Western Ontario. Figure 14 shows both a schematic and a picture of this telescope. The optical chain feeds into a spectrograph at the $f/30.5$ coudé focus. By working at coudé focus, one can permanently mount the spectrograph and thus minimise thermal and gravitational flexure which would compromise the high resolving power desired. The light-path intersects five mirrors before entering the spectrograph, the primary is a bare aluminium mirror ($\sim 80\%$ reflectivity) and the secondary, 3rd, 4th and 5th mirrors are high reflectivity over-coated silver ($\sim 97\%$ reflectivity). Since the typical seeing on any given night is $\sim 5''$, a Richardson image slicer replaces the entrance slit, ensuring that more light passes into the spectrograph than when using a simple slit; details can be found in Appendix A. After passing through the image slicer the starlight enters the spectrograph and is collimated before falling upon the 316 l/mm blazed grating,

the optical path is shown in Figure 15. By using orders from the 7th to the 17th we are able to view spectra in a window from 3800 to 10000 Å, though any individual spectrum covers only 50 or so angstroms using a single order. A CCD camera with a focal length of 2080 mm was used to record the spectra with a typical dispersion of ~ 0.013 Å/mm.

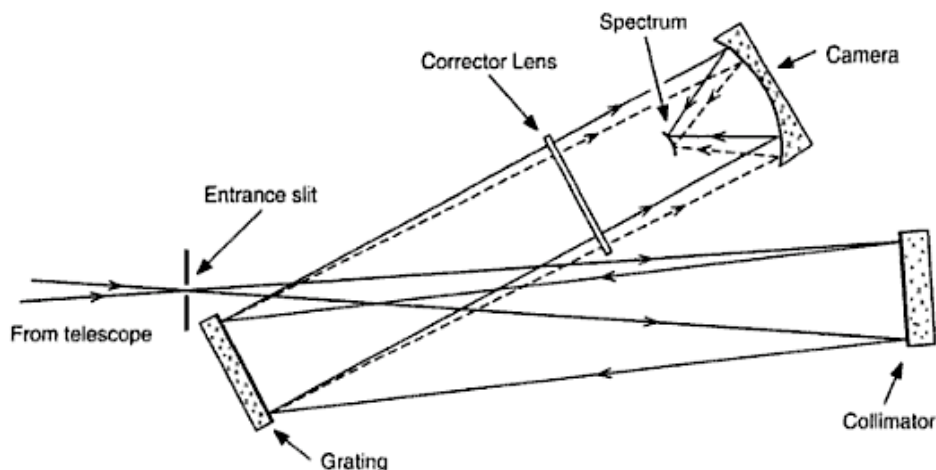


Figure 15: Schematic of a typical spectrograph. Light from the slit diverges and is collimated before falling upon the grating. Monochromatic light from the grating is incident upon the camera mirror and focused on the CCD. (Fig 3.1 Gray 2005)

4.2 Observational Techniques

The stars under observation in this thesis are cool, spectral-type G and cooler, and bright, luminosity class I-II, thus a wavelength range from $\sim 6215\text{\AA}$ to $\sim 6275\text{\AA}$ was chosen as there are few enough lines that blending due to the turbulence broadening is not wholly detrimental, while maintaining enough lines that a meaningful analysis can be completed. A sample of the spectra typical of the stars included in this thesis is shown in Figure 16. Here we show the K0 III star Arcturus (α Bootis) to demonstrate the nature of the broadening one has to deal with when observing high-luminosity, low surface-gravity stars. In order to select this range in wavelength, a filter is placed in the optical path before the beam enters the image slicer and the 9th order is selected.

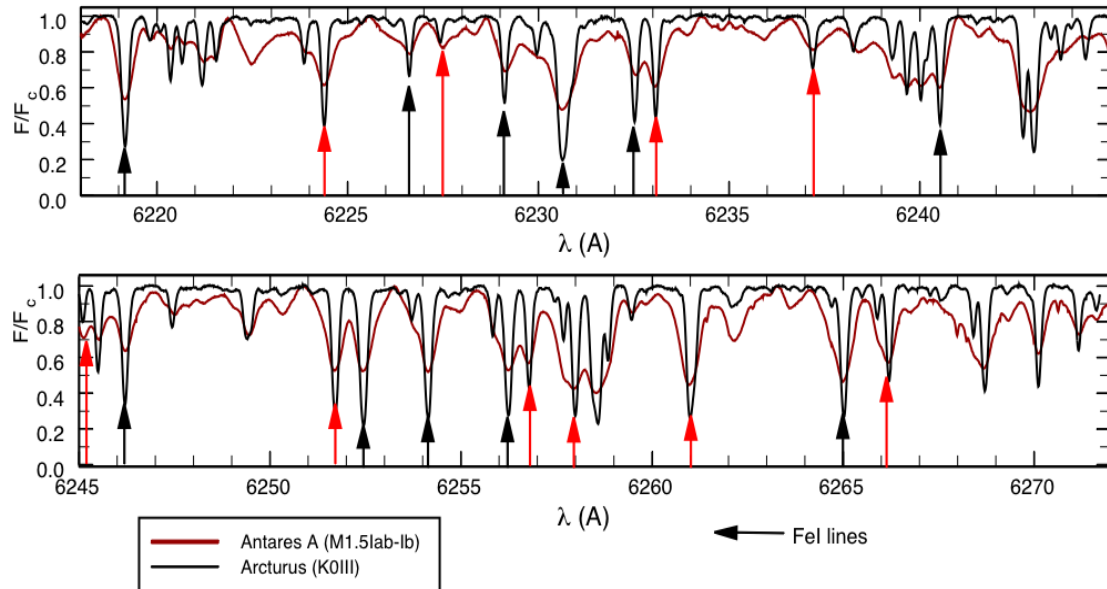


Figure 16: Spectrum of the M1.5 supergiant Antares, typical of the spectra used in this study, is plotted in red with a spectrum of the K0III star Arcturus for comparison shown in black. Note the reduced line depths and extreme broadening seen in the supergiant. The black arrows denote the Fe I lines usually used for analysis in this spectral window. The red arrows indicate the non-Fe I lines that were added as part of this thesis.

After selecting accessible targets there are a number of observational criteria we wish to fulfill in order to get the most from the data collected: (i) Precise wavelength scales for use in radial-velocity determinations, (ii) high signal-to-noise ratios, (iii) high resolving power, (iv) a linear detector, (v) cosmic ray free spectra, and (vi) reasonable integration times. To keep integration times down and maintain good signal-to-noise ratios bright targets are required. Cosmic ray hits are unavoidable unless the detector is encased in the same manner as neutrino detectors so these are instead cleaned from the spectra after observation, details are given below. Since, as an observer we can have no direct effect on the sky conditions we are limited in the actual signal-to-noise achievable. There are a

number of things one can do to ensure that this sky-limited maximum is achieved. The CCD chip is cooled to -125°C to keep the electron noise per pixel as low as possible. Additionally, it is useful to have the coudé room and camera initiated one to two hours before sunset, the effect of this precaution is twofold: firstly, since the electron noise intrinsic to the chip falls exponentially after power-up, and secondly, it allows the temperature disturbance caused by ones presence within the room to dissipate. By maintaining a coudé room temperature of a few degrees above the nightly minimum, the room remains temperature stable throughout our observations, varying by maybe a single degree. Finally, vapors from the CCD cooling system are vented from the room during a refilling cycle, the final refilling cycle is instigated manually, and the autofill system is shutdown along with the camera initiation. By maintaining such a system, one ensures temperature stability of the optical pathway inside the spectrograph, which as we shall see in a moment is invaluable in maintaining high-precision wavelength measures and reduces the electron noise of the CCD during exposures which will increase the resulting post-reduction signal-to-noise ratio.

4.2.1 The Telluric Lines

Computation of the wavelength-scale for the observed stars comes from telluric lines of the water vapour inside the spectrograph. Telluric lines have often been used to supply the reference spectrum for solar lines and have been considered in a stellar context by Griffin & Griffin (1973). Since the optical path is identical for the reference spectrum as for the stellar spectrum using the telluric lines within the spectrograph has the advantage of reducing errors associated with the both the wavelength calibration and the sky position of the object in question. The precision reached by our set-up, which will be further discussed below, is modest at ~ 25 m/s for sharp-lined spectra, increasing to nearer 100 m/s for the broad lined stars considered in this thesis. However, this modest precision comes with a major advantage over the typical high-precision absorption cell set-up (e.g. Butler *et al.* 1996; Rupprecht *et al.* 2004), in that the stellar spectra are unaffected by the measurement technique. By taking the telluric exposure sequentially with the stellar exposure we maintain the full integrity and the full usefulness of spectral

observations while achieving reasonable precision. A typical telluric spectrum is shown in Figure 17, measurements are based on the details published by Gray & Brown (2006), although a further three lines have been added to the conversion from telluric to stellar wavelength. The lines beyond the bounds of the wavelengths noted in Figure 17, that is the one before and two after, were added to improve precision in these parts of the stellar spectrum. With the addition of these lines the length of the lamp exposure required to minimise the residuals was slightly reduced in order to avoid saturation of some lines. Telluric exposures were taken using a ribbon-filament lamp and an order sorting filter, which selects the 6th order at 9375\AA , placed before the image slicer. The mean scale is computed from an equal number of post- and pre-stellar exposures, such that if we exclude any one telluric exposure, then the mirror exposure was also excluded.

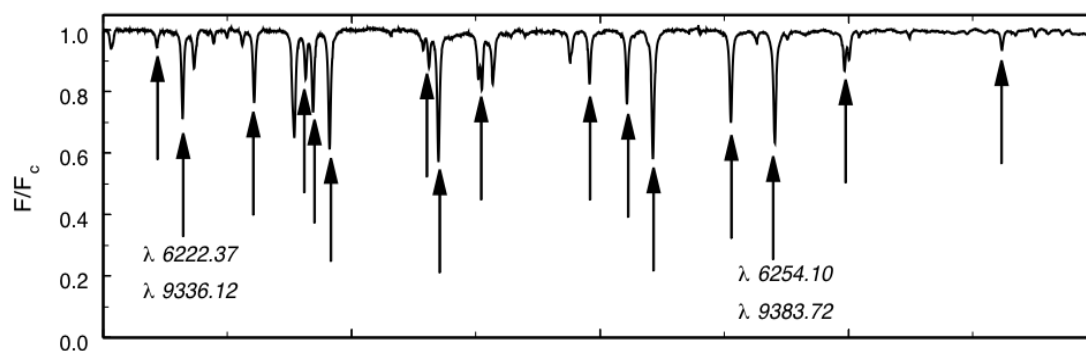


Figure 17: Telluric spectrum, observed in the 6th order, with the 16 lines used for wavelength conversion marked.

There are four major sources of error in the radial velocities arising from this technique: (i) imprecise interpolation of the drifts that occur during the exposures, (ii) photon noise, (iii) imprecise barycenter corrections due to errors in the recorded time of the exposure, (iv) errors in the adopted wavelengths and errors in the polynomial that is used to convert pixel number to wavelength.

The errors arising from the first source come from two sources: changes in temperature and pressure and mechanical changes inside the spectrograph. In order to analyze the

effects of the changes in temperature and pressure we must first discuss the effect of using two different spectral orders for our observations. Because we make use of two different grating orders we must account for the difference between the refractive indices of the two orders. The wavelength change caused by the refractive index of the air within the spectrograph is

$$\Delta\lambda = \lambda (n-1), \quad \text{Equation 1}$$

or
$$v_R = (\Delta\lambda/\lambda) c = c (n-1). \quad \text{Equation 2}$$

Thus, the differential shift between the two orders is given by

$$\Delta v_R = (n_2-1) c - (n_1-1) c = (n_2-n_1) c, \quad \text{Equation 3}$$

where the subscripts refer to the two orders used. Using the wavelength dependence of n given by Allen (1973) and Gray & Brown (2006), we find (n_0-1) is 0.00027662 at 6250Å and 0.00027436 at 9375Å. Using equation (3) this gives a difference of 678 m/s. This differential shift varies with changes in temperature and pressure and it is from these changes that the errors in the radial velocities are introduced. To account for the variations, which are the same in both orders, we can multiply the differential shift by a density factor, which is taken from Allen (1973) and Gray & Brown (2006). The density factor is given by

$$d(P, T) = \frac{P [1 + (1.049 - 0.0157T) \times 10^{-6}]}{720.883 (1 + 0.003661T)} \quad \text{Equation 4}$$

where P is in mmHg and T is in °C. The use of a precision thermometer and barometer ensures we can measure such shifts down to ± 10 m/s and can thus account for the changes that typically occur over a single stellar observation (~ 50 m/s).

As mentioned above there is also an error in the telluric wavelengths introduced by the mechanical shifts, these include: (i) thermal expansion of the diffraction grating and/or CCD, (ii) positional shift of the detector mount as the dewar weight drops due to evaporation of the coolant, and (iii) other mechanical changes within the spectrograph.

Since the telluric spectra are taken sequentially with the stellar spectra, we assume that the mechanical shifts are the same for the telluric spectra as they are for the stellar spectra with which they are associated. We can measure this error by comparing the wavelength scales of the telluric spectra taken either side of the stellar exposures; the typical error for Antares A is ≤ 20 m/s.

Errors in timing arise from variable sky conditions. If seeing or cloud cover vary significantly during a single exposure the point of mid-photon count will not coincide with the median time of the exposure. This error then carries into our barycenter corrections. At the Elginfield observatory the maximum rate of change of radial velocity due to Diurnal cycle is 89 m/s hr^{-1} (Gray & Brown 2006). A typical exposure of Antares A is 1800 s, so a timing error of 10% would result in an error in the radial velocity ~ 5 m/s.

4.2.2 A Night at the Dome

On a typical night the observer will arrive an hour or two before observations begin. Upon arrival the CCD camera dewer will be filled, the spectrograph mirrors opened, the grating position set and the CCD turned on. Observations begin with a pair of flat-field exposures, taken using the ribbon-filament lamp with the stellar filter in place in front of the image slicer. This will be followed by a pair of telluric spectra, using the same lamp but an order sorting filter, a stellar exposure and two more telluric spectra. Typical stellar exposures last from 10-120 minutes depending on the brightness of the star and sky conditions. At the end of the night, with the telescope computers shut down a 120 minute dark exposure is taken, which during reduction will be scaled to fit the exposure in question.

4.3 Reductions

[All of the utility programs mentioned in this section were written and provided by Dr. D. F. Gray.]

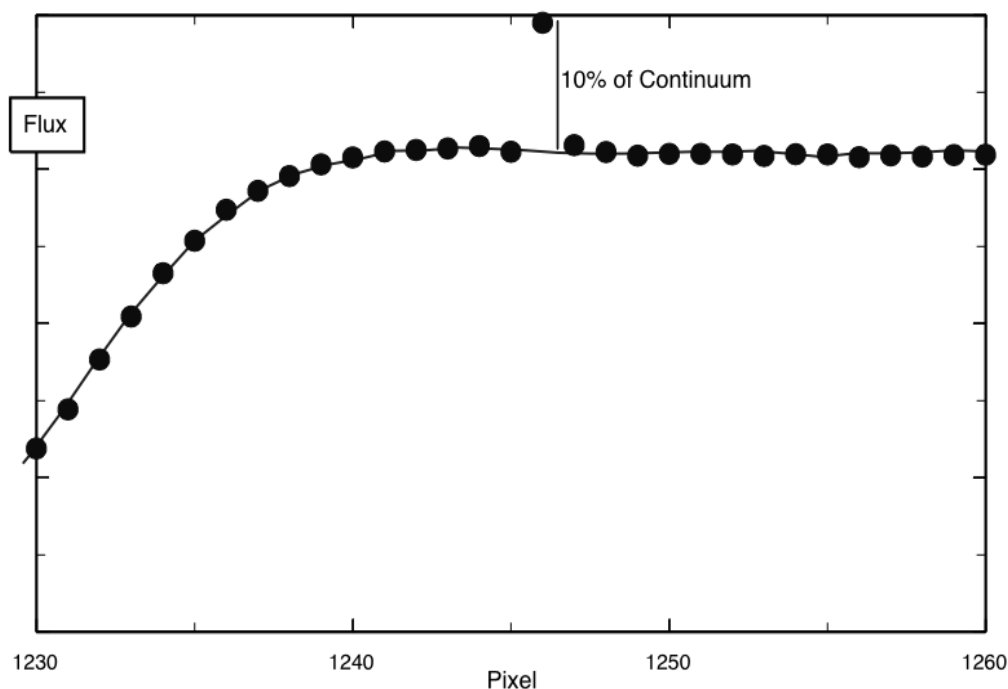


Figure 18: Cleaning of a cosmic ray hit by the R9 reduction software. Points are the raw CCD pixel flux points. The line is the reduced data in which the cosmic ray spike at pixel 1246 has been successfully removed.

Reduction of the data is done by the R9 algorithm, it requires the stellar/telluric exposure, a flat-field exposure, a dark exposure, and a bias exposure. The R9 program removes instrumental effects (as outlined below) and cosmic ray spikes. The stellar and telluric exposures are divided by the flat-field exposure to account for the non-uniformity of the CCD pixel response, pixel-to-pixel electron overflow and the slope of the spectral order. The dark exposure is subtracted from the stellar or telluric exposure to account for the zero level offset of each pixel. The cosmic ray spikes are dealt with by fitting the “gap” in the spectrum using the points to either side of the spike; recognition of spikes is built

into the R9 algorithm. A typical cosmic ray correction can be seen in Figure 18, these spikes typically incorporate one or two pixels and are easily distinguishable from spectral features, which are typically much more extended than this. Each of the 4096 columns is averaged over the 200 rows in bins of 10 which are further binned produce the final single spectrum used in analysis.

Once the data have been cleaned in this way they are continuum normalised. In stars where the continuum is easily recognizable, this can be automated. However, the evolved stars studied in this thesis are cool, resulting in many metal lines being present, and have extreme line broadening due to large turbulent velocities. Thus, the continuum is generally indistinguishable from the line wings. In this case a two-fold normalisation process was chosen. The cleaned spectra are processed using SPLT4, where one can choose between automated or manual normalisation. In manual mode, one selects a number of pixel positions to use as normalisation points, the flux at these points is set to unity. Using this method one can determine by eye the best normalisation, and the one which is the most uniformed from one exposure to the next. The pixels chosen as continuum points are the same for each exposure. This gave the normalisation over the full length of the spectrum but some regions were affected by large temperature shifts (~5-10%). Since we wish to keep as many Fe I lines as possible in our analysis, as they are the typical lines used and have precise rest wavelengths, a secondary normalization approach was taken.

The spectrum was ‘cut’ into sections covering five to eight angstroms, within these regions a normalization point (usually coinciding with the unity continuum) was selected, this gives λ_1 . Each exposure was then inspected to ensure that this point remained at a constant flux level. A second point was then selected some three to five angstroms away which, via a scaling relation, was also forced to be the same in each exposure. The scaling relation used was:

$$F/F_{c,new} = F/F_{c,old} [1+m(\lambda \pm \lambda_1)], \quad \text{Equation 5}$$

$F/F_{C,new}$ is the adjusted normalised flux, $F/F_{C,old}$ is original normalised flux (output from SPLT4), λ_1 is the reference wavelength of the first point chosen, λ is the wavelength point at which the new flux is being computed, and m is a constant that is typically less than 0.01. The \pm in equation (5) arises from two affects: (i) λ may be larger or smaller than λ_1 and (ii) the adjustments needed for this normalisation may be positive or negative. From inspection we see that the flux at λ_1 remains unaltered, however it is found that this normalisation method works best when λ_1 is near to one edge of the wavelength window being considered. A sample normalisation window is shown in Figure 19, with λ_1 and the remaining normalisation required outlined. We note here that this secondary approach raises the level of the entire spectrum and, since both line cores and the peaks are affected by changes in broadening, when we wish to consider changes in the broadening (i.e. line widths) we encounter a few problems (these issues are addressed in that section of the

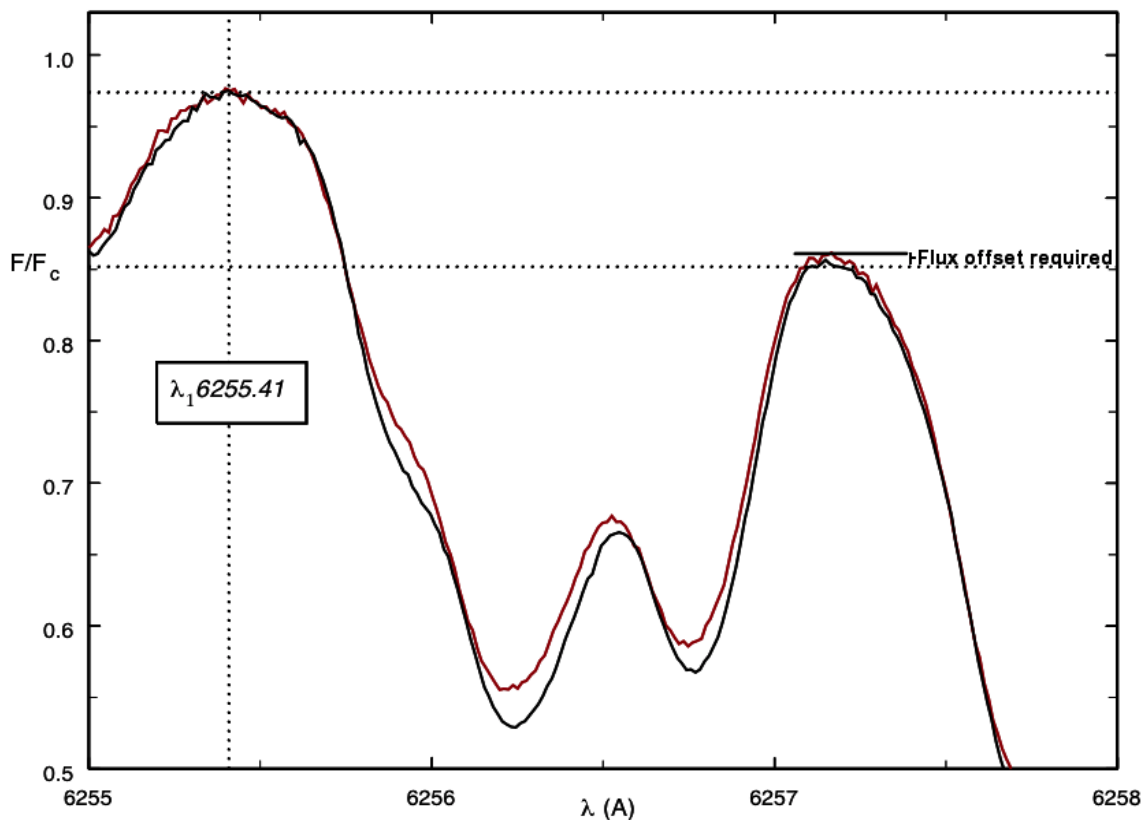


Figure 19: A typical normalization window. The black line is the high signal-to-noise reference spectrum; the red is the spectrum to be normalized using Equation 1 with the reference wavelength shown on the figure.

thesis; Section 6.4). In the cases of radial velocities, where only the line core position is important, and line-depth ratios, where we use two lines that are close together, this normalization technique does not affect our result. A shift of $0.1 F/F_c$ resulted in $\sim 1\%$ change in either of these variables. As is seen in Figure 19, the required shifts were typically much less than this. In addition since we are generally interested in the variations rather than the absolute values as long as our normalization remains consistent from one exposure to the next any introduced error should be minimised between any two exposures.

4.4 Program Star

After the findings of Gray (2008) regarding the motions of the atmosphere of the red supergiant Betelgeuse, it was felt that other red supergiants should be examined for similar phenomena. For this purpose we selected another bright M supergiant, Antares A. A number of factors influenced this decision: (i) the similarity in spectral types of the two stars, (ii) the large number of AAVSO magnitude estimates available for Antares and (iii) the brightness of Antares.

The remainder of this thesis will focus on the observations of Antares A, with a handful of other evolved stars being considered only briefly. Table 1 lists the parameters of the Antares system and the two stars within it. Antares has a combined spectral type, spectra of the system contain features of both the cool and hot stars. One, might then, worry that the spectra we observe are contaminated by the hot star. The flux ratio in the region we are concerned with is shown in Table 1. Two ratios are given: the first is calculated based on the difference in the visual magnitudes, the second is estimated from the comparison of ELODIE spectra of a typical M supergiant and a typical B dwarf shown in Figure 20.

Table 1: Observational details of the Antares system, with a focus on the primary star.

	A	B
Spectral Type	M1.5 Iab (Houk 1982)	B4 Ve
Mass	$18 \pm 4 M_{\odot}$ (Schroder & Cuntz 2007)	$10 M_{\odot}$
m_v	0.96 ± 0.06 (Nicolet 1978)	5.4
Radius	$883 R_{\odot}$ (Baade & Reimers 2007)	$4 R_{\odot}$
Luminosity	$48,000 \pm 1000 L_{\odot}$ (Schroder & Cuntz 2007)	170
M_v	-5.2 ± 0.9	
K Magnitude	$m_k = -3.78$ (Johnson <i>et al.</i> 1966) $M_k = -9.9$	
Parallax and Distance	$\pi = 5.89 \pm 1.00$ mas $d = 180 \pm 30$ pc (van Leeuwen 2007)	
Binary Period	1220 years (Mason <i>et al.</i> 2001)	
Separation	2.9'' (Worley & Heintz 1983)	
Flux Ratio	0.017 and 0.012	
A star timescales of variability	1733 days (Stothers & Leung, 1971) 350 days (Percy <i>et al.</i> 1996)	
Δm_v	0.28 mag	

Like other red supergiants, Antares A is variable in both magnitude and radial velocity. Antares A is classified as an Lc variable in the GCVS (Samus *et al.* 2012). Here we

discuss the timescales of variation that can be found from previous studies of this star, we consider the photometric and radial velocity variations separately.

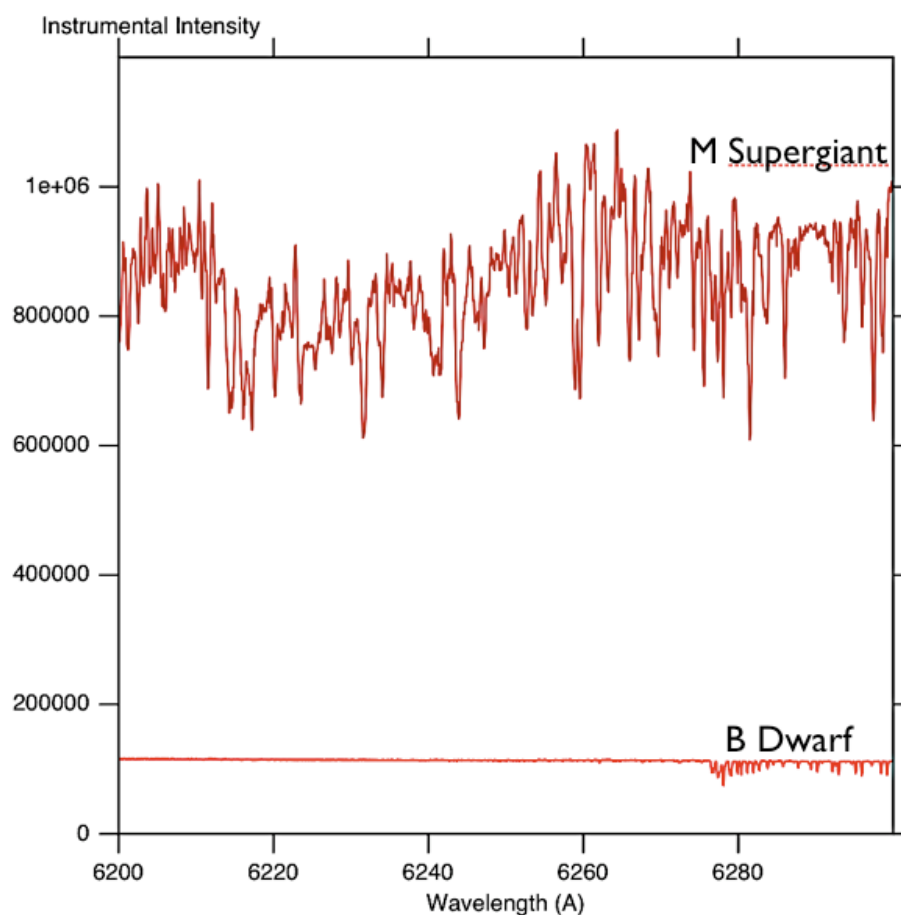


Figure 20: ELODIE spectra of the M-supergiant Betelgeuse (*upper*) and the B-dwarf Regulus (*lower*). The ordinate is the instrumental intensity and the abscissa is the wavelength in Å. The ratio of line strengths is ~ 0.012 .

Radial Velocity Variation – Variations in the radial velocity of Antares A have been reported since the early 20th century (i.e. Wright 1906); initially these variations were treated as arising from orbital elements and based on such assumptions, a period of 5.8 years (Halm 1909, Lunt 1916) was attributed to the observed variations. Even then the cause of the variability was disputed. Arguing that the variations were δ Cephei like, Spencer-Jones (1928) determined a period of 7.35 years. Even in these early

investigations, shorter variations superimposed on this long timescales were noted (Lunt 1916; Spencer-Jones 1928), though was usually attributed to noise rather than signal. It wasn't until the 1980s that further work was conducted in this regard, baring a single paper in the 1960s (Evans 1961), which notes a radial velocity variation but does not attribute a timescale to the variation. In the 1980s, Myron Smith and colleagues (Smith *et al.* 1989) undertook an investigation of the radial velocity variations of Antares A, Betelgeuse and α Her A. They reported a half-cycle of greater than 2.5 years and an amplitude of 5 km/s for Antares A. They also found a short period of 260 ± 20 days from radial-velocity analysis. This was the last comprehensive radial velocity study conducted on Antares A until the work presented below.

Brightness Variations – The first conclusive study of the variable brightness of Antares A was conducted by Stothers & Lueng (1971), who found a period of 1733 days from AAVSO visual magnitude estimates. Most recently a period of 1650 ± 640 days was found by Kiss *et al.* (2006) and a period of 7000 days was noted by Percy & Terziev (2011). A similar study reported a short period of 350 days from the AAVSO photoelectric data (Percy *et al.* 1996). In the Hipparcos catalogue Antares is tagged as variable and is reported to have an amplitude of 0.134 ± 0.053 mag (van Leeuwen 2007) though no period is given. Cummings (1998) finds periods of 1000 days and 217 days from the Hipparcos data. Cummings (1998) also analyzes Tycho data and finds periods of 1111 days and 95 days. Further remarks on this subject will be made when we consider our analysis of the photometry of Antares A.

Chapter 5

5 The Parameters and Their Measurement

For the purposes of measuring the photospheric dynamics of cool stars from high resolution optical spectra one measures and analyses the spectral lines in a number of ways. In the following section we outline the typical measurement techniques, any alterations that were needed for our analysis and the typical interpretations that one can apply.

5.1 Measuring Granulation

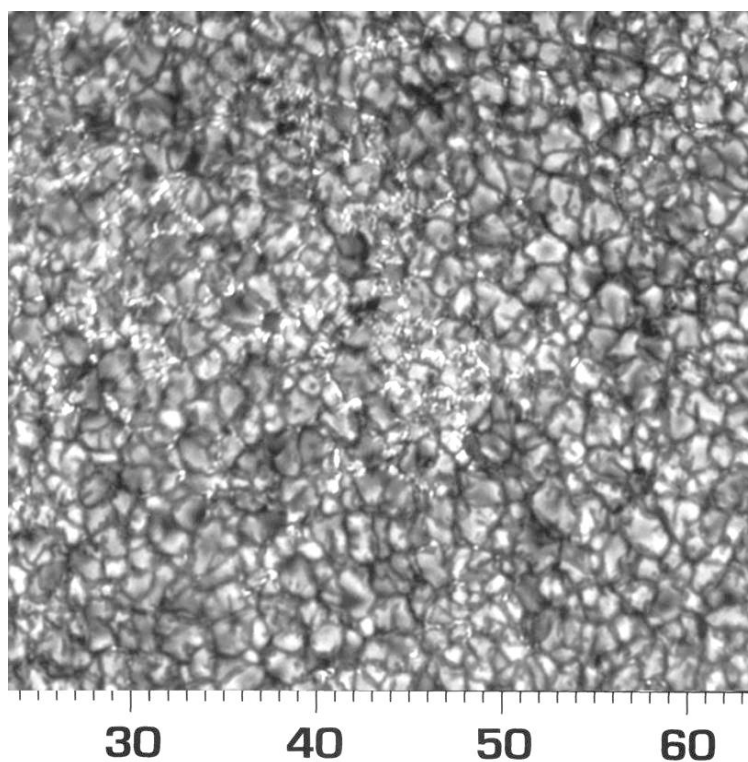


Figure 21: An image of granulation on the solar surface; bright granules are surrounded by dark lanes. Image obtained by G. Schamer using the Swedish Vacuum Solar Telescope, July 1997. Distance in 1000 km. (Shine *et al.* 1997)

Convection plays a vital role in a large number of stellar phenomena: mixing of stellar material, Li and Be deficiencies, internal distributions of angular momentum, carrying thermal energy through the convective zone, dynamo action (in combination with rotation) and the generation of acoustic and Alfvén waves. In cool stars we find that convection dominates the shapes of the spectral lines resulting in line broadening, line asymmetries and depth-dependent line core radial-velocity shifts. In addition to this, convection being inhibited causes starspots. The best-known and most easily observed effect of convection is the solar granulation pattern. The blotchy surface of the Sun is well documented, being first photographed in 1877 by M. Janssen (Janssen 1878). However, the link between the observed granulation and convection did not come until 1936 (Plaskett 1936). We now know that the granules are produced by the tops of convective cells. The bright material, located at the center of a granule (Figure 21), is hot rising material and the dark intergranular lanes are cool, falling material. Unfortunately, such informative images as that in Figure 21 are not available for stars other than the sun and thus evidence of granulation for other stars must come from other observations.

5.1.1 Macroturbulence

Macroturbulence is the term used to refer to the large-scale turbulent motions of stellar atmospheres, these motions cause Doppler shifts which are observed as broadening of stellar spectral lines. Initially such turbulence was modeled as being Gaussian and isotropic but by the 1970s it was becoming clear that this assumption was failing to agree with observations. However, observations of granulation in the sun led to the development of the radial-tangential model of macroturbulence; where a Gaussian distribution of velocity amplitudes is maintained but the velocity vectors are governed by granular motions, and are taken to be either radial or tangential in orientation, see Figure 22. In cool stars (spectral types G, K & M) the macroturbulence is dominated by such convective motions. Reviews of this topic can be found in Huang and Struve (1960), Gray (1978), Beckers (1981) and Gray (1988).

There are a number of methods one can use to measure the macroturbulence dispersion from stellar spectra. For stars with low rotational velocities the line broadening will be dominated by photospheric velocity fields. In such cases one can either observe the line widths directly or compute Fourier transforms of the spectral lines (details regarding Fourier analysis of spectral lines can be found in Appendix B). From such measures we see that macroturbulence dispersion increases with effective temperature and with luminosity class (Fig. 17.10, Gray 2005) a trend which agrees with theoretical convective velocities (Renzini *et al.* 1977). In the most luminous evolved stars one runs into observational difficulties, luminosity class Ia-Ib stars also have considerable microturbulence. So, while changes in line widths and observed broadening imply changes in the turbulent velocities, distinguishing macroturbulence from microturbulence is a non-trivial task, which requires synthetic spectral modeling. In addition, since the turbulence is highly unlikely to be Gaussian in the extreme atmospheres seen in red supergiants there is an additional layer of doubt that clouds the theoretical results as well.

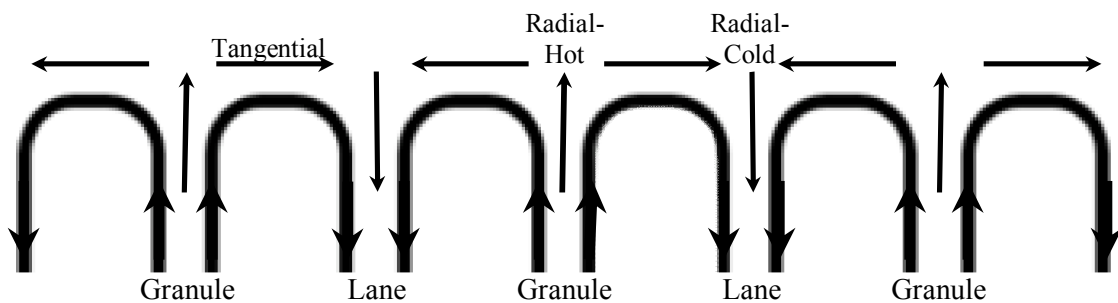


Figure 22: A schematic of granular motions. Radial-flow corresponds to the rising and falling material; tangential-flow corresponds to the layers where the material is turning over.

5.1.2 Spectral Line Asymmetries

Due to the motions of the photospheric material, we should see that the spectrum from the hot, rising material is blue-shifted and the spectrum from the cool, falling material is red-shifted. Also, since the granules are hotter than the surrounding lanes, they are also

brighter and so granule light dominates the combined spectrum. When we combine these effects, as in the case of an unresolved star, we see non-symmetric spectral lines such as that shown in Figure 23. Typically we measure line asymmetry by looking at the bisectors of spectral lines. The line bisector is computed from the midpoints of horizontal line segments that extend across the spectral line. The reader is directed to Appendix C for further details on the computation of line bisectors. One such bisector is shown in the right hand panel of Figure 23.

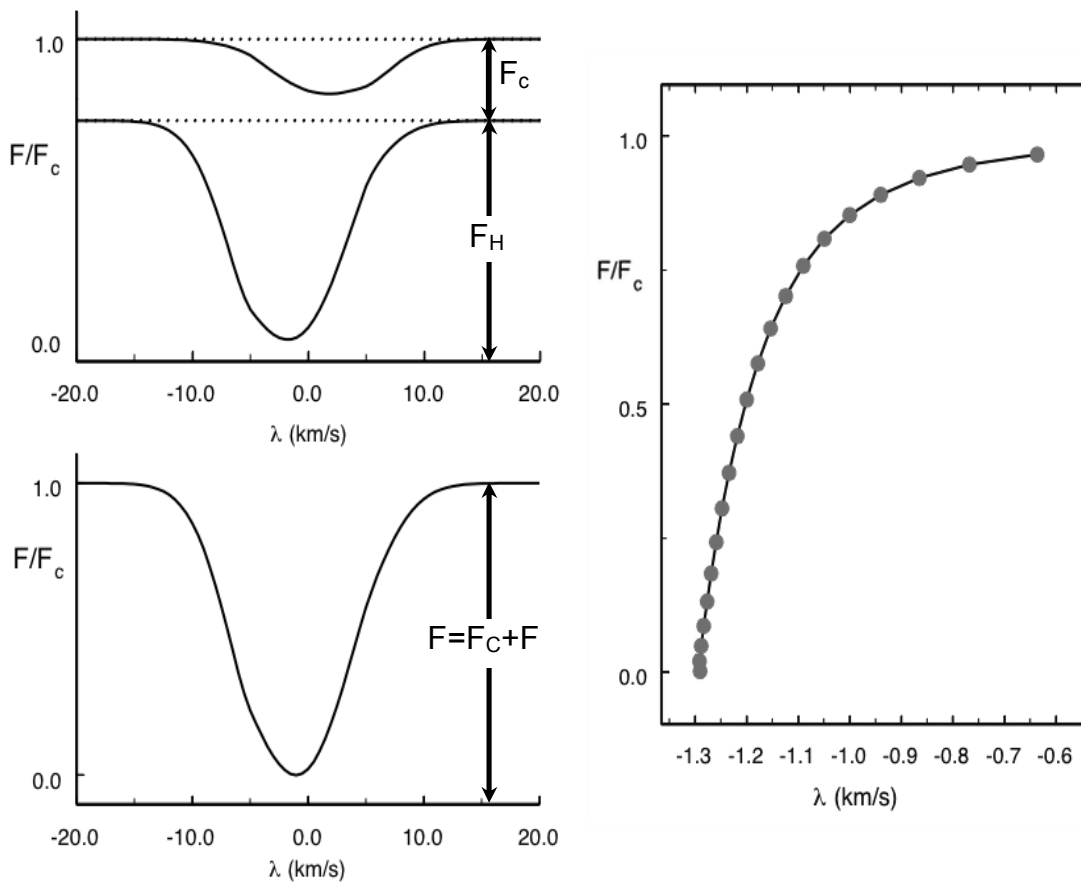


Figure 23: *Left* - Correlation between Doppler shift and line flux of the hot and cool plasma results in an asymmetric spectral line. *Right* - Asymmetry is more obvious when viewing the bisector of the spectral line.

The first detection of granulation asymmetries in unresolved stars was presented by Gray (1980). Since then many further detections have been made (see for example Gray 1981; Gray 1982; Gray & Toner 1986) and a progression of asymmetries across the Hertzsprung-Russell diagram has been seen for the various luminosity classes, as demonstrated in Figure 24. In general, one finds C-shaped bisectors for cool stars and reversed-C bisectors for hot stars a phenomenon that has resulted in the observationally determined granulation boundary, see Chapter 17 of Gray (2005) for further reading. The C-shape in cool stars is indicative of the convective-type motion outlined above. The changes in shape of the bisectors are indicative of changes in the nature of granulation amongst these stars. The larger the span of the bisector, the more pronounced the asymmetry, the larger the granulation velocity. Such an increase in granular flow-rate is seen with both increased temperature (Figure 24) and increased luminosity. Further, stars that are seen to undergo vigorous granulation (i.e. have bisectors with large velocity spans) also have blue-shifts in the cores of their strong lines. This is easily explained by recognizing that the strong granulation currents they experience will extend further into the atmosphere and thus will penetrate the layers where the strong-line cores are formed. Thus, as one might expect, the lines that show the largest velocity spans also show the largest core blue-shift, as can be seen in Figure 24.

Interestingly a number of papers (Gray 2008; Gray *et al.* 2008) report reversed-C bisectors in highly evolved cool stars. As stated above reversed-C shaped bisectors are usually associated with the hot side of the granulation boundary, their occurrence on the cool side could arise due to blending, maybe invalidating the use of the bisectors for such stars. However, Gray (2008) found no correlation between temperature variations and changes in bisector shape, meaning that both lines (study and blending) would need to have the same temperature dependence.

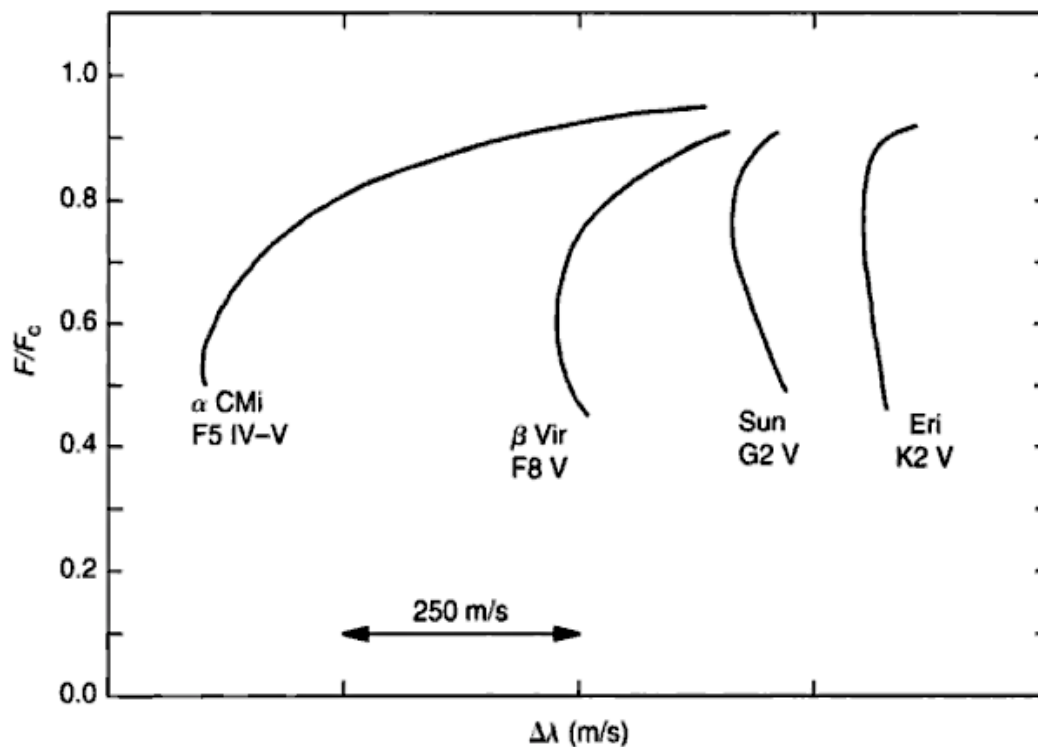


Figure 24: This sample of bisectors demonstrates the changes of asymmetry with spectral type in cool stars. The absolute shifts are meaningless and are solely included to order the bisectors by spectral type. The velocity span and curvature of the bisectors increase with effective temperature. (Gray 2005)

5.1.3 The Third Signature of Stellar Granulation

So termed because it was the third-signature to be used to indirectly observe granulation in unresolved stars, the third signature or differential velocity-shift of photospheric lines can be envisioned quite simply. In arguments similar to those used in the case of asymmetries we accept that the bright, hot and rising material dominates the integrated light from an unresolved star. Secondly, since granulation is essentially a signature of convective overshoot into the photosphere, since the material is no longer being propelled; the velocity should diminish with height through the photosphere. And thirdly, the line contribution function leads to a depth of formation relation that tells us

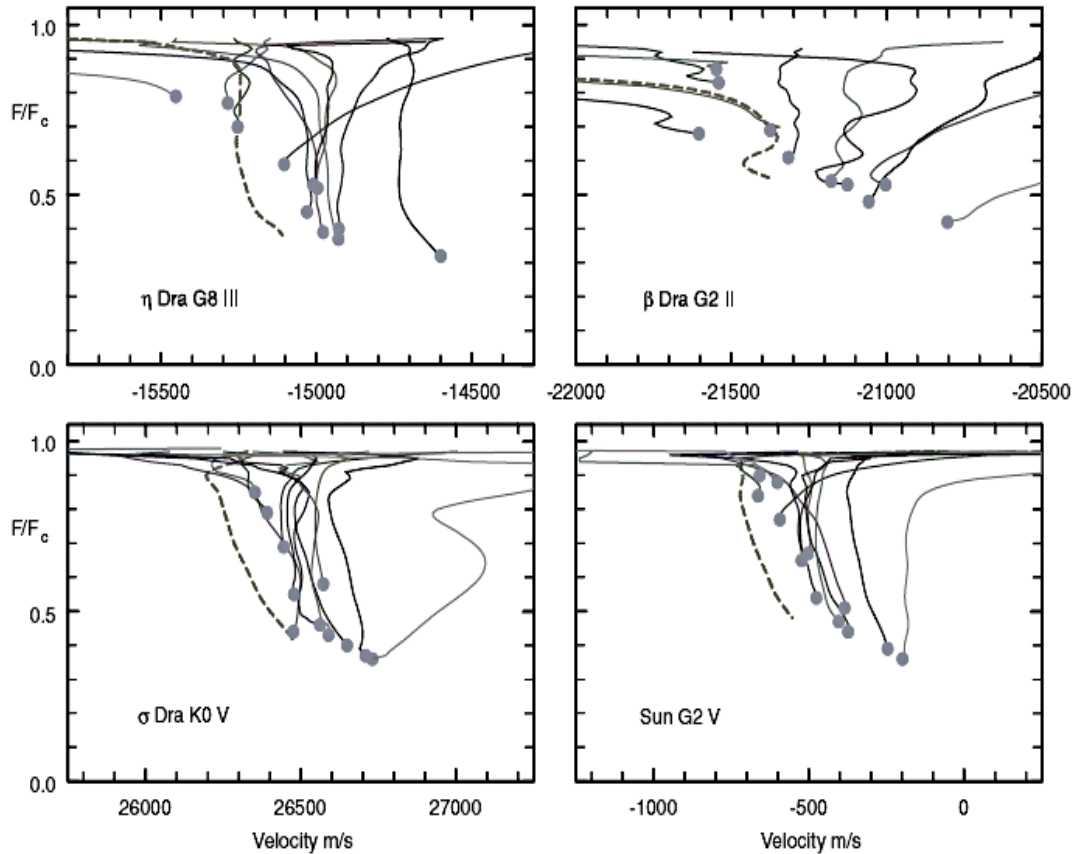


Figure 25: Sample of four third-signature plots. Fe I line-core positions (*points*), measured from line bisectors (*lines*), are plotted on an absolute velocity scale for lines of various strength. Weak-lines (core $F/F_c \sim 1$) are more blue-shifted (lower velocity) than strong lines ($F/F_c > 0.5$). The *dashed* bisector is from the $\lambda 6254$ line, a thorough discussion of the ‘overly’ blue position of this line is given by Gray (2009).

that the cores of strong lines are formed higher in the photosphere than the cores of weak lines. Combining these three effects one expects to see a systematic shift to greater blue-shift for weaker lines, see Figure 25 for an observational example. This effect has been clearly demonstrated for the sun since the 1980s (Dravins *et al.* 1981; Allende Prieto & Garcia Lopez 1998; Hamilton & Lester 1999) and more recently for other stars (Allende

Prieto *et al.* 2002). Further, Gray (2009) showed that the third-signatures, and thus granulation, in a number of cool stars is scalable to the solar case. This implies that the velocity gradients of stellar photospheres of cool stars are scalable to the solar velocity gradient.

One is tempted to ask, since the wings of the strong lines are also formed in similar layers to the cores of weak lines, why is it that bisector shapes and third-signature shapes are not more similar (compare Figures 24 and 25). Simply stated this is an effect of the fact that the third-signature contains only information gained from the rising material. If we recall Figure 23, here we see that the combined line-core is dominated by, if not entirely due to, the rising material. However, the line wings are also affected by the cool material. In the case of Figure 23 the flux ratios are 1:0 in the core and almost 1:1 in the red wing. Thus, the change in shape from the third-signature to the bisector is nothing more than a flux deficiency in the line profile. For a more thorough explanation see Gray (2010).

5.2 Predicting Rest Wavelengths

Figure 16 shows an example of an observed spectrum of Antares A; black arrows were used to highlight the Fe I lines usually used in this spectral region. There are eleven lines. Unfortunately due to the broadening seen in the spectra of Antares A, blending compromises the information available from the lines. There are number of other species that have lines in our spectral window that could also be used, and although no one line is less broadened than any other, by increasing the number of lines available for analysis one increases the reliability of the analysis. In order that our radial velocity precision is at its best, we require high-precision rest wavelengths. Traditionally we have used the Fe I lines because they have good quality laboratory rest-wavelengths available; precision ~ 10 m/s according to Navé *et al.* (1994). However, the scalability and universality of stellar third-signatures allows one to back engineer rest-wavelengths from stellar wavelengths using the third signature curve.

For this work narrow spectral lines with definite line-cores are required. To ensure precise wavelengths, three reference stars were selected: α Bootis (K2 III), α Arietis (K2 III), and γ Draconis (K5 III). The method of calculation is outlined here and can be seen for a larger selection of spectral lines in Gray & Pugh (2012):

- i. Compute line bisectors for Fe I lines, converting from wavelength to radial velocity using the rest wavelengths of Navé *et al.* (1994). Shown by the *lines* in Figure 26.
- ii. Plot bisectors and line-core positions on an absolute velocity scale as in Figure 26. This should reproduce the typical convective overshoot signature seen in Gray (2009) and Figure 25.
- iii. Plot the universal third-signature curve from Gray (2009) on the solar velocity scale. Shown by the *solid-black line* and upper x-axis in Figure 27.
- iv. Combine the universal curve with the Fe I core positions and stellar radial velocity scale, scale the velocity axis by the scale factors from Gray (2009) so that the universal relation describes the shape of the stellar points as in Figure 27.
- v. Compute line bisectors for non-Fe I lines using available low precision rest wavelengths, such as those available from the NIST (National Institute of Standards and Technology) database (Kramida *et al.* 2012).
- vi. Find core depth from the bisector and, using this depth coordinate, find stellar velocity position on the universal curve, Figure 28.
- vii. Use this measured velocity and the measured spectral wavelength to compute a rest wavelength.
- viii. Repeat for several exposures of the same star and for several stars until residuals are minimized.

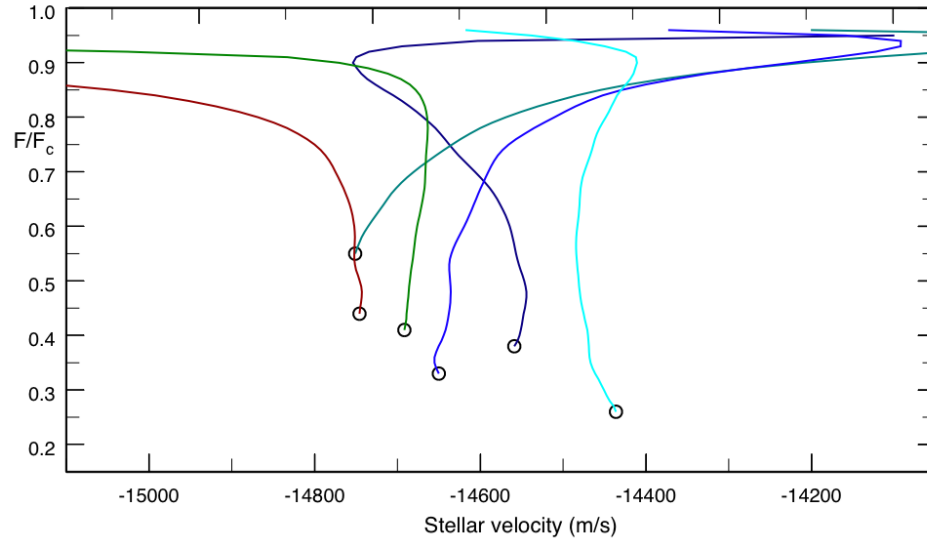


Figure 26: Six Fe I line bisectors computed from the mean lines of five exposures of α Ari. Core positions are marked with circles. The typical error on core position is <50 m/s.

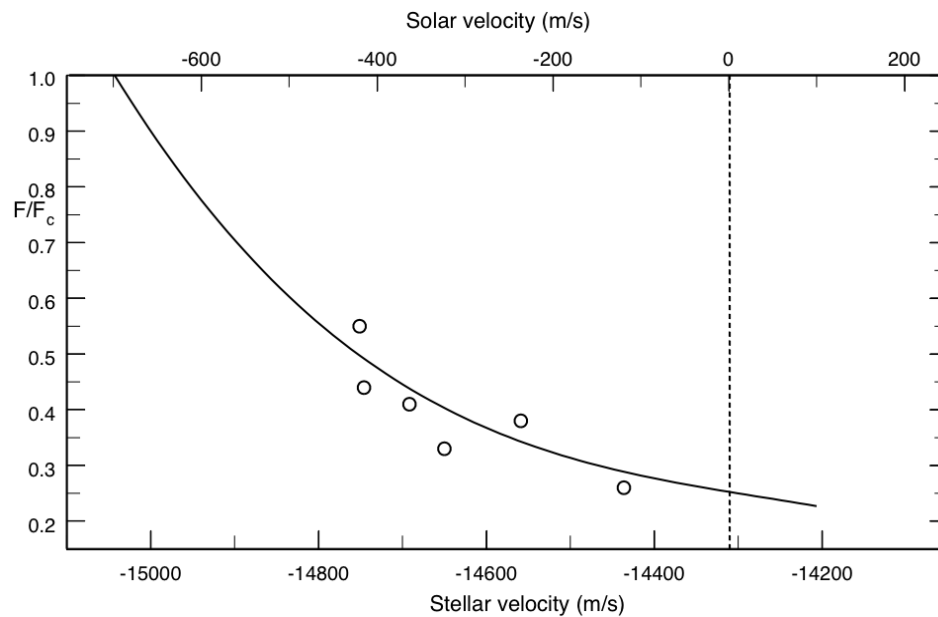


Figure 27: Bisector core points (*circles*) from Figure 26 plotted over the Universal curve (*solid-line*) from Gray (2009) using the scaling given in that work. Lower velocity axis gives the stellar velocity scale and the upper gives the solar velocity scale. The typical error on core position is <50 m/s.

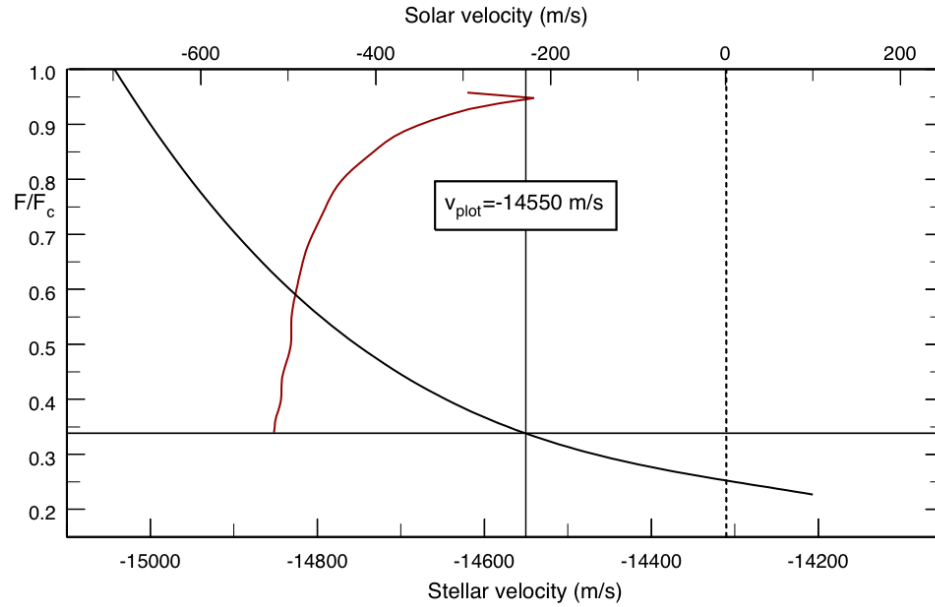


Figure 28: A bisector from a non-Fe I line taken from one of the five exposures. This bisector is assigned a core velocity using its depth on the Universal Curve.

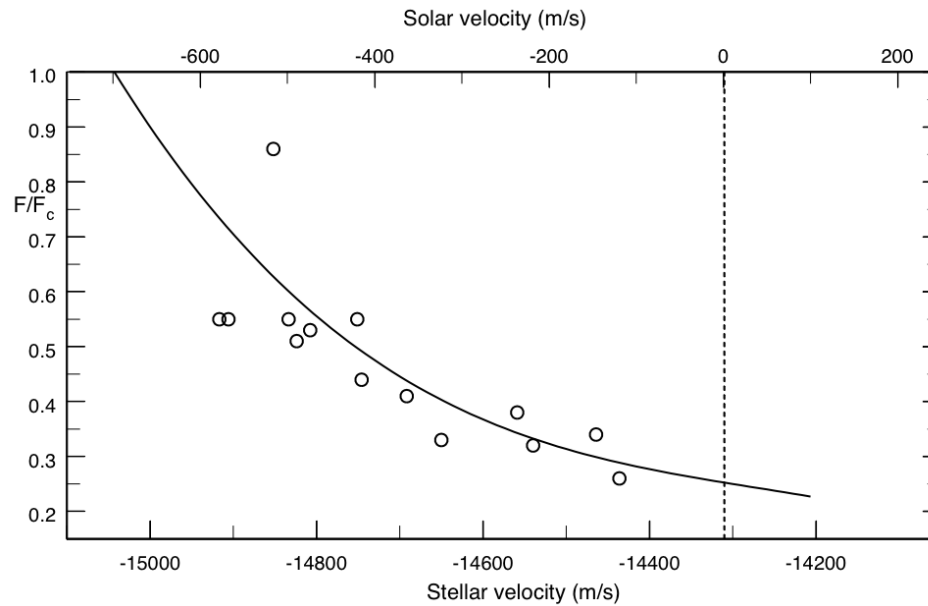


Figure 29: Final third signature plot including Fe I and non-Fe I lines; velocities for the non-Fe I lines are averaged over the five exposures. [This method was repeated for two other stars and the mean rest wavelength from all three contributions is what is given in Table 2]

Using this method we compute the rest wavelengths given in Table 2, the uncertainty is typically 30 m/s. It is known that radial-velocity varies with the excitation potential of the line used to calculate it. Such formation-depth mapping is well-documented for solar spectral-lines (Böhm-Vitense 1955). Our results from 2012 (Gray & Pugh 2012), however, demonstrate that these species (V I, Ti I, Si I, Fe II, Sc II) follow the third-signature of the Fe I lines very closely.

Table 2: Absolute wavelengths of non- Fe I lines. Wavelengths marked by † are taken from Gray and Pugh (2012) all others are calculated as outlined here. Note the small, occasionally, negligible difference between the values given here and those of Gray and Pugh (2012)

Wavelength (Å)	Difference from Gray and Pugh (2012) (Å)	Species	χ (eV)
6223.9870†	n/a	Ni I	4.10
6224.5059	0.0001	V I	0.29
6227.5490†	n/a	Unknown	-
6233.1987	0	V I	0.27
6237.3179†	n/a	Si I	5.61
6245.2194	0	V I	0.26
6245.6189	0	Sc II	1.51
6247.5596†	n/a	Fe II	3.89
6251.8252	0.0007	V I	0.29
6256.8999	0	V I	0.27

6258.1036†	n/a	Ti I	1.44
6261.1011	0.0005	Ti I	1.43
6266.3214	n/a	VI	0.28

5.3 Line Positions and Depths

One can compare the observed position of a stellar spectral line to its measured laboratory wavelength in order to determine the line-of-sight motion of the emitting/absorbing material using Doppler's equation. When one considers stellar atmospheres in this manner, one measures the rise and fall velocities of the photospheric material. Unfortunately, measuring the position of a spectral line which is heavily broadened is not straightforward task. Recall the typical spectrum illustrated above, the spectral lines of a typical red supergiant can span almost two angstroms, or ~ 100 km/s, thus assigning a radial velocity to such a line somewhat arbitrary. We could pick any part of line from which to measure our radial velocities. In a sharp-lined star one would normally use a bisector point, usually from within the line core. However, the lines of red supergiants are in general ill-suited to such an analysis. Gray (2008) was able to compute bisectors in the case of Betelgeuse for only a single line. As mentioned in the previous section we wish to ensure our results are as accurate as we can get them. In addition to calculating the rest wavelengths of several extra lines to allow ourselves more observational points, if we use a technique to measure the line positions that is not limited to whether or not a bisector can be computationally obtained, we can increase the number of position measures that we make.

Rather than using the usual method of determining the position based on the core position of a bisector, we instead fit a vertically oriented parabola to the core of the spectral lines and consider its vertical axis of symmetry to be the line core position. An example of the parabola fit is shown in Figure 30. We typically fit 12-20 points through the core of the line depending on blending and asymmetry. From the comparisons such as those shown in Figure 30, we estimated an expected measurement error from the signal-to-noise of the

exposure, the line flux compared to the continuum flux, the slope of the line at the final points used in the fit and the number of points fitted. Typical measurement errors calculated in this fashion are ≤ 110 m/s. We assigned each wavelength/radial-velocity measure a weight based on this expected error. These individual measures are then used in two ways.

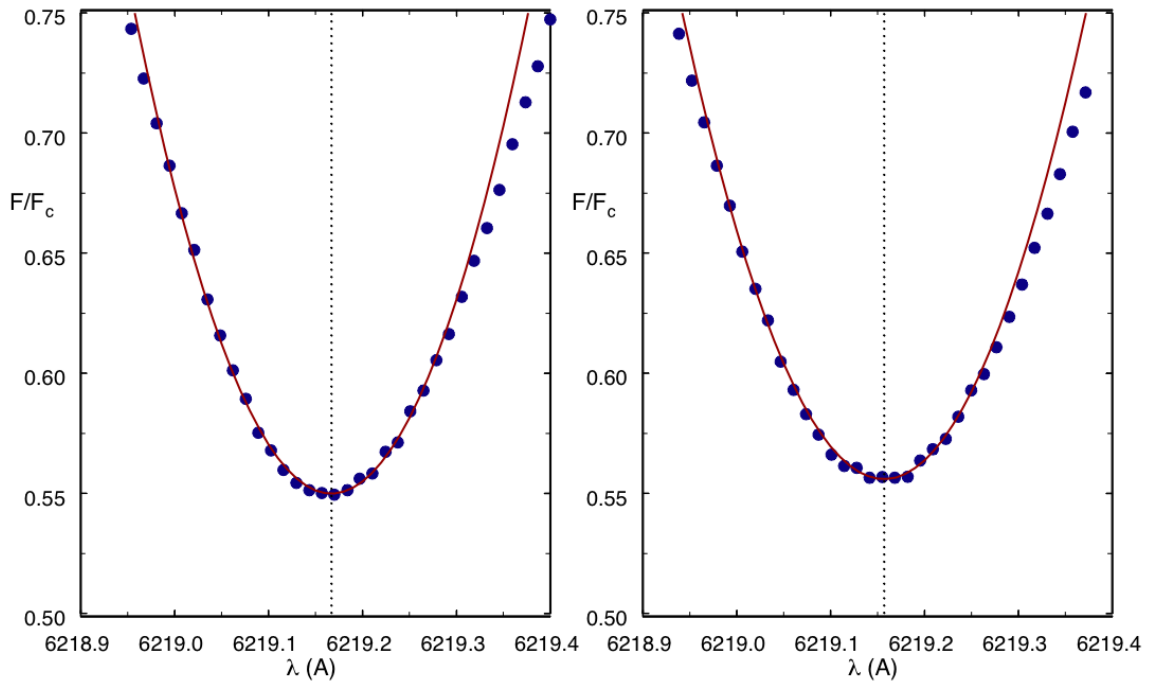


Figure 30: Example of core parabola fitting. *Left* – Exposure from April 2008, $\lambda=6219.1659\text{\AA}$. *Right* – Exposure from May 2008, $\lambda=6219.1562\text{\AA}$.

Firstly, we compute a weighted mean radial velocity for each exposure. Thus, we can study the temporal changes in the average line-of-sight velocity of the stellar atmosphere or the star, depending on interpretation. When used in this manner we compute a weekly scatter by comparing several measures taken over a few nights. In Figure 31 we show the exposure mean radial velocity measures taken over several nights in 2008, 2009 and 2010. Weekly scatters are estimated from the standard deviation of groups of points, such as those shown delineated by the red rings. Points are typically grouped in 10-day intervals, though occasionally there is only one point per 10-days and thus that point is grouped with the closest measures, providing that it makes sense within the radial

velocity trend. For each subset of exposures we compute the weighted mean, the standard deviation, and the error in the mean. The resulting errors in the mean for the subsets shown in Figure 31 are 63 m/s, 72 m/s, and 58 m/s from top to bottom. This error varies between subsets and we find that the average error over all data is 83 m/s. This is smaller than the typical measurement error (given above). Thus, the parabolae fitting technique is accurate enough that our measurement precision is not further lowered.

Secondly, the radial velocity measures of individual lines can be averaged over a series of nights to form third-signature plots. The scatter here is calculated in much the same way as those found above only we use the individual radial velocity measures rather than the exposure mean. In Figure 32 we show examples of the radial velocities of one weak line, one intermediate strength line and one strong line for the same time interval. As for the previous case for each set we computed the mean, the standard deviation, and the error in the mean for the three groups shown in Figure 32 are 106 m/s, 107 m/s and 78 m/s from weakest to strongest. This scatter is ~ 1.5 times larger than the scatter calculated using the means from all lines across the spectrum, however they are still approximately equal to or less than the measurement error. Thus, we can conclude that this measurement technique is sufficiently accurate to construct third signatures.

In Figure 32 we see that the weak lines demonstrate slightly higher (less negative) radial velocities than the intermediate strength and strong lines. This is the first hint that the third-signature shape of Antares A is different to the solar case. A result which is consistent with other high luminosity stars (Gray & Pugh 2012) and will be discussed further in the following chapter.

We also use the fits shown in Figure 30 to measure the normalized line fluxes for use in both the third-signature plots and in the line-depth ratios. Again we estimate the measurement errors in the same manner as outline above and we find a typical measurement error of 0.005 (or 5°K). In Figure 33 we show a single example for the line-core fluxes and a single example for the line-depth ratios. In the case of the continuum normalized line-core flux from the sample of Figure 33, we determine an error in the mean (or scatter) of 0.001 and for the 6252/6253 line-depth ratios we find 0.004

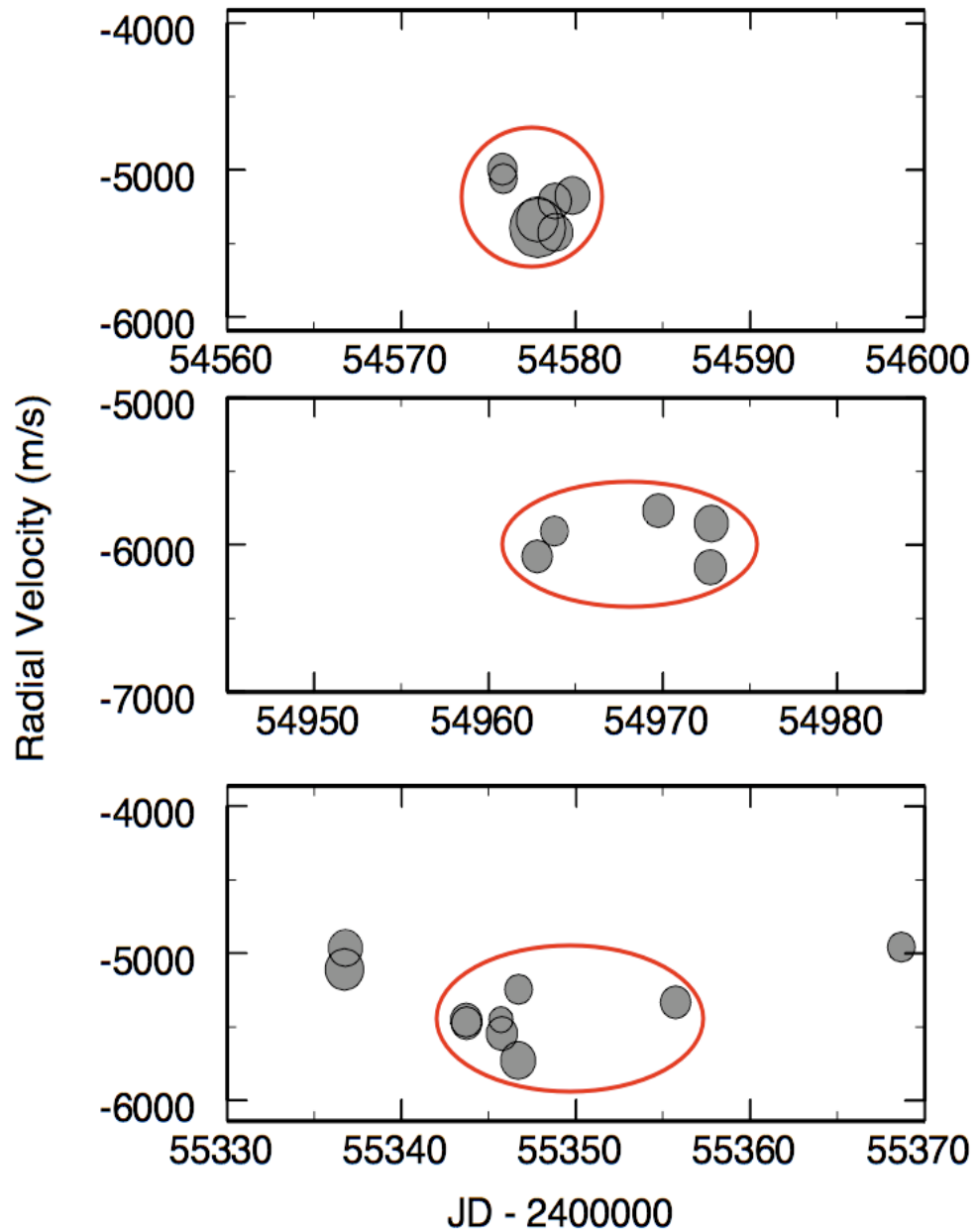


Figure 31: A sample of exposure mean radial velocity measures as a function of Julian Date. Each panel highlights a different section of the data; symbol sizes reflect the signal-to-noise ratio of the exposure. The *red* ‘rings’ enclose the subsets of data from which we compute the scatter. The scatter is 63 m/s, 72 m/s, and 58 m/s respectively.

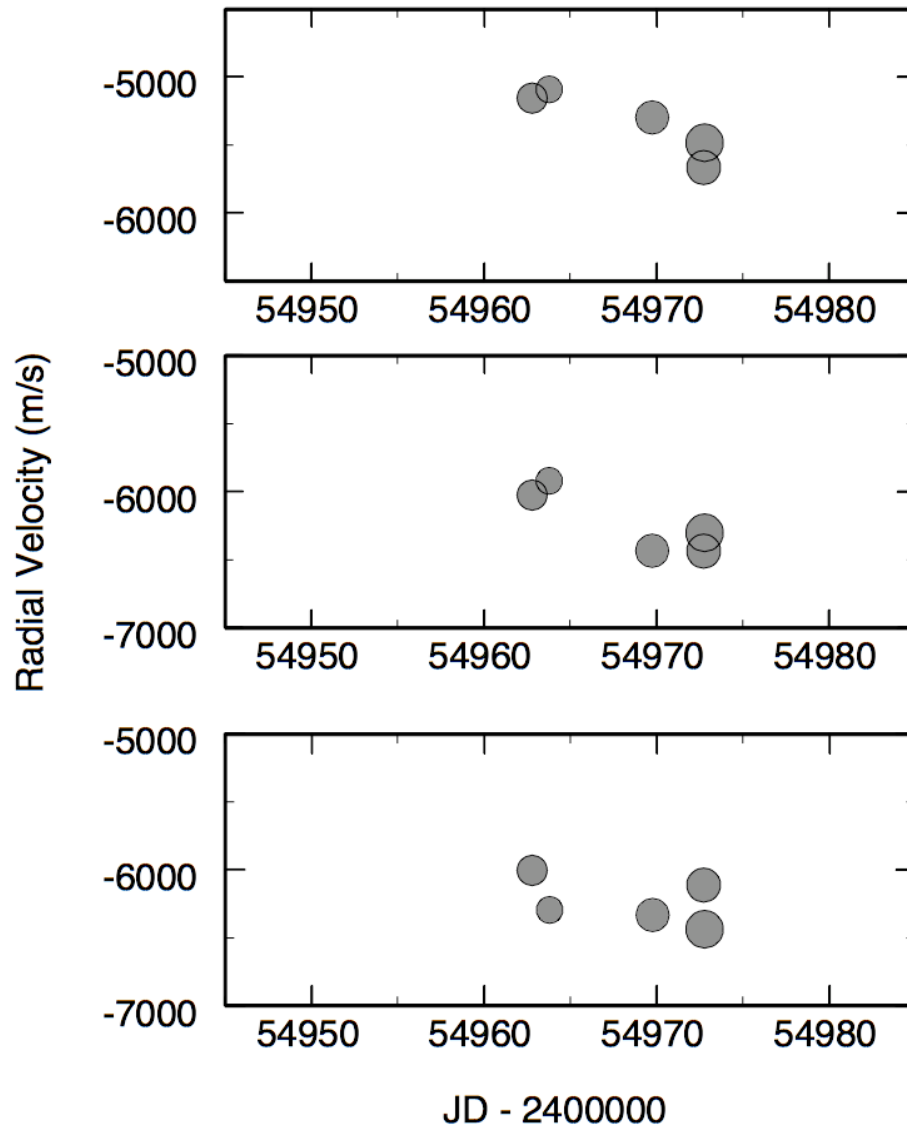


Figure 32: A sample of the core radial velocities for lines of three different depths. Symbol sizes reflect the signal-to-noise ratio of the exposure. The top panel shows measures for a typical weak line, the middle panel shows the measures for a typical intermediate strength line and the bottom panel shows the measures for a typical strong line. Point scatter is fairly similar amongst the three data sets indicating that the scatter is not greatly increased from one group to the next.

(4°K). As above these are typical, though not entirely representative, and some portions of the data may suffer from more or less scatter. For the purposes of our analysis of Anates A we used the weighted mean line-depth ratio of the 6252/6253 and 6233/6232 vanadium-iron pairs. The average over all exposures of the error in the line-depth ratio means is found to be 0.003 (4°K).

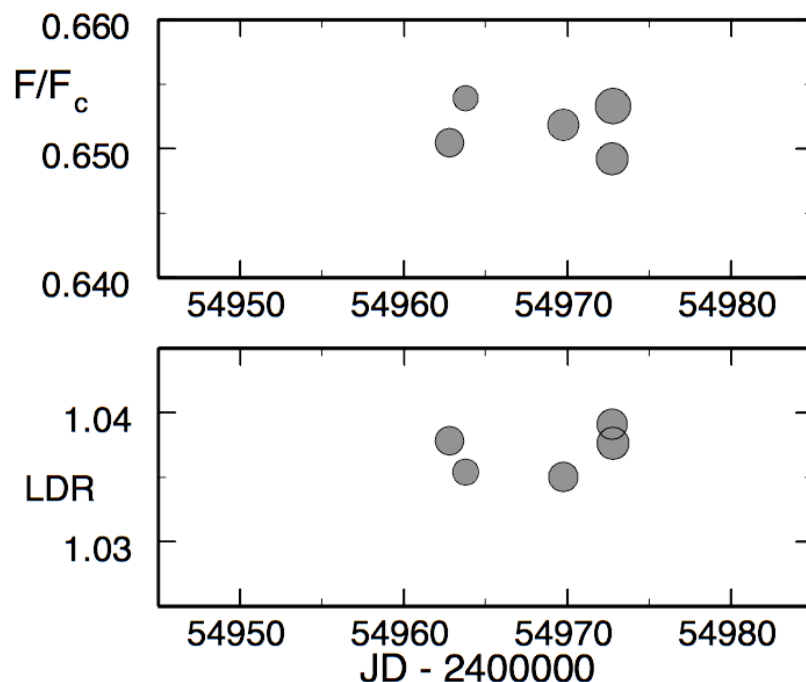


Figure 33: Sample of the temporal variations of the line-core flux in the *top* panel (for the 6241Å line) and the line-depth ratio (6252Å/6253Å) in the *bottom* panel. Both measures show little scatter, demonstrating the accuracy with which one is able to measure these quantities.

The purpose of the preceding section was not only to outline the method by which our measurements were made but also to demonstrate that the use of such a technique does not decrease the accuracy of our measurement to the point that our measurement precision is jeopardised.

Chapter 6

6 Analysis

65 spectra of Antares were collected during the three observing seasons of 2008, 2009, and 2010. A typical exposure was shown in Figure 16. The spectral observations made for this thesis were analyzed in conjunction with photometric data sourced from the AAVSO archive and the Hipparcos catalogue (van Leeuwen 1997) along with data from previous radial velocity studies (Spencer-Jones 1928; Evans 1961; Smith *et al.* 1989). This chapter outlines the analytical methods used to study the variability of Antares A (and in some cases a handful of other red variables) and interprets the results.

6.1 Brightness, Temperature and Radial Velocity

Our initial discussion focuses on the variability of brightness, temperature and radial velocity and compares the timescales, amplitudes and phases of these variations to build a picture of the nature of the variability. Here we shall present the data and, once all of the measures are at our disposal, discuss the variations of differing lengths separately. We begin by reviewing the AAVSO visual data. Since the focus of this thesis is majoritily the spectroscopic variations, for the purposes of examining the photometric variability we focus of Fourier amplitude spectra and historical measures. There are, however, other techniques that one may use and that can have more success these include wavelet analysis and auto correlation. A nice, thorough review of these methods and their applicability to various types of variable stars can be seen in Templeton (2004).

6.1.1 Brightness Variations

The AAVSO International Database holds over 20 million brightness estimates dating back over 100 years. For Antares the data consist of over 1000 magnitude estimates spanning more than 60 years. These data are of lower precision than research quality

photometry but provide unprecedented coverage. These magnitude estimates have been used in a handful of many-star studies of the photometric variations in red supergiants and/or small amplitude semi-regular variables (see for example Stothers & Lueng 1971; Percy *et al.* 1996; Kiss *et al.* 2006; Percy & Terziev 2011).

6.1.1.1 The AAVSO Brightness Estimates

There are certain caveats involved with using this data however, especially the visual estimates – which of course cover the greatest observational window. For this thesis we need to remain particularly aware of the limit placed on the observations of Antares. Our spectroscopic requirement, that we prefer bright targets, is a detriment to photometric studies. In fact Antares' magnitude is detrimental since suitable reference stars are difficult to identify for the brightest objects. To make visual estimates a reference star of slightly low magnitude and another of slightly higher magnitude are required. Fewer of these are available as the study star increases in brightness. In addition, the visual estimates are recorded only to an accuracy of one tenth of a magnitude; thus the AAVSO suggest that their data are binned in intervals of 7-10 days and give the expected standard deviation within a bin to be 0.2-0.3 mag for red stars.

Following this advice, and to make the results more comparable to those of previous authors, the data were binned in 10-day intervals. The resulting light curve is shown in Figure 34. As expected from previous investigations we see variations on more than one time scale and find a mean magnitude of 1.0. Inspection of our 10-day bins reveals standard deviations that are typically ~ 0.2 with standard errors in the range of 0.06-0.2. We note here that in this thesis we consider only the visual estimates and not the photoelectric V magnitudes, since we did not wish to introduce spurious effects related to integration of the two data sets.

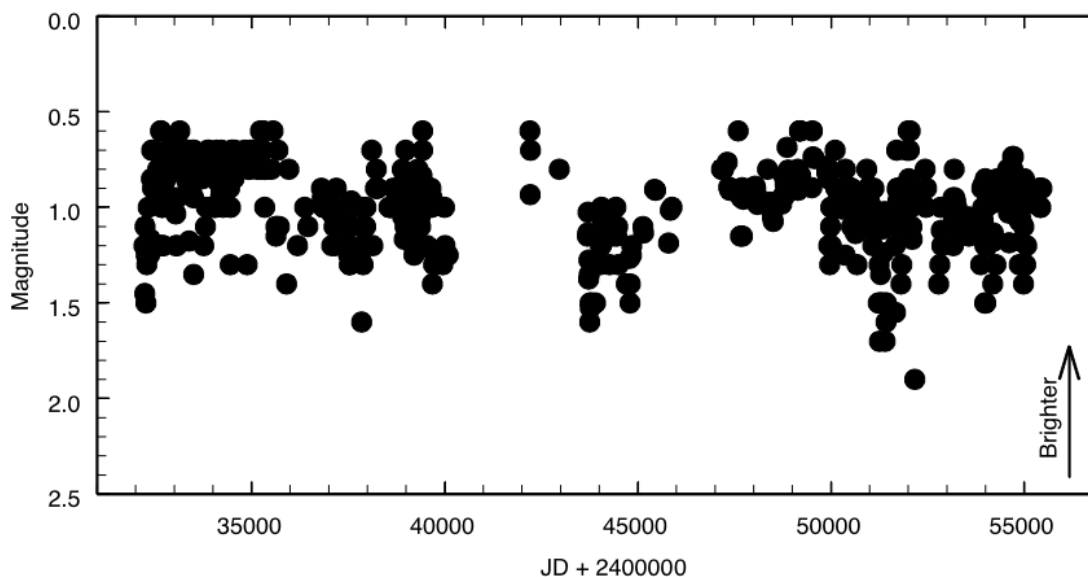


Figure 34: AAVSO light curve of Antares A the data are binned in 10-day intervals. Each bin contains between one and around ten individual measures. The standard deviation of the binned data is 0.21, while the standard deviation in any one bin is typically 0.2, with a typical error in the mean of 0.106.

To analyze the timescales associated with the variations, Fourier amplitude/power spectra were computed using both the WINDOW algorithm provided by D. F. Gray and Period04 (Lenz & Breger 2005). The initial Fourier power spectrum of the data is shown in Figure 35. In this power spectrum three frequency peaks are apparent; the window function has been adjusted to coincide with the first peak.

The first peak, seen in the amplitude and power spectra, constructed from the AAVSO magnitude estimates (Figure 35), occurs at a frequency of $(1.40 \pm 0.02) \times 10^{-4}$ cycles/day or a period of 7140 ± 10 days and has an amplitude of 0.13 ± 0.01 mag. This coincides with the, approximately, 7000-day period reported by Percy & Terziev (2011). The second highest amplitude peak in Figure 35 occurs at approximately 360 days and coincides with the alias of the primary peak. One must be cautious in assigning a period of approximately one year to any variability since it may be associated with the orbital

period of the Earth. This 1-year period is likely spurious as suggested by Percy & Terziev (2011) for similar data.

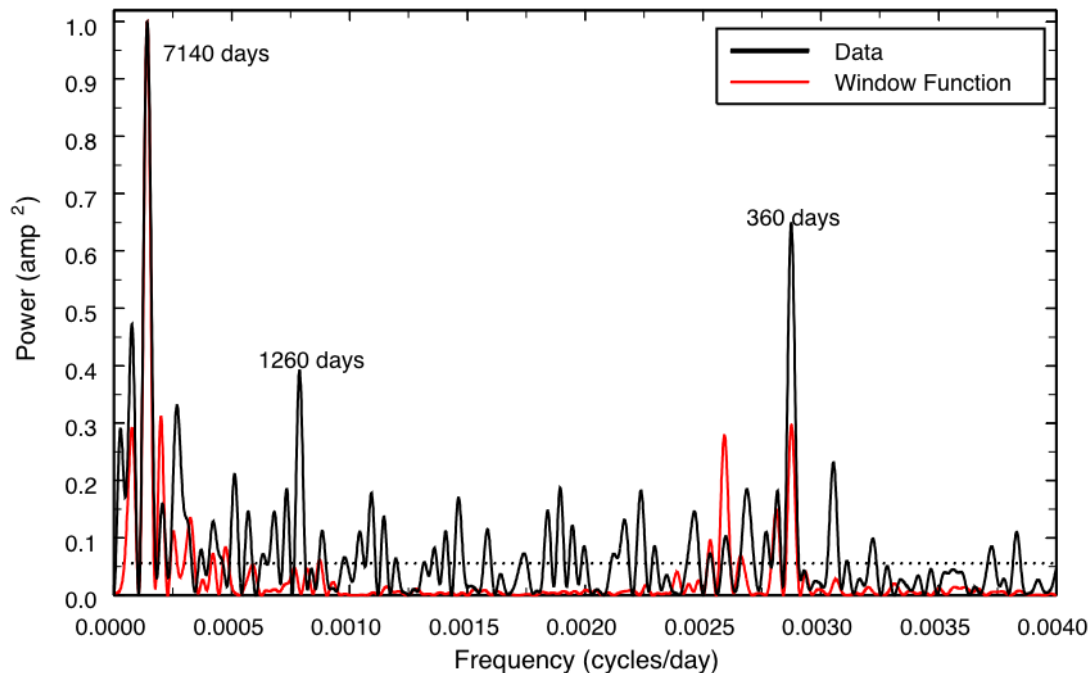


Figure 35: Fourier amplitude spectrum of the 10-day binned AAVSO light curve of Antares A. The data are given in black and window function adjusted to the frequency of the primary peak is shown in red. Dotted line shows the noise level. The primary amplitude peak occurs at 7140 ± 10 days.

To obtain a better understanding of the actual periodicity/variations demonstrated in the AAVSO photometry the primary period (~ 7140 days) is subtracted from the data and the amplitude/power spectrum reexamined. This is done by subtracting the corresponding sinusoid from the binned data. The sinusoid used is shown by the dotted-red curve in Figure 36. The equation for this sinusoid is determined from the amplitude and frequency of the peak in the power/amplitude spectra and is $y = 0.13 \sin(2\pi 0.00014 + 0.035) + 1.00$, the phase is found through phasing the resulting sinusoid with the data and

reducing the residuals. The resulting phase is 0.035 ± 0.003 . The whitened power spectrum is shown in Figure 37. With the primary period subtracted, the 360-day peak also disappears, supporting the conclusion that this peak is spurious. Percy & Terziev (2011) found many such ~ 1 -year periods using AAVSO visual magnitude estimates, the prewhitening completed here suggests that such periods are artificial. In Figure 37 we see a remaining power peak with a frequency of 0.000789 ± 0.000003 cycles/day, or a period of 1261 ± 5 days, and an amplitude of 0.09 ± 0.01 mag. The periods found from this data will be discussed further individually once we have reviewed the other data.

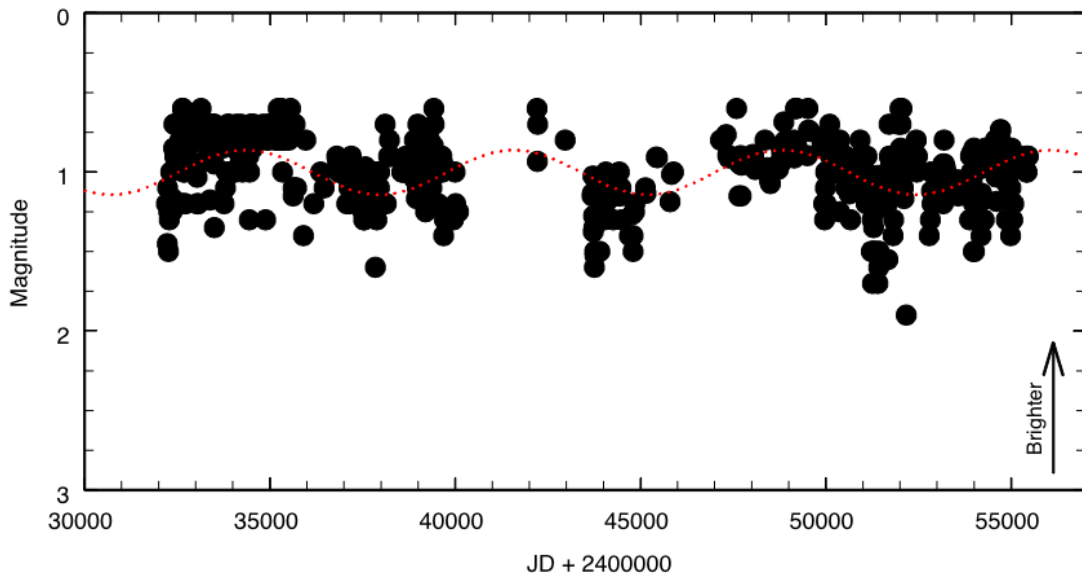


Figure 36: AAVSO data (as Figure 34) shown with the sinusoid corresponding to the 7140-day timescale plotted in red. The equation for this sinusoid is $y = 0.13 \sin(2\pi 0.00014 + 0.035) + 1.002$

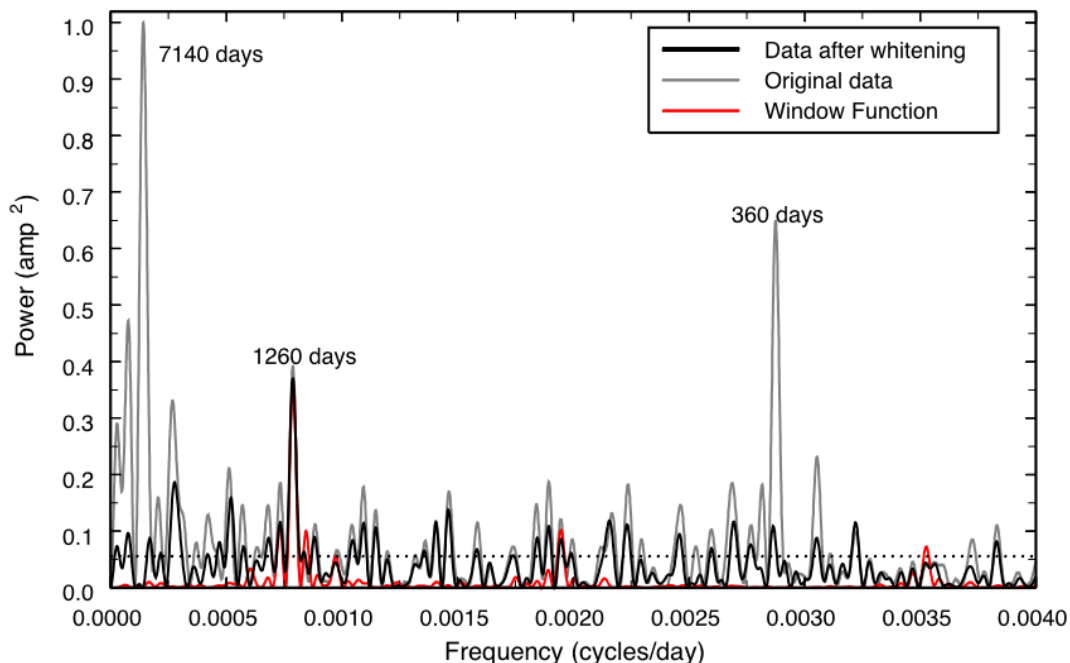


Figure 37: Power spectrum after prewhitening of the 7140-day variation. The 360-day peak has also disappeared leaving only the 1260-day peak. The window function has been scaled to the position and power of the 1260-day peak.

6.1.1.2 Hipparcos Photometry

Hipparcos (the **H**igh **P**recision **P**arallax **C**ollecting **S**atellite) was launched in 1989 and operated until 1993. Although an astrometric mission, to precisely determine the distances to stellar objects, a byproduct of the mission was high precision photometry of the sources. For the purposes of this study we have constructed 1-day bins of the available data, the 1-day binned light curve is shown in Figure 38 with the AAVSO 10-day binned data for the same epoch. There is good agreement between the two data sets over this portion of the AAVSO data.

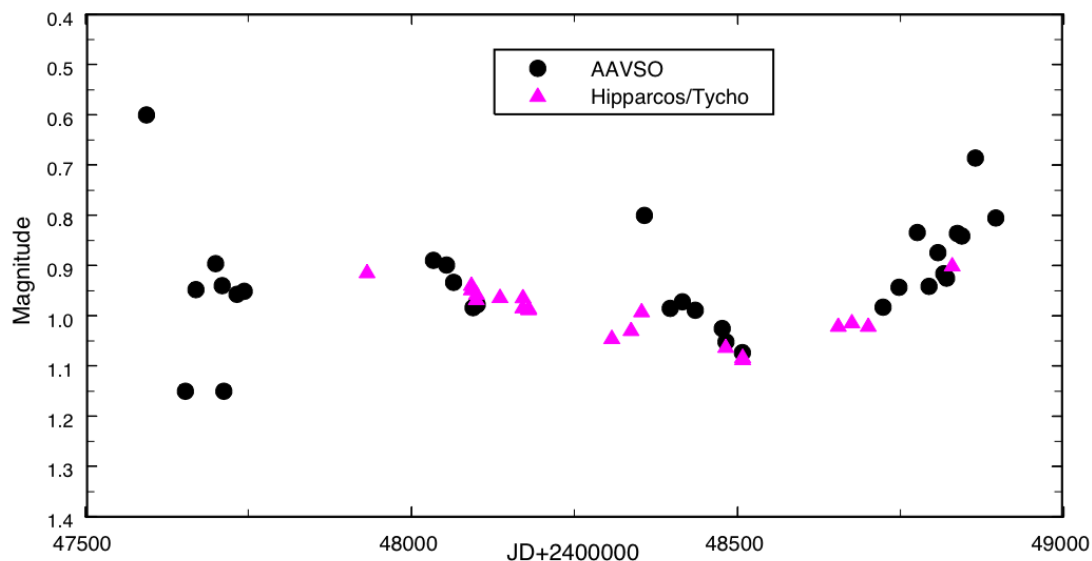


Figure 38: Light curve of Antares A. ▲ - Hipparcos & Tycho magnitudes in 1-day bins. ● - AAVSO magnitude estimates in 10-day bins. Two timescales of variation are seen in the data. The agreement between the two sets is surprising giving the vast difference in precision – recall the typical error on an AAVSO point is 0.2 mag. Quoted measurement errors for Hipparcos are 0.042 mag.

While not shown here we did compute a Fourier power spectrum of the Hipparcos data. We found a primary power peak at 1055 days, a period that is longer than the data window which spans 897 days. This period is in fair agreement with those of Cummings (1998) who reports periods of 1000 days and 1111 days. However, since the period detected is longer than the data window one should be cautious. Inspection of the light curve, shown in Figure 38, shows that one could simply be observing part of a longer trend. Figure 39 shows the light curves of Figure 38 again but with a sinusoid corresponding to a 1260-day period (from Figure 37). The shape of the Hipparcos light curve can be explained by the period found from the AAVSO data. This timescale will be discussed in comparison with others later in this chapter. Looking at the curves of Figures 38 and 39 one sees that there is a shorter timescale (around 200-days) that is most obvious between JD 48250 and 48500. This fits well with the previous findings of 217

days by Cummings (1998). From the Fourier power spectrum on finds a peak at 170 days.

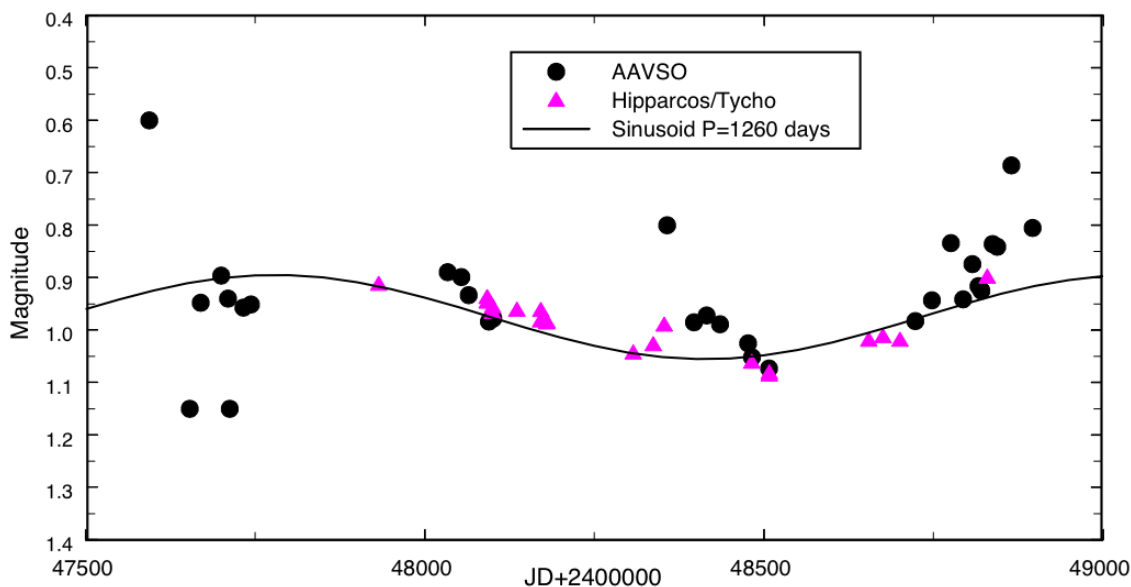


Figure 39: AAVSO (●) and Hipparcos (▲) light curves with a 1260-day sinusoid (solid line). The sinusoid is calculated using the results from the Fourier analysis of the AAVSO data. The fit is not perfect as the 7140-day variation has not been accounted for.

6.1.2 The Radial Velocities and Line-Depth Ratios

Using the 65 spectra obtained of Antares, we performed a number of investigations. In this section we consider the variations in the line-depth ratios and the radial velocities, both of which will later be compared to the photometric variability.

6.1.2.1 Radial Velocities

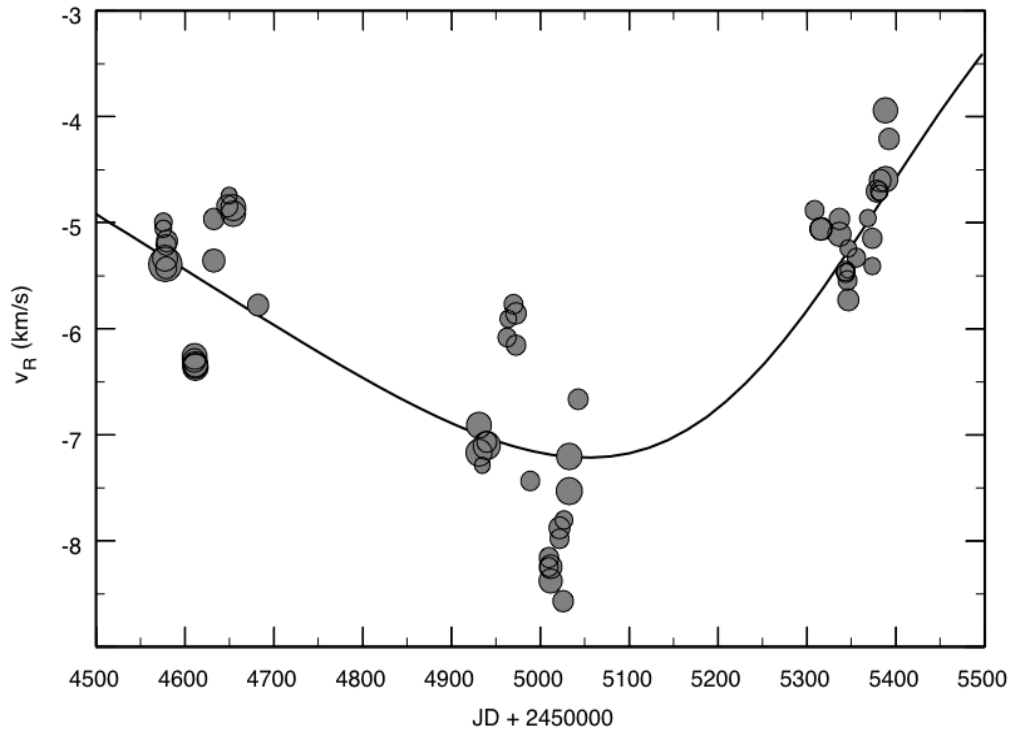


Figure 40: Radial velocity curve of Antares during 2008-2010. The size of the data points indicates the weight of the exposure, errors are typically smaller than the symbol size. The solid-line is the orbital solution given in Table 4. We see variations on more than one time scale.

Using the telluric lamps taken before and after the stellar exposures, we are able to accurately determine stellar wavelengths. The measurement errors were discussed previously and as pointed out there are typically 100 m/s. The first step in measuring the stellar radial velocity is to convert the wavelength of each line under consideration into a velocity. In this investigation we used ten Fe I lines and eight lines of other species, as listed in Gray & Pugh (2012) and in previous sections. A typical spectrum was shown in Figure 16, in that figure we depict the Fe I lines using black arrows and the lines of the other species using red arrows. The lines used vary in strength from $\sim 0.89 F/F_C$ to $\sim 0.45 F/F_C$ and exhibit large macroturbulence broadening, which is typical of cool supergiants.

The radial velocity curve of Antares is shown in Figure 40, it demonstrates variability on two timescales. The seasonal mean value varies considerably from one season to the next and we observe a minimum in 2009. The variation in the season means is consistent with the period ~ 2000 days that is often reported from radial velocity studies of Antares (Lunt 1916; Evans 1961; Smith *et al* 1989 amongst others). We also see variations on a shorter timescale, ~ 100 -days in the radial velocities. In the following section these two timescales are considered separately and compared to the variations in other observed parameters.

6.1.2.2 The Line-Depth Ratios

We estimated the temperature variability of Antares A from measured line-depth ratios, using the calibrations of Gray & Brown (2001) and Catalano *et al.* (2002). For this purpose we measured the line-depths of the 6233 V I to 6232 Fe I and 6252 V I to 6253 Fe I pairs. The mean line-depth ratios of these two pairs are used as the temperature index through the calibrations mentioned above. In Figure 41 we present the line-depth ratio as a function of Julian Day plotted with the radial velocities from Figure 40. The abscissa are offset by 70 days so that the line-depth ratios trace the same long-term shape as the radial velocities. Measurement errors are ~ 0.005 ($\sim 5^\circ\text{K}$). As with the radial velocity we observe both long-term and short-term temperature variations. The variations are $\sim 65^\circ\text{K}$ within a season and $\sim 160^\circ\text{K}$ if the temperature curve continues to mimic the radial velocity curve over the full cycle. The two timescales are considered separately below.

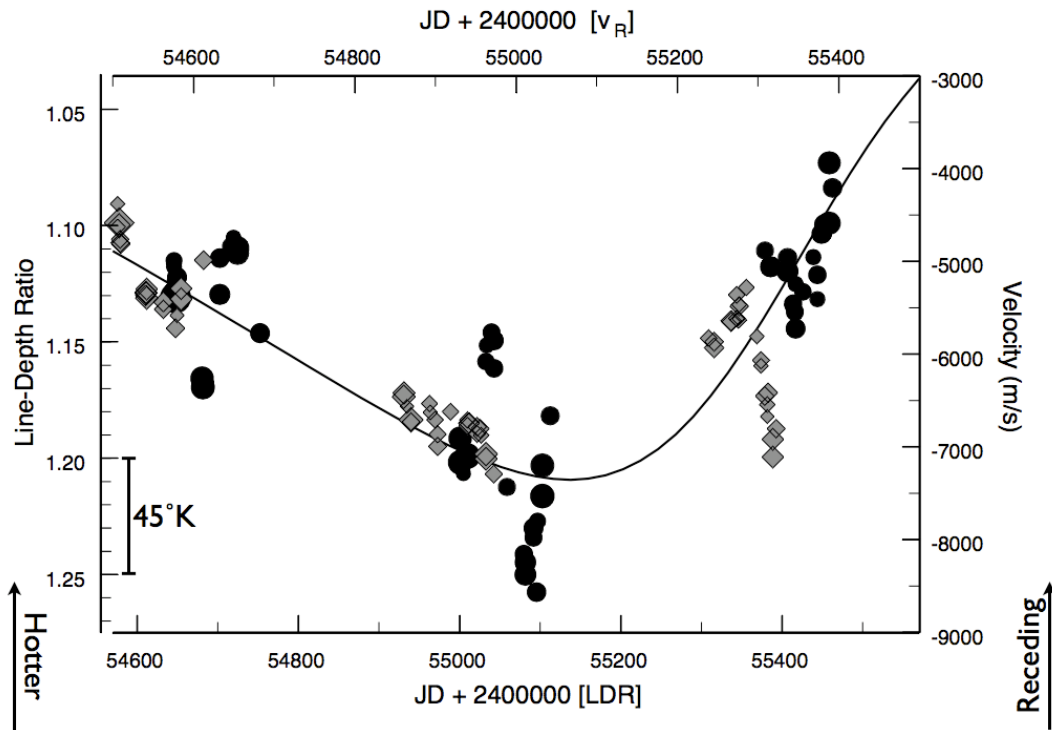


Figure 41: Line-depth ratios (◆) and radial velocities (●) as a function of Julian Day. Symbol size indicates point weight and in both cases the errors are smaller than the symbol size. Temperature increases inversely with line-depth ratio. The solid line shows the orbit solution from Table 4. The abscissa offset amounts to the minimum temperature occurring 70 days after the minimum in the radial velocity (maximum velocity of approach).

6.1.3 A Six-Year Variation

To further investigate the long-term trend seen in the radial velocity and line-depth ratios, our radial velocity measures were compared to the radial velocities of: i) Smith *et al.* (1989) obtained at the McMath solar telescope, ii) Evans (1961) obtained at the Cape Observatory, and iii) data recorded at the Lick Observatory before 1910 as summarized by Spencer-Jones (1928). Since our observations are on an absolute scale, aside from convective blueshifts (Gray 2009), we adjusted the zero point of earlier data sets to agree

with ours. The zero-point shifts are -700 m/s for the Smith *et al.* data and the Evans data, and -1450 m/s for the Lick data. Since there are short-term variations on the scale of 100 days, seasonal means, rather than individual data points, were used to study the six year variation. In the current context, we treat the short-term variations as extra noise, which is significantly reduced by using averages.

Table 3: Mean radial velocities. Errors include seasonal scatter and measurement errors.

Source	JD – 2400000 (days)	v_R (m/s)
Lick Observatory (Spencer-Jones 1928)	16656.9238	-4850
	16952.3200	-2090
	17336.1855	-3800
	17726.7520	-5350
	18011.8984	-7250
	18465.0566	-5430
Evans (1961)	34361.0742	-2980±760
	34532.4297	-2770±700
	34892.3945	-4500±500
	35552.6133	-6000±400
	35625.1641	-6050±770
	36022.9646	-3220±900
Smith <i>et al.</i> (1989)	46027.5000	7260±330
	46215.1172	6860±340
	46457.2109	-6160±300

	46633.9336	-5040±290
	46899.5547	-2200±400
	47251.5547	-2080±560
	47590.8008	-4000±480
Pugh & Gray (2013)	54613.4844	-5450±150
	54988.7695	-7240±190
	55358.4844	-4971±100

In order to compare our data with those presented in the literature, errors were calculated based upon the overall scatter of the data, which incorporates both the short-term variations and the measurement error. Thus the errors on our data points are a factor of two higher than the measurement errors shown in the previous chapter. Similarly the presented errors for the other data also incorporate both measurement error and short-term variability. The mean errors calculated in this manner are: i) for our data 150 m/s, ii) for Smith *et al.* 360 m/s, and iii) for Evans 640 m/s. Since Spencer-Jones (1928) presented only means of the Lick data no scatter analysis could be performed. We anticipate an error similar to that of the Evans data if not greater. The mean velocities and errors are presented in Table 3. Finally, the data were phased and the period and uncertainty estimated by minimizing the residuals. We find a period of 2167 ± 5 days or 5.93 ± 0.01 years. A phase plot is shown in Figure 42.

The radial velocity variation could be the result of either stellar pulsation or the motion induced by an orbit. It is well established that Antares A has a distant companion Antares B ($m_v=5.4$ mag, B4Ve) but the period is far longer than the time scales considered here, ~ 1200 years (Mason *et al.* 2001). We compute an orbit solution for the phased data, this is shown in Figure 43 and the orbit parameters are given in Table 4. Table 4 also compares our orbital elements with those found in the literature. It seems likely that the 2685-day (7.3-year) period given by Spencer-Jones (1928) is in error as

was suspected by Smith *et al.* (1989) and Evans (1957). From our orbital elements we determine the projected semi-major axis, $a_1 \sin i = (7.7 \pm 1.1) \times 10^7 \text{ km} = 111 \pm 15 R_\odot$, where i is unknown.

We do not see a secondary spectrum within our data. We could find no published evidence for any X-ray excess beyond that associated with the stellar wind and Antares B. Direct sighting of the secondary is unlikely given the brightness of Antares A. However, it should be within the grasp of modern interferometry if the photospheric contamination from Antares A is adequately subtracted. We find surprisingly few interferometric studies of this star. Tuthill *et al.* (1997) report no detections of bright/hot features in July 1992, but do see a spot 11 months later. Similar features on Betelgeuse and α Her A are interpreted as giant convection cells, not a companion star. Further, there are a large number of semiregular red supergiants that show *orbital elements* very similar to those shown here. In these cases the radial velocity is interpreted as arising from a long secondary period (Hinkle *et al.* 2002).

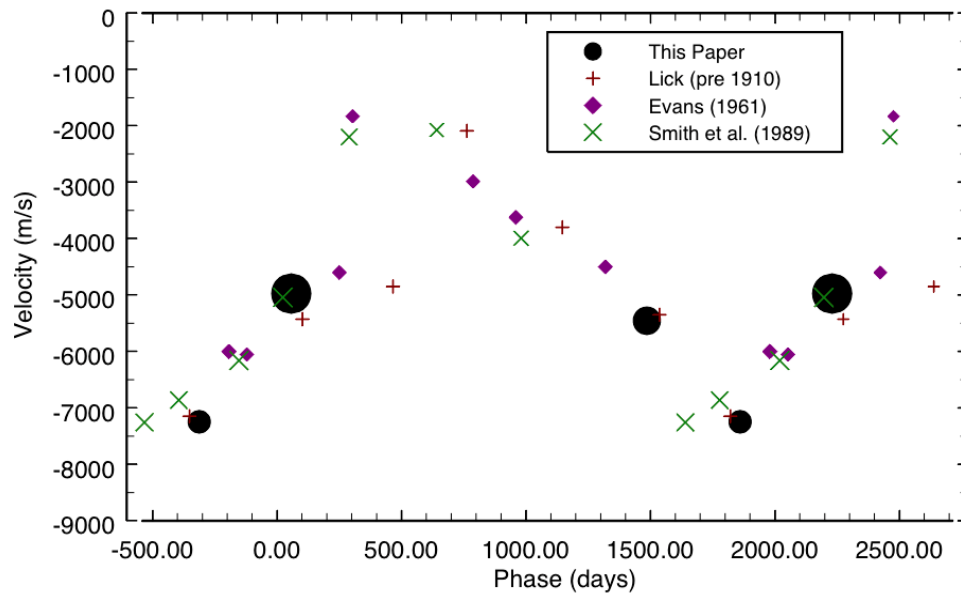


Figure 42: Mean radial velocities phased to a period of 2167 days. Symbols are; ● our data, + Lick data (Spencer-Jones 1928), ◆ Evans (1961), × Smith *et al.* (1989). Symbols sizes reflect the errors presented in Table 3; larger symbols for smaller errors.

Table 4: Comparison of Orbital solutions

Elements	Pugh & Gray (2013)	Halm (1909)	Spencer-Jones (1928)
e	0.30 ± 0.04	0.20	0.487 ± 0.054
ω (°)	249 ± 3	289	330.1 ± 7.1
P (days)	2167 ± 5	2120	2685 ± 29
K_1 (km/s)	2.73 ± 0.05	2.12	2.09 ± 0.15
V_0 (km/s)	-4.33 ± 0.05	-3.09	-3.18 ± 0.18
T_0 (JD - 2400000)	35626 ± 8	16674	17043 ± 37

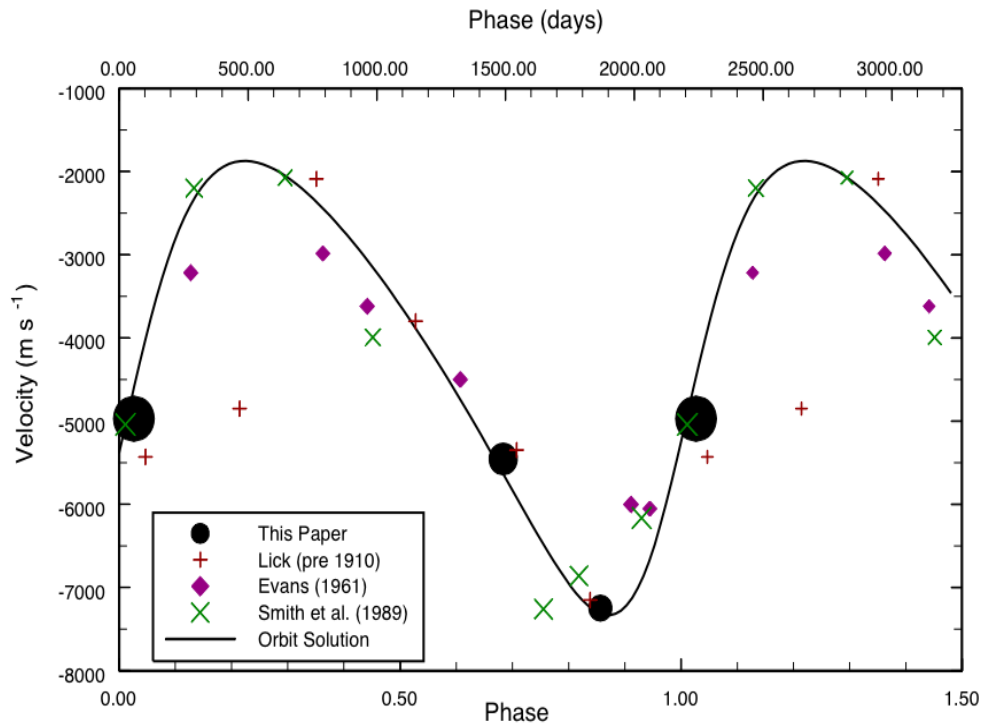


Figure 43: Mean radial velocities as a function of orbital phase. Symbols are; ● our data, + Lick data (Spencer-Jones 1928), ◆ Evans (1961), × Smith *et al.* (1989). Symbols sizes reflect the errors presented in Table 3; larger symbols for smaller errors. The solid line shows the orbital solution that is presented in Table 4.

The associated variation in temperature (Figure 41) could be produced by a stellar companion in two ways: it could result from (i) a close companion heating the surface of the primary, as is seen in other systems (e.g., Wilson 1990) or (ii) a close degenerate companion influencing the gravitational field could cause reduced surface gravity in a localized area as it orbits, leading to gravitational darkening and cooling. In this case one would expect the temperature minimum (or maximum) to occur after maximum velocity of approach as we see here, however the orbit solution constrains the phase shift to ~ 280 days not the 70 days that we see. In fact, to meet the 70-day requirement the orbital eccentricity would have to exceed 0.7. This eccentricity is incompatible with our radial velocity curve which can, in the extreme if we ignore the point weighting and suggest that the amplitude is somewhat larger than observed, be fit with an eccentricity of 0.45.

The asymmetry of the radial-velocity curve is reminiscent of Cepheid behavior, with a steeper rise than fall, but obviously Antares lies in a totally different part of the HR diagram. The phase shift of the temperature relative to the radial velocity is similar to the behavior of Mira variables, in which the temperature minimum lags the radial-velocity minimum by less than 30% of the pulsation period (Mahler *et al.* 1997; Wood *et al.* 2004a, 2004b). Further, pulsation with long periods is the norm for cool supergiants (for example Stothers 1969; Heger *et al.* 1997; Guo & Li 2002).

Since the early data are quite noisy and our data do not cover a full cycle, the radial-velocity curve is not well defined. Instead, we adopt the orbital solution as a stand-in and integrate it to estimate the change in radius. Applying the rough projection factor of 1.35 (Gray & Stevenson 2007), we find $\Delta R \sim 165 \pm 22 R_{\odot}$. The error is estimated from the uncertainty in the orbit solution.

Antares A has a parallax of 5.89 ± 1.00 mas (van Leeuwen 2007) and an angular diameter of 41.3 ± 0.1 mas (Richichi & Lisi 1990). Combining the parallax and angular diameter gives a radius of $890 \pm 150 R_{\odot}$. Thus the radius changes by $19 \pm 4\%$ over the pulsation cycle. Adopting a Mira-type variation we assume that the maximum temperature coincides with the minimum radius, thus combining the estimated temperature variation

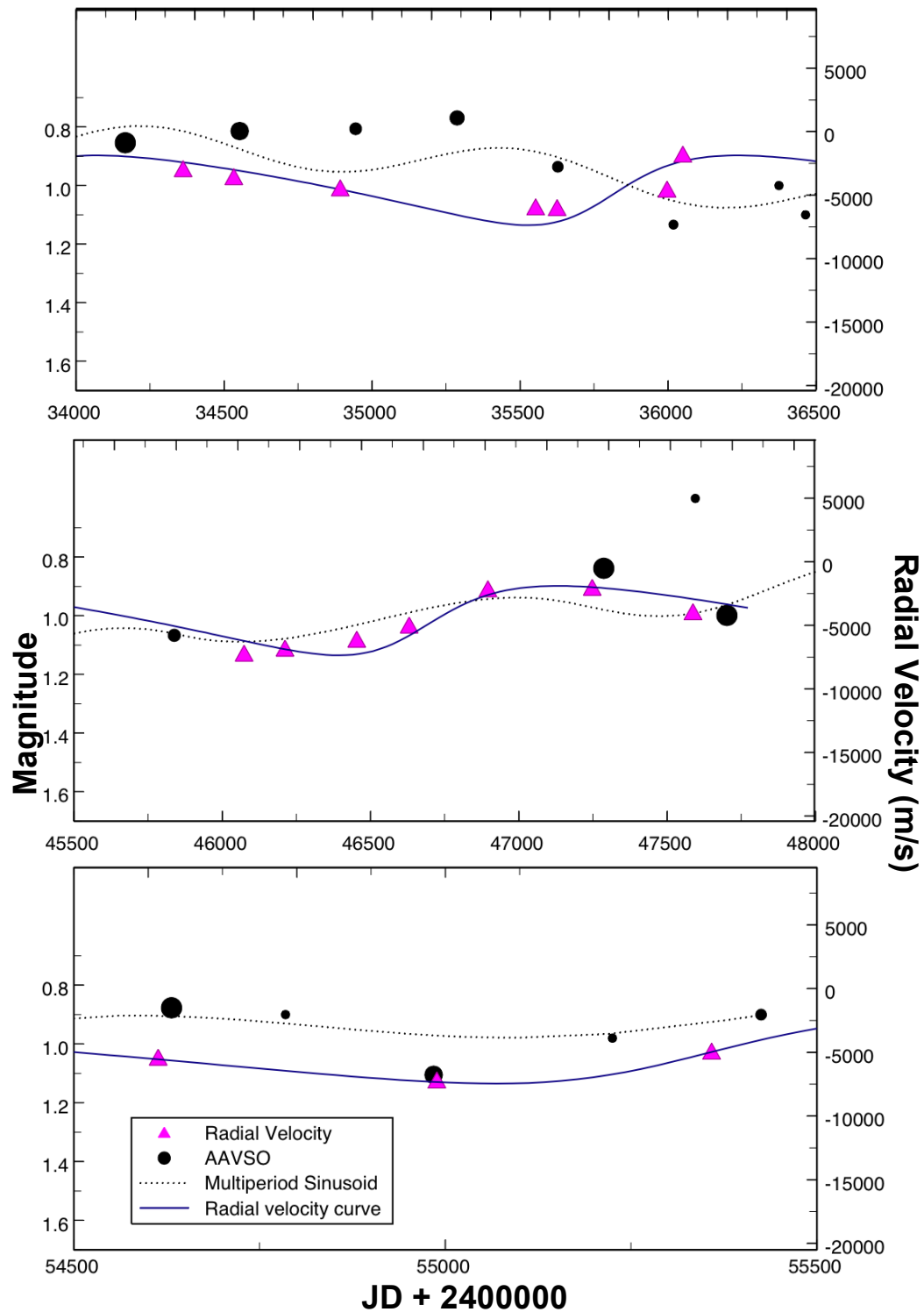


Figure 44: Radial velocity (▲) and AAVSO magnitudes (●) means as a function of Julian Day for three of the four radial velocity data sets. The orbital solution is also shown (blue line) as is the multiperiod sinusoid (black dotted line) calculated from the AAVSO data.

of 160°K with this radius change, we predict a magnitude variation of 0.2. We use the temperature-color calibration of Gray (2005) and $B-V=1.82$ from Lee (1970) to find $T_{\text{eff}} = 3570^\circ\text{K}$, and use the size estimated above.

Although several photometric periods have been reported for Antares none have been found with our 2167-day radial-velocity period. In Figure 44 we compare the season mean radial velocities (from three of the four data sets considered above) to the AAVSO data to see if there is any correlation between the two. We see a radial velocity minimum coinciding with minimum brightness in 2009 (*bottom panel* of Figure 44). In the *central panel* there are too few AAVSO magnitude estimates to determine if there is a correlation between the radial velocity of Smith *et al.* (1989) and the AAVSO photometry. Finally, in the *upper panel* we see anti-correlation between the radial velocities and magnitudes. Figure 44, then, suggests that there is no photometric counter part to the 2167-day spectral variation. While it could be argued that the AAVSO data are too uncertain for us to detect the signal this seems unlikely, since both the 7140-day and the 1260-day variation are smaller than the 0.2 mag variation predicted for this period.

Our radial-velocity curve for Antares is similar to those for long secondary periods seen in $\sim 30\%$ of certain types of semi-regular AGB stars (e.g. Hinkle *et al.* 2002, Nicholls *et al.* 2009), having both the same more rapid rise than fall and an amplitude lying within the $\sim 2\text{-}6$ km/s amplitude range found for these stars. Further, Nicholls *et al.* point out that these variables show no correlation between the velocity and light amplitudes of their long secondary periods. Unfortunately with no long-term high precision photometry this avenue cannot be investigated further here. For now we suggest that the 2167-day variation is likely a long secondary period, the origins of which remain unknown (Nicholls *et al.* 2009).

6.1.4 A 7140-Day Variation

The 7140-day period found from the AAVSO data corresponds to a period of approximately 20 years, such periods are predicted to arise from pulsation only once a

red supergiant has entered the “super-wind” phase (Heger *et al.* 1997). Given that the large light amplitude also expected of such pulsation is not seen, we suspect that this variation does not have a pulsation origin. There are a number of other phenomenon that could explain such a variation in the photometry:

- i. Rotational Modulation – Gray (2001) showed the rotation period for Betelgeuse to be ~ 22 years, not dissimilar to the timescale seen here. A rotation period of 7140-days leads to a rotational velocity of $\sim 6 \pm 1$ km/s, based on the radius given in Table 2. This is a reasonable rotational velocity for a supergiant such as Antares A. Such a modulation could arise from either surface features (such as spots or active longitudes) or from distortions to the sphericity of the stellar surface.
- ii. Time Variable Extinction – Antares A has been found to have a dusty ring of radius ~ 50 AU (Cruzalebes *et al.* 1998; Marsh *et al.* 2001) detected at $12.5 \mu\text{m}$ despite earlier observations (Danchi *et al.* 1992) showing no such feature. This was interpreted as evidence for episodic dust ejection. Such ejection events should correspond with a decrease in observed brightness due to circumstellar extinction. The timescales between such ejection events is expected to be several decades (Massey *et al.* 2005 and references therein) and fits well with the timescales seen in the AAVSO photometry.
- iii. A Magnetic Activity Cycle – Magnetic activity cycles are typically 10s of years (i.e. ≥ 14 years for Arcturus reported by Brown *et al.* (2008)) and so this period is of the correct timescale. Recent detections of longitudinal magnetic fields in other red supergiants (Grunhut *et al.* 2010) mean that such cycles are not unlikely to occur, though Antares A itself had a null detection.

From initial inspection we rule out the starspot hypothesis, for those stars with detected magnetic fields, the longitudinal field-strength is typically less than 1G and Antares A has yet to have a positive detection. Surface fluxes are likely to be very small, while on the other hand convection is very extreme. It seems unlikely that such weak fields could disrupt convective transport in the same manner as they do in less luminous stars. Further, even if there are spots on the stellar surface it seems unlikely that such features

would be as long lived as 20 years. It is this same argument that prevented the suggestion of the modulation of convective cells - again the life-time of any one cell would be so much shorter than this period that the modulation effect would never occur.

Non-sphericity is an attractive option. The surfaces of red supergiants are thought to be asymmetric due to the turbulent conditions and low surface gravity. While the data we have is not sufficient to fully investigate this hypothesis there are number of simple observations we can make. Firstly, the period of 7140-days implies a rotational velocity of 6.1 km/s (as mentioned above), which is not unreasonable for a star like Antares A. Secondly, we look again at Figure 42. The phasing between the four radial velocity data sets is very good and leads to orbit parameters with errors of only a few percent or less. This is despite the large gaps between the observations. The period under examination in that phase plot was 2167 days, approximately 30% of the 7140-day period being discussed here. That is a substantial enough fraction of the cycle that any coincidental changes in radial velocity should distort the shape of the 2167-day radial velocity curve. From Figure 35 we see that during the three epochs of radial velocity observation (JD 2435000, JD 2447000, and JD 2450000) the phase of the 7140-day variation is different. The marked quality of the radial-velocity phasing in Figure 42 suggests that no such gradient exists and that the 7140-day photometric variation has no radial velocity counterpart, or that the radial-velocity change is extremely small. Further, the nature of the variation seen in the AAVSO data, Figure 34, is not truly periodic. This further suggests that non-sphericity cannot explain the changes in the light curve. However, this non-periodic appearance may be a result of the lack of coverage in certain epochs combined with the low precision. Effectively, we can neither confirm nor dismiss the idea of nonsphericity causing changes in brightness on the timescale of several decades.

We find ourselves in a similar position when considering the idea of dimming caused by episodic dust ejection, our data span too small a spectral window and too few years for any of the effects of such an opacity change to be discerned. Whether or not such dust ejection is likely to effect the radial velocity curve can only be determined by accurate knowledge of the physics of the dust formation process, which we do not have. Since mass-loss mechanisms are far from being understood for red supergiants, one is left with

the assumption that such episodic events occur symmetrically whether or not that is the case. Marsh *et al.* (2001) suggested episodic dust ejection events occurred in Antares. They detected two rings containing $10^{-9}M_{\odot}$ of material with radii of 50 AU and 200 AU at $12.5 \mu\text{m}$ and $20 \mu\text{m}$. Based on their measured dust ring radii and the outflow velocity of Bernat (1977), Marsh and collaborators predicted an ejection to have occurred sometime between 1981 and 1991. A photometric minimum in the AAVSO data is observed at around 1982 (JD 2445228). However, the same paper also suggests, based on the two shells observed and Bernat's velocity, that the time between ejection events for Antares is ~ 45 years. So, while the AAVSO minimum coincides with an expected ejection event it also suggests that if ejection events are the cause then a third dust shell should be seen between the two detected by Marsh *et al.* (2001).

6.1.5 The 1260-Day Variation

Table 5: Photometric periods between 1000 and 2000 days (? Indicates that the period is longer than the observational window)

Author	Data	Window Length (yrs)	Periods (days)
Stothers & Leung (1971)	AAVSO	-	1733
Cummings (1998)	Hipparcos & Tycho	2.5	1111?
Kiss <i>et al.</i> (2006)	AAVSO	88	1650 \pm 640
This thesis	AAVSO	64	1260 \pm 400
	AAVSO	2.5	1040?
	Hipparcos	2.5	1055?

In previous photometric studies one finds a number of variations with periods between 1000 and 2000 days, these have been referenced in previous sections and are summarized in Table 5. The difference in window length between the data used here and that used in Kiss *et al.* (2006) arises since we did not include the first seven magnitude estimates as

there is a gap of more than 20 years between these seven points, which cover only 19 days, and the beginning of the remainder of the data.

There is fair agreement between the timescale we determine from the Hipparcos data and that reported by Cummings (1998) and, as was shown in Figure 38, these data are consistent with a longer period also. A study of the AAVSO data from the time of the Hipparcos mission results in a timescale of 1044 days being determined from the Fourier power spectrum. This is very close to that found from the Hipparcos data by ourselves and Cummings (1998) in spite of the observational window being shorter than 900-days in length. There is, however, a large discrepancy between the timescale we see in the AAVSO photometry and those found by previous authors. To investigate the origins of this discrepancy the AAVSO data were reexamined using the data points from within the observational windows corresponding to those of the previous authors.

Analysis of the same span of data as Kiss *et al.* (2006) resulted in a peak at 1268 ± 5 days. This is essentially the same as the period that found by our original analysis of the data. To investigate the cause of this difference further we also analyzed the data of α Her A over the same window as Kiss *et al.*, in that case we found the same periods as reported by those authors. Further we analyzed the data files of Kiss *et al.* (provided by private communication) and found a difference between the initial data used by those authors and in this investigation. The files provided by Dr. Kiss, while covering the same observational window as our data contained one-third the number of data points. With this differences accounted for we are able to reproduce the Kiss *et al.* result. Further discussion revealed that the *missing* data were excluded as a result of the automated data selection program used by Kiss *et al.* and was likely an oversight. Thus, the differences between the data used here and that analyzed by Kiss *et al.* are arbitrary and we conclude that the result presented here is the more correct result.

Stothers & Leung (1971) did not include a date span or observation window with their period estimates. Instead of performing the analysis over the same window as them, we instead performed the analysis on all data observed prior to 1970 (JD 2440587). From this data we find a peak in the amplitude/power corresponding to ~ 1780 days.

From the comparison of the periods given in Table 5 and the discussion above we see that the timescale associated with the variation seen in the photometry of Antares within the range of 1000 to 2000 days is unstable. These changes in the timescale of variability were further investigated by comparing the amplitude/power spectra of various windows of the AAVSO data. Figure 45 shows various spikes that correspond to frequency peaks from the different observational windows used. These peaks can be enclosed by a dispersion function with a FWHM of 420 days, this dispersion function also encloses the frequencies reported by various investigators. For completion, Figure 45 also shows the dispersion profile for the period and FWHM reported by Kiss *et al.* (2006).

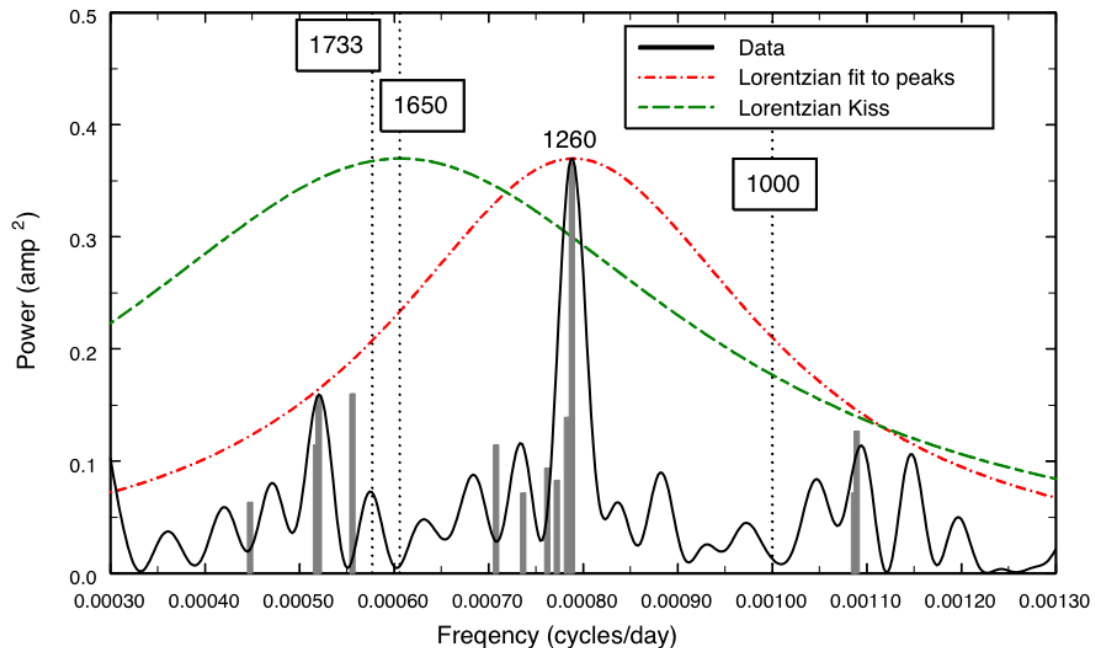


Figure 45: Fourier power spectrum of the AAVSO photometry, prewhitened and focused on the 1260-day peak. *Solid black-line* – prewhitened data. *Dot-Dash red-line* – Lorentzian fit to the frequency peaks. *Grey spikes* – Frequency peaks from various observational windows. *Dashed green-line* – Lorentzian from Kiss *et al.* (2006). *Dotted black-lines* – previous periods found in the literature (periods given in days).

Such structure in the Fourier amplitude spectrum is typical of convection driven oscillations, as was discussed in Chapter 3. Previous interpretations of this 1000 to 2000 day variation have determined that it arises from giant convection cells, due to number of different periods found within this range (Stothers 2010 for example). Figure 45 suggests that such an interpretation could well be correct. It is curious then that no corresponding timescale is found in the radial velocities or line-depth ratios. Previous authors often considered this 1000-2000 day period as having the same origin as the long-term radial velocity variation. In light of the remarkable phase coherence of the radial velocity seen in Figure 42, it seems unlikely that it shares its origin with this 1000-2000 day photometric variation. Further, Figure 44 demonstrated no systematic similarity between radial velocity and photometric changes during the three epochs of radial velocity observation. This makes a physical interpretation of this timescale extremely difficult. We observe a stochastically driven, damped variation in the brightness, accompanied by no radial velocity variation.

6.1.6 100-200 Day Variations

As was noted earlier, short-term variations are seen along with all of the variations already discussed. We observe a variation of ~ 100 days in both the line-depth ratios and radial velocities, as well as seeing an approximately 200-day variation in the Hipparcos photometry. Before consideration of the various timescales reported and the possible mechanism for this variation we examine our data more thoroughly. To this end we compute radial velocity residuals compared to the 2167-day orbit solution (Figure 43) for each of our radial velocity measures. The resulting residual velocity curves are shown in Figure 46 along with three sinusoids each with a 100-day period. Periods of approximately this length have been found by various previous authors. Table 6 reviews the available timescales. No timescales shorter than the, approximately, 1 year discrepant timescale have been recorded, that we could find, for the AAVSO photometry. There is evidence of short-term variations in early radial velocity studies (Lunt 1916 for example), however, this was in general attributed to noise and ignored.

Table 6: Photometric periods between 100 and 200 days

Author	Data	Period (days)
Smith <i>et al.</i> (1989)	Radial Velocity	260 ± 20
Cummings (1998)	Hipparcos & Tycho	215 and 95
This thesis	Radial Velocity	100 ± 6
	Hipparcos	170

The picture one gets from Table 6 is chaotic, there are various timescales of variability. In Figure 46 we see that in spite of the successful fit of a 100-day sinusoid to the three seasons of radial velocity data, the phase and amplitude change from one season to the next. From 2008 to 2009 there is a phase change of 4 days. From 2009 to 2010 there is a phase change of 46 days, or approximately half a cycle!

The 260-day timescale attributed by Smith *et al.* (1989) stems from periodogram analysis and the resulting sinusoid fit to the data is quite poor (Fig 8. of that paper). In lieu of our findings (Figure 46) we reexamine the data of Smith *et al.* (1989) in Figure 47. Similar to our data 100-day sinusoids characterize the variations. We see large changes in phase and amplitude, again this is similar to the results from our data in Figure 46. Several of the plotted sinusoids characterize the measured radial velocities very well within errors. In those cases we can determine the phase and amplitude variations. The amplitudes vary from 800 m/s to 2400 m/s and we determine phase changes as large as 60 days. We find that the data cannot be modeled with a 260-day sinusoid and conclude that the 260-day period (Smith *et al.* 1989) is not physically significant. The Fourier amplitude spectrum of the residuals, shown in Figure 48, is similar to those usually associated with granulation and convection, in that it has multiple lower amplitude peaks. While these peaks may arise in a similar manner, they are also similar in length to the coverage and gaps of the data. In Figure 48 we have fit Lorentzian and Gaussian curves to the peaks. The largest of these peaks correspond to the period determined by Smith *et al.*, though the Gaussian and Lorentzian are centered at 200-days. We conclude however that

Fourier amplitude analysis is unsuitable for variations such as that seen here. The amplitude and phase changes occur over timescales not much larger than 100 days thus it is easy for Fourier amplitude peaks to arise erroneously.

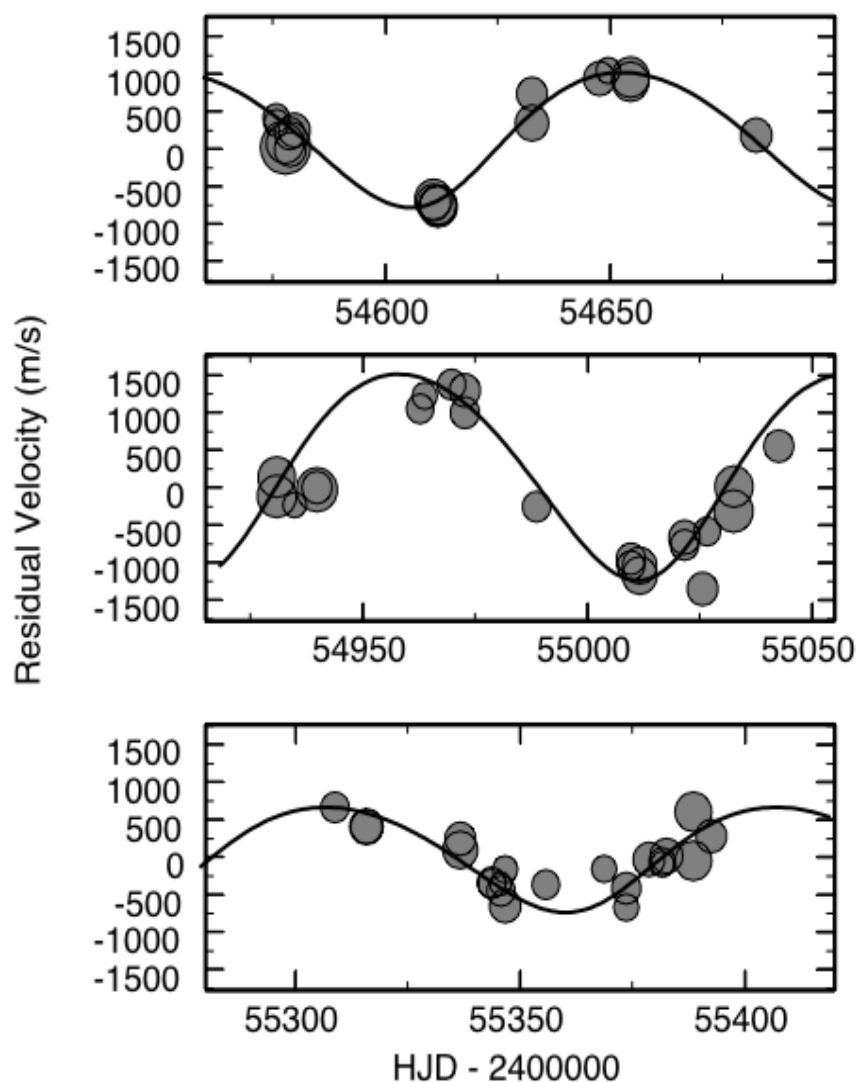


Figure 46: Radial velocity residuals as a function of Julian Day. The plots are in chronological order from 2008-2010. Each panel encompasses 140 days. Symbol size indicates points weight from photon count. The solid line plots a sinusoid with a period of 100-days, the same period sinusoid is used in all three panels with the phase and amplitude being altered.

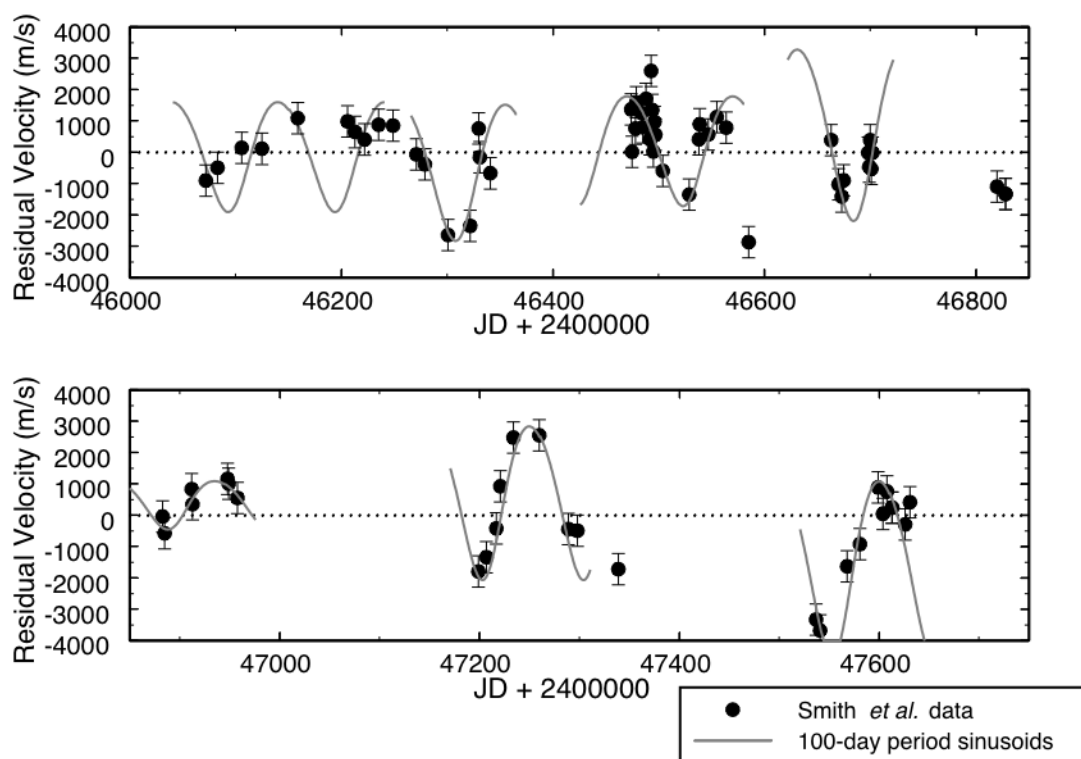


Figure 47: Residuals of the Smith *et al.* (1989) are shown by the *black points*. The *grey curves* are 100-day sinusoids with differing phases and amplitudes: these show that the 100-day characteristic timescale has persisted for at least several decades. The error bars show the typically error quoted by Smith *et al.* (1989), ± 500 m/s.

These behaviors; phase shifts, amplitude variations, and multiple frequency peaks, are typical of a chaotic phenomenon. Large convection cells are expected to cause such variations since their location will be random, while the size and velocity are dictated by the stellar structure. Similarly, spots that originate from active longitudes could also cause such variability since spot sizes and numbers are stochastic but their location of origin will be consistent. The second scenario seems unlikely since Antares has no detectable magnetic field (Granhut *et al.* 2010) and we see no evidence of spotting in the shapes of the spectral lines. Further information can be garnered by comparing the

variations of each measurement, since Antares shows variation in radial velocity, brightness and temperature.

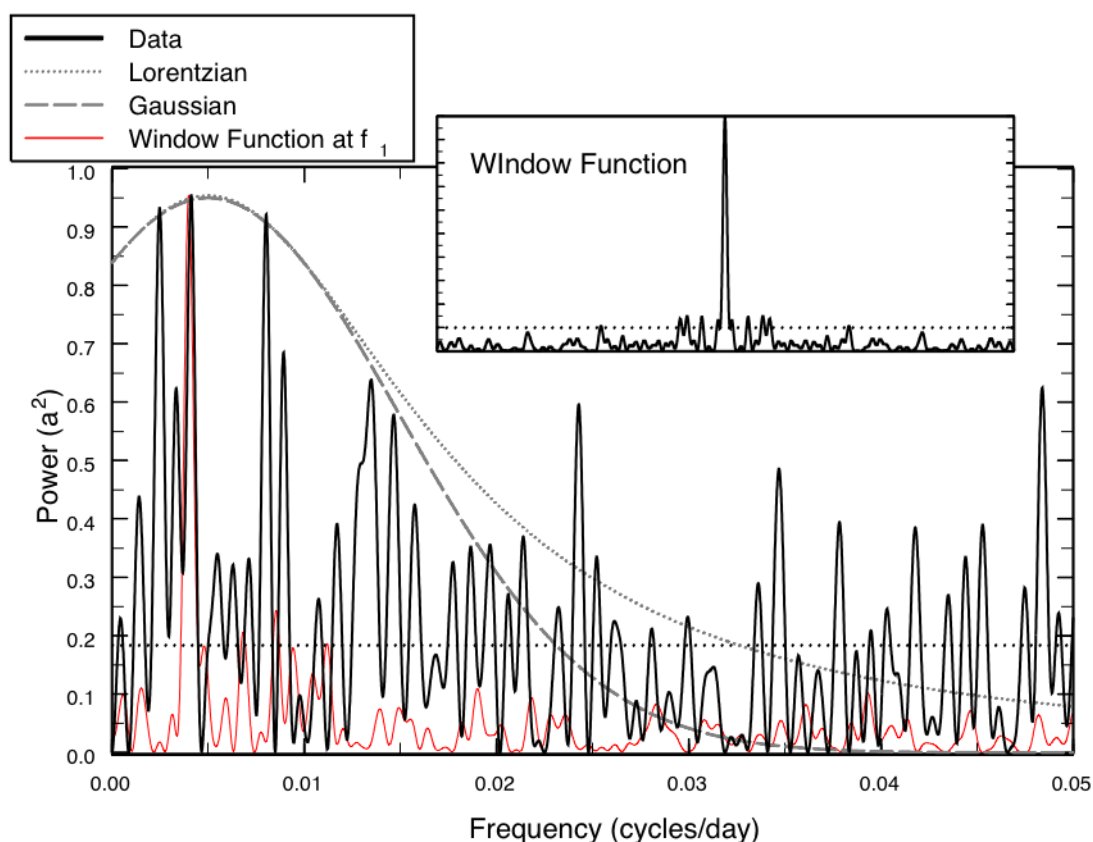


Figure 48: Fourier power spectrum of the radial velocity residuals from the data of Smith *et al.* (1989). The main peak occurs at 260 days and is flanked by several smaller peaks. A Gaussian (*dashed*) and Lorentzian (*dotted*) curve are fit to the peaks. The inset panel shows the window function, while the red-line shows the window function scaled and fit to the amplitude peak. The Gaussian and Lorentzian curves are centered at 200 days.

With no concurrent spectral and high precision photometric data we cannot tell by direct comparison if the short-term variations in brightness are due to the short-term variations in temperature. A comparison of our line-depth ratios and the AAVSO photometry can be made and is shown in Figure 49. There are occasional hints of similarity, however

there is enormous scatter amongst the measures that are contained within each binned AAVSO point. The typical standard deviation of any one magnitude point is shown by the single error bar. We see here that the variation likely to arise from the temperature changes is, in general, smaller than the scatter of the magnitude estimates. Thus, a direct comparison of this manner is neither informative nor useful. We instead make a comparison between the scales of the line-depth ratio variability and the scales of variability seen in the Hipparcos photometry.

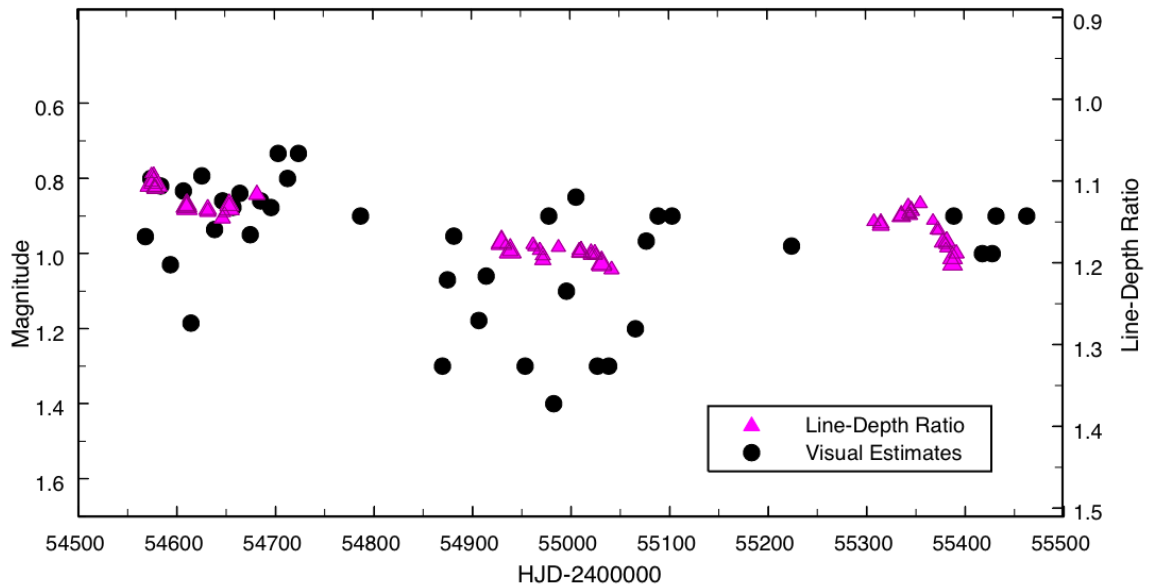


Figure 49: AAVSO binned magnitude estimates (●) and line-depth ratios (▲) as a function of Julian Day. The line-depth ratio axis has been scaled such that the typical amplitude of the variation is equivalent to an amplitude of 0.12 mag. The typical standard deviation in the AAVSO points is 0.165 mag.

In Figure 50 we compare the temporal variation in line-depth ratio with the temporal variation in the Hipparcos magnitudes. The line-depth ratios have been scaled such that the equivalent change in brightness is ~ 0.12 mag. This change is found from atmospheric models constructed using a mean temperature of 3570°K (as determined previously from B-V) and a typical variation in temperature of $\pm 31^\circ\text{K}$, found from the typical variation in

line-depth ratio. These models use $\log g = 0$ and $\log(Fe/H) = 0.05$, the typical values for a star of this type. From the Hipparcos magnitudes we measure a typical variation of 0.13 mag for the short-term variability. The predicted change in brightness from our line-depth ratios falls very close to this value suggesting that the two features have a similar origin. While these numbers are typical we find temperature variations of between 33°K and 80°K , thus we should expect the brightness variations to be similarly chaotic.

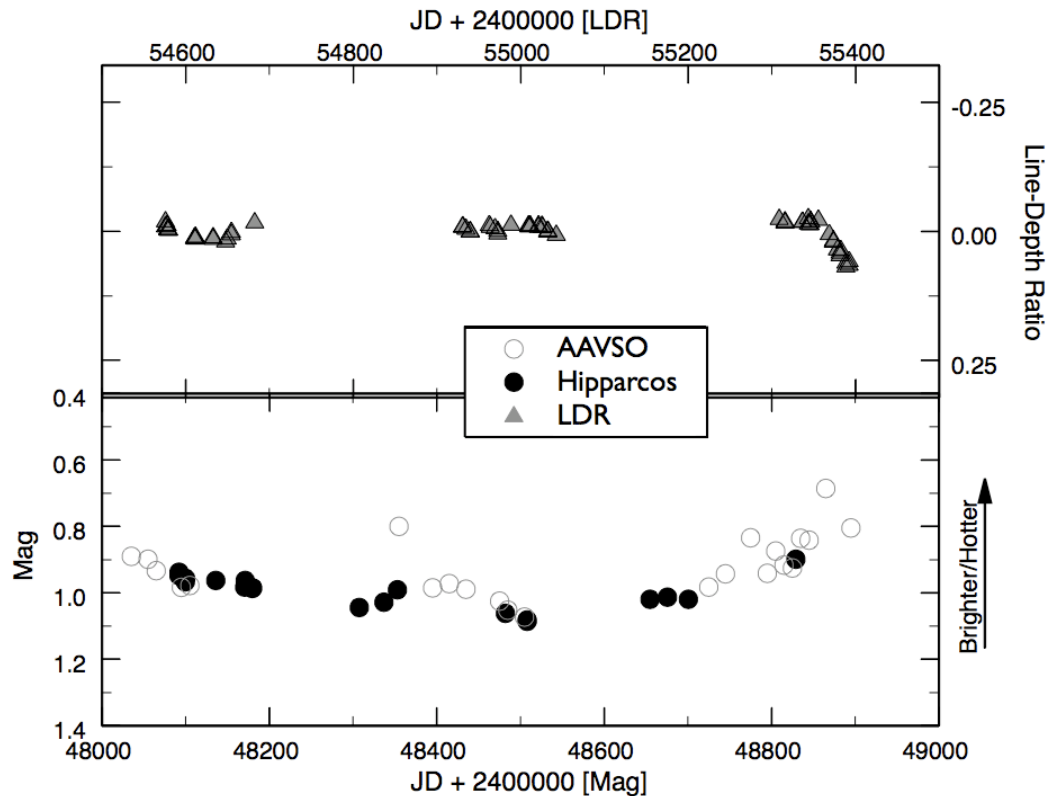


Figure 50: *Top* – Line-depth ratios measured from 2008 - 2010. *Bottom* - Hipparcos magnitudes from 1989-1991 (●) and AAVSO magnitudes over the same epoch (○). Both panels cover 1000 days and the line-depth ratios are scaled to correspond to a 0.12 mag brightness amplitude, as expected from the temperature variation.

One further investigation is possible using the measurements presented and discussed thus far: following the procedure of Gray (2008), we plot the residual line-depth ratio against the residual radial-velocity and compare the data for the three seasons

individually. The residual line-depth ratio versus residual radial-velocity plot is shown in Figure 51. Antares A shows similar behavior to that found in the case of Betelgeuse (Figure 7 & Gray 2008), though the cycles are not so clearly defined. And based on integration of the radial velocity sinusoids we find a typical rise height that is an order of magnitude smaller than Gray (2008) reported for Betelgeuse.

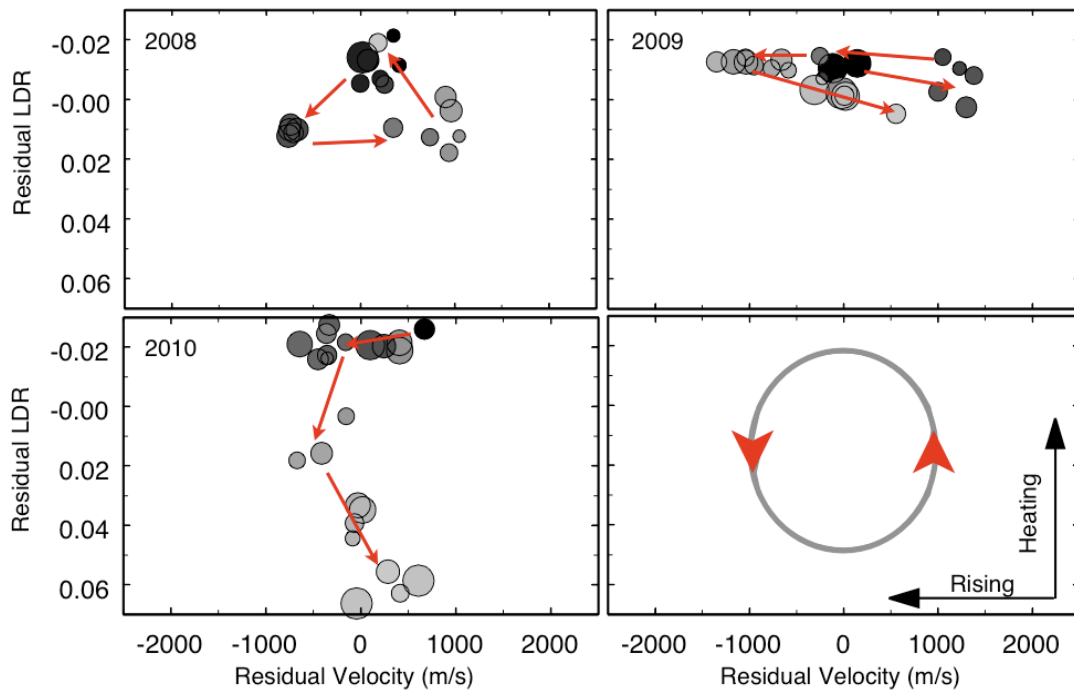


Figure 51: Line-depth ratio residuals as a function of radial velocity residuals for individual seasons. Point size indicates exposure signal-to-noise. Dark points are for data observed early in a season and light points for the data taken later in a season. The final panel (bottom-right) indicates a simplified picture of convective cycling and shows the orientation of the physical parameters. A 0.02 change in LDR corresponds to $\sim 18^{\circ}\text{K}$ change in temperature.

The behaviors seen in the preceding section make a very strong case for the 100-200 day variations stemming from large convection cells on the stellar surface. We see a characteristic rise of hot material and fall of cool material (Figure 51), though the true nature of the dynamics are much more complicated than this. We have seen that the

change in temperature can effectively explain the observed changes in brightness, though no simultaneous measures are available. We have seen a characteristic multi-peaked Fourier power spectrum, typical of stochastically driven oscillations. And we have seen how, within the Elginfield data and within the data of Smith *et al.* (1989), a single period which undergoes a phase and amplitude change can characterise the data (Figures 46 and 47). Combined these results make a convincing case for giant convection cells. Which, in light of the null magnetic field measurement (Grunhut *et al.* 2010), seems the most plausible explanation.

6.1.7 Summary

In this section we have measured and characterized several timescales of variation for Antares A:

- i. A period 7140 ± 10 days is found from >60 years of AAVSO visual estimates. Such a variation may arise from rotational modulation of a nonspherical surface or episodic dust ejection
- ii. A period of 2167 ± 5 days is found from a combination of four radial velocity studies. Lack of a known photometric counterpart and the shape of the radial velocity curve suggest that this is a long secondary period or the type seen in many red giant semiregular variables.
- iii. A characteristic timescale of variability of 1260 ± 400 days is found from a combination of AAVSO visual estimates and Hipparcos photometry. This is in keeping with previous studies and along with those shows evidence of a timescale that varies. This is similar to other semiregular variables and characteristic of a stochastic driving mechanism.
- iv. 100 ± 6 day period sinusoids are able to successfully characterise radial velocity variations. The amplitude and phase of these variations changes rapidly. We

interpret these variations as convective cells perturbing, or erupting through, the photosphere.

- v. Note: the 350 day variation recorded by Percy *et al.* (1996) is not reproduced here, since we did not examine the photoelectric data. If this is, as those others and studies of other red supergiants and semiregular variables suggest, the primary radial period then $P_2/P_1=6$, this is large but not unreasonable (Wood *et al.* 2004).

Thus we see a highly complicated picture with variations occurring on 5 different timescales.

6.2 The Depth Dependent Velocity and the Third Signature of Antares A

In the previous section we discussed the mean radial velocity variations. That is we computed the radial velocity by taking a mean for each spectrum using 18 lines of various depths. To determine this mean we measured the radial velocity for each of these 18 lines individually for each spectrum. This allowed us the opportunity to also observe how the variations (2167-day and ~ 100 -day) change as a function of line strength. This was done in two fashions, the details of which will follow. Our initial reasoning stems from our inability to compute bisectors for this star. Since we could not map the changes in the photospheric velocity distribution by observing changes in bisector shapes, we instead looked to changes in the third signature shape.

6.2.1 The Line-Strength Dependence of the Radial Velocity Curve

We examined the radial velocity means taken from lines of similar strengths. Grouping the lines by strength in this manner, we computed four means per spectrum. Similar to the analysis carried out for the average radial-velocity above, we examine both the long-

term (2167-days) and short-term (~ 100 -days) variations. In particular the short-term variations are examined by taking the residuals compared to long-term variation.

A sample residual radial velocity curve for 2009, computed from the three strongest lines, is shown in the *right-hand* panel of Figure 52. In Figure 52 we compare the mean residual velocity (*left*) with the residual velocity of the strong lines (*right*). The amplitude of the variation is approximately 800 m/s lower in the strong lines than in the mean. As was discussed earlier the typical errors are 100 m/s in both cases.

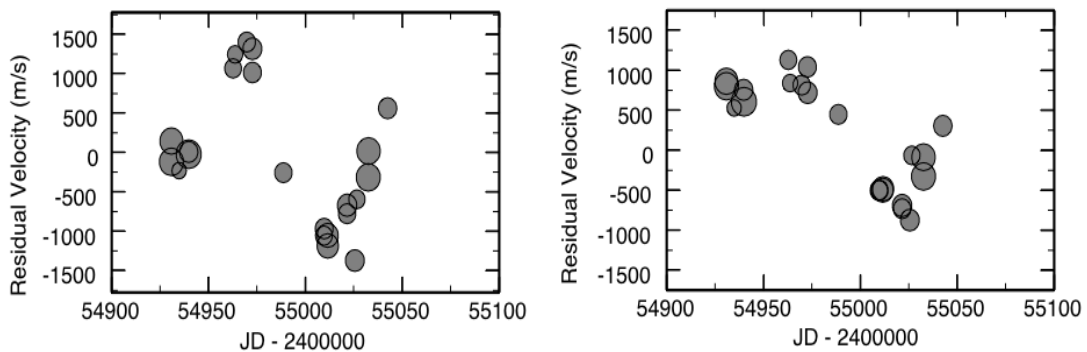


Figure 52: *Left* - Mean residual velocities from 2009 as a function of Julian Day. *Right* – Mean residual velocities from the three strongest lines in the spectrum of Antares. Amplitude of the variation is decreased by ~ 800 m/s compared to the mean distribution and has a slightly different shape.

6.2.2 The Season Mean Third Signature Plot

The third-signature of granulation plots individual line core-fluxes as a function of their radial velocity. In the Sun and a handful of other stars, we see a signature of convective overshoot in such plots (above and Gray 2009), where weak lines, which are formed deeper in the photosphere, demonstrate the greatest rise velocities. From the variations seen in Figure 52, we anticipate seeing changes in the shape of the third-signature. In Figure 53 we show the season mean third-signatures. These were each constructed from approximately 20 exposures and have a signal-to-noise of >2500 . The typical error on

any one point is 90-200 m/s. We also show the mean third-signature averaged for lines of similar strength with their statistical errors. These two plots indicate that the variation in shape is statistically significant and that we are witnessing a dramatic change in the dynamics of the photosphere.

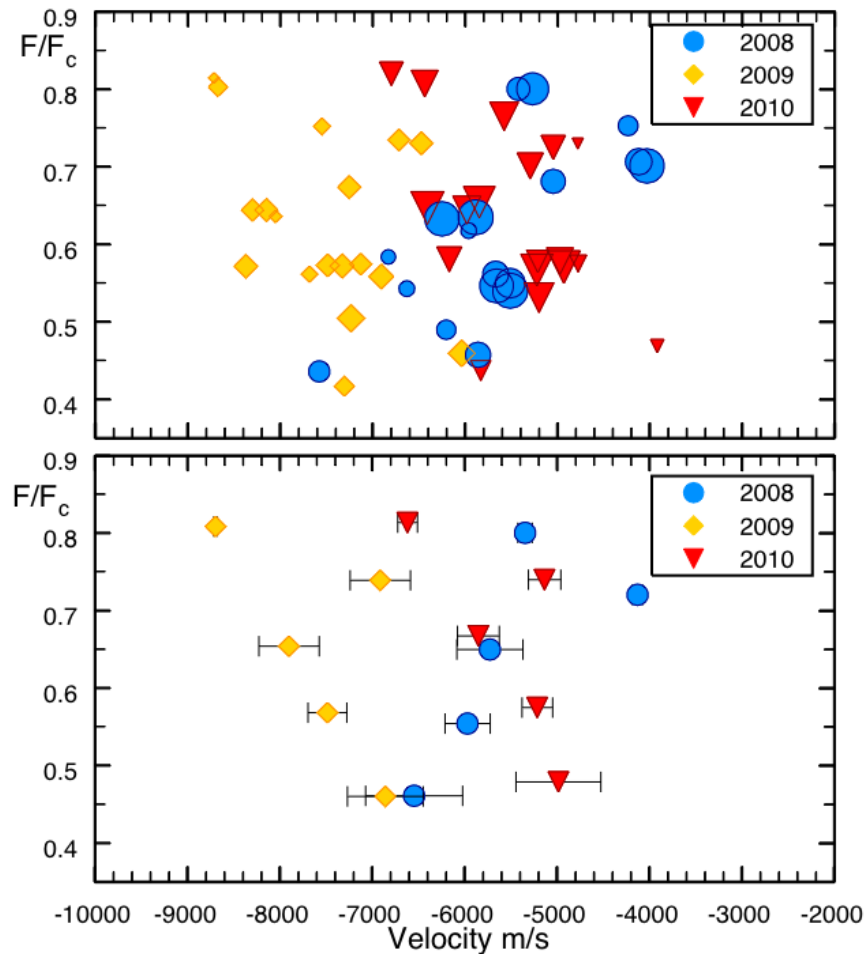


Figure 53: *Top* - Season mean third-signatures. Blue circles for 2008, orange diamond for 2009 and inverted red triangles for 2010. Typical errors range from 90 m/s to 200 m/s for each point, symbol sizes represent this error - smaller symbols for larger errors. *Bottom* - Mean third signature constructed by averaging the core position of lines with similar strengths. Error bars give the statistical error in the mean of each point; the three points with no obvious error bars have errors that are smaller than the symbol size.

We observe a dramatic change in shape from 2008 to 2009 where the third-signature returns to an almost solar-like shape (compare to Figure 25). If the interpretation of the third-signature is correct, where we assume that the weak lines are formed deeper in the photosphere than the strong lines, then we are observing a very dramatic change in the photospheric velocity gradient from 2008 to 2009. As mentioned above there are two physical phenomena that could result in such a variation: differential expansion of a pulsating atmosphere or the penetration of the photosphere by giant convective elements.

The bottom panel of Figure 53 shows quite distinctly that the shape change of the third signature plot is not correlated with the radial velocity, else 2008 and 2010 would have similar shapes. (For the following discussion I refer the reader back to Figures 40 and 43). Though we have not measured the pulsation velocity or the pulsation acceleration for the 2167-day variation, the shape of the radial velocity curve can tell us something about these parameters. From 2008 to 2009 the radial velocity curve is falling, the atmosphere is approaching the maximum speed of approach. Shortly before 2008 the radial velocity passed through its mean value (V_0) and in 2009 the maximum speed of approach (minimum radial velocity) was reached. Thus, we can conclude (somewhat simplistically) that from 2008 to 2009 the atmosphere was accelerating outward at a decreasing rate. During 2009 the direction of the acceleration changed and the velocity begins to move back toward the mean value. From 2009 - 2010 we see the opposite occur, the radial velocity is increasing (i.e. the velocity is dropping from maximum velocity of approach) and the acceleration is now directed inward. So, while the shape change is certainly not dependent upon the value of the radial velocity, it does seem to be dependent upon the nature of the radial acceleration.

6.2.3 The Residual Third Signature Plot

Less pronounced changes in the shapes of the third signature plots are seen within each season. Due to the large scatter typical in the third signature plots of high luminosity stars (Gray 2010; Gray & Pugh 2012) these variations are more readily observed from the residual core positions than the measured core positions. In Figure 54 we present both

the full residual third signatures and those constructed by averaging the core positions of lines of similar strength. We constructed four third-signature plots per season. Using the means of at least two exposures we were able to maintain a combined signal-to-noise ratio of more than 500. The season mean third-signatures shown in the top panel of Figure 53 were then subtracted from each, resulting in four residual third-signatures per season, seen in the top three panels of Figure 54. For each of these, we then computed a weighted average of all core positions within each $0.1 F/F_c$. These are shown in the bottom three panels of Figure 54, we also show the typical error in the radial-velocity position of the points in the top panels ($\sim 150\text{m/s}$), these indicate that the overall mean-shape changes are larger than the error in any one point. Typically we see larger shape changes for larger mean radial-velocity shifts and the incline of the residual third-signature coinciding with the radial velocity. The shape change here is less definite than that seen in Figure 53, likely due to it stemming from a different physical effect, but still it seems a very real phenomenon. Similar to the shape changes discussed in the previous section there are a number of ways in which shape changes such as these can arise.

These changes are independent of the long term shape changes. We come to this conclusion since despite dramatic changes in the radial velocity during 2009, and consequently large changes in atmospheric acceleration, the scale of the shape change is much smaller than the shape change between the mean of this season (2009) and the mean of the previous season (2008). The maximum relative position change (that is weak line position relative to the strong line position) from 2008 to 2009 is $\sim 3000\text{ m/s}$. While the maximum change in relative position seen in 2009 is $\sim 1800\text{ m/s}$. This is despite the fact that the radial velocity amplitude of 2009 is almost twice as large as the change from 2008 - 2009 and is occurring over a much shorter time, thus massively increasing the radial acceleration.

From Figure 54, we see that there is effectively no change in shape during 2010, while in 2008 and 2009 there is a change in the slope of the residuals (and thus the slope of the third signatures) that is correlated with the radial velocity. This excludes the weakest lines, which are the most difficult to measure and the most affected by blending changes. Since these changes scale with radial velocity, are independent of the pulsation discussed

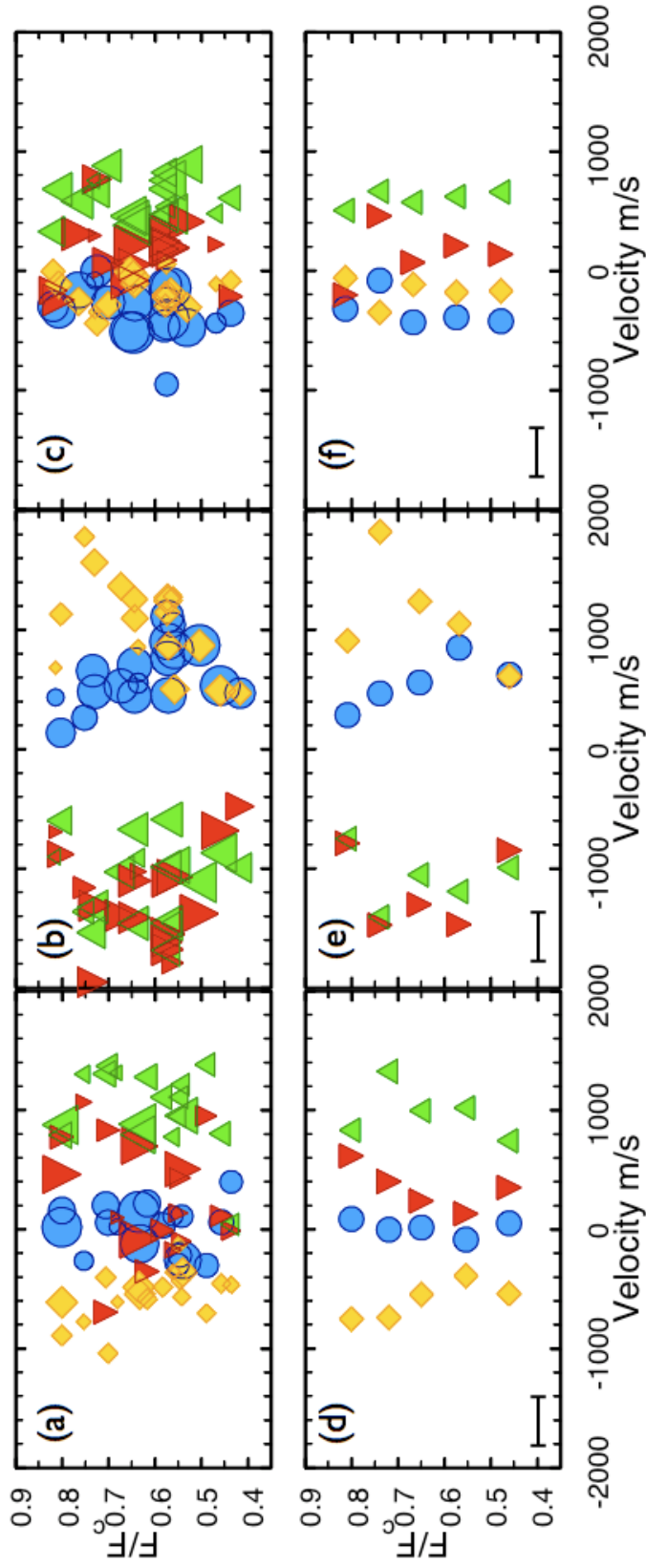


Figure 54: *Top* - Residual third-signature plots: (a) 2008, (b) 2009, (c) 2010.

Bottom - Depth averaged residual third signature plots: (d) 2008, (e) 2009, (f) 2010.

The different colors are for the four different data groups and represent a time progression through the season. In each season the color progression is the same. First group - *blue circles*. Second - *orange diamonds*. Third - *red inverted triangles*. Final - *green triangles*. In (d), (e), and (f) we show the typical error bar of a point in (a), (b), and (c).

in the previous section, and occur on the timescale of months we conclude that they are caused by the same convective cells that cause the ~ 100 -day variations seen in the temperature and radial velocity. In the case of short-term changes in the shape of the third signature, the effect arises due to convective overshoot. The convective elements do not penetrate the entirety of the photosphere and their velocity diminishes as they climb in altitude or inversely increases as they fall back through the atmosphere. Thus, they affect the weakest lines most strongly while the strong lines are affected very little, if at all. Because the cells are so large, unlike the *normal* solar-like case, we not only see the effect of the rising material but also of the falling material as the cell recedes since at any one time we are observing only one cell rather than the combined light from many cells. So, when the cell is receding from us, there is no rising material to affect the measured radial velocities.

6.2.4 Summary

Antares A displays variability in its photospheric velocity distribution (third signature). At times the inner photosphere has a larger rise velocity than the outer atmosphere and at other times the inner photosphere has smaller rise velocities (or larger fall velocities) than the outer regions. Interpretation without further stellar examples of this phenomenon is difficult. For now however, our interpretation is two fold and essentially follows our interpretation of the radial velocity variations. That is: long-term variation is attributed to differential expansion and short-term variation is attributed to convective motions.

6.3 Line Shapes

In Gray (2008) the line shapes of Betelgeuse were analyzed using the FWHM and bisectors of the 6261\AA Ti I line. This line is distant enough from other spectral lines that it suffers less from blending than other lines in the spectrum. However, Antares A is a southern star with a declination of -26° . With this low a declination this star is only observable from the Elginfield observatory for an hour or two as the star passes the

meridian. In addition, its low position in the sky results in the light passing through a large volume of the atmosphere. Thus, we detect atmospheric telluric lines in our spectrum. In Figure 55 we show a sample of spectra at wavelengths longer than 6259\AA . In this region we see dramatic line shape changes introduced by the atmospheric lines. In Figure 55 the baricenter corrections are subtracted from the data to highlight that the atmospheric lines are approximately stationary compared to the stellar spectra. Since these telluric lines change the shape of the 6261\AA line bisectors of this line were not used to study the shape changes instead we simply overlay other spectral lines.

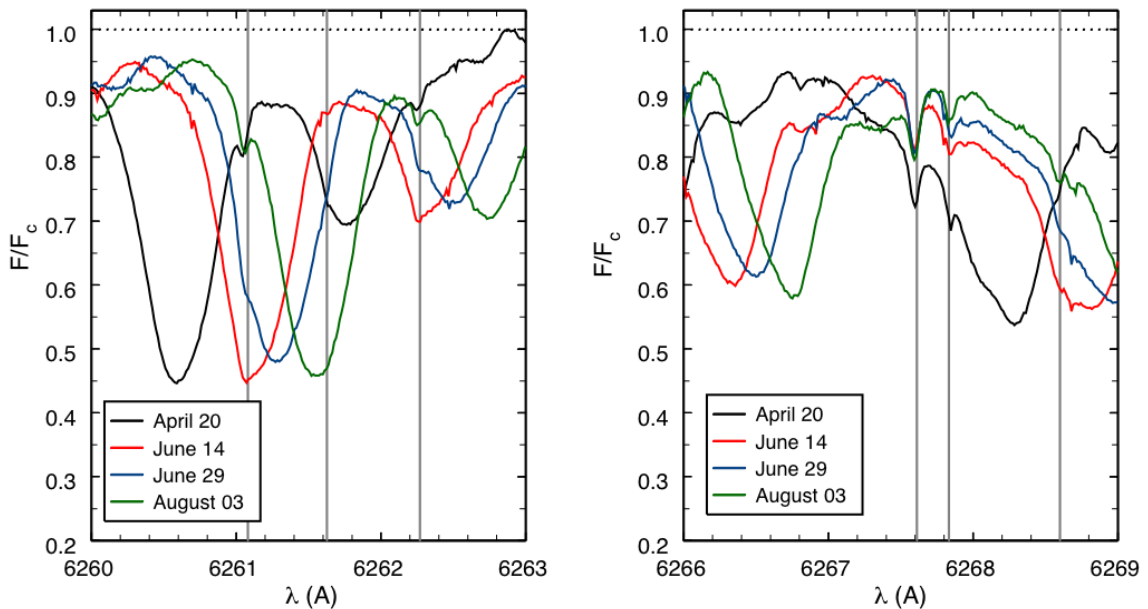


Figure 55: Telluric lines seen in the spectrum of Antares, the baricenter corrections have been subtracted from the data. We see that the atmospheric lines are approximately stationary compared to the stellar spectrum. *Grey lines* show the λ_0 positions of the spectral lines.

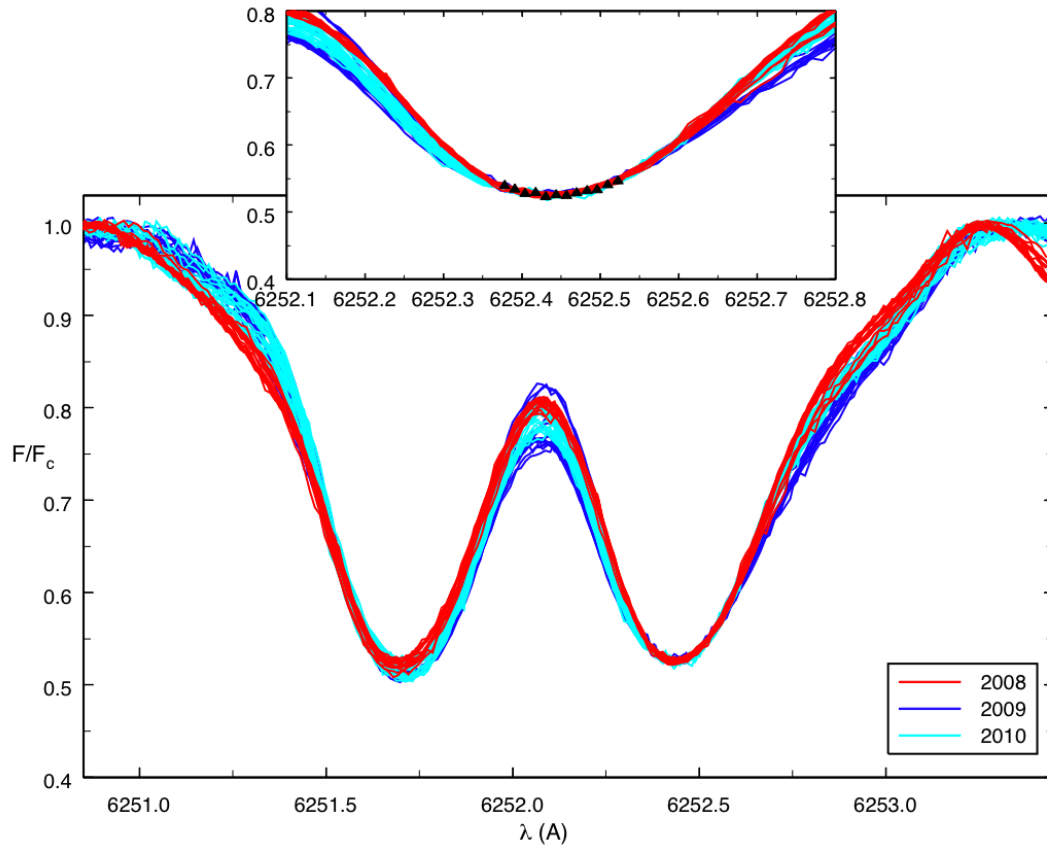


Figure 56: Spectral lines shifted to negate the radial velocity shifts and scaled to ensure that the 6253 Å line is the same depth in all lines. The red lines are for 2008, the blue lines are for 2009 and the teal lines are for 2010. Note the larger spread in core depths of the 6252 Å line compared to that of the 6253 Å line due to the temperature variations. There is a small difference in the position of the 6252 Å line cores relative to the 6253 Å, we attribute this to changes in the photospheric velocity gradient (see section 6.2.2). The inset panel shows the core of the 6253 Å line

Figure 56 shows the 65 spectra shifted to account for radial-velocity changes and scaled to the same depth and continuum. Upon initial inspection we note:

- i. The 6252Å vanadium line shows much more depth variation than the 6253Å iron line. This is a result of their differing temperature sensitivities. (The iron line is more temperature stable than the vanadium line).
- ii. The position of the 6252Å vanadium-line core changes relative to the 6253Å iron-line core. We attribute this change to changes in the photospheric velocity gradient, as discussed in the previous section. The line forming region of these two lines is not identical, in spite of their similar line strengths. These small differences are seen in Figures 53 and 54, which is why averages rather than individual positions were used in that analysis.
- iii. The blending region between the two lines varies much more than the depths of either line and is thus interpreted as arising from changes in the other broadening mechanisms, rather than changes in temperature (further discussion to follow).
- iv. The spectra of 2008 have both narrower line cores and narrower peaks, which we attribute to lower turbulent velocities (further discussion to follow). This is most evident from the 6253Å line and the *continuum* peak following that line.
- v. The core position of the 6253Å line is unaffected by the observed changes in the profiles. Section 5.3 noted that, typically 12-20 spectral line points were used in order to fit line core positions. In the inset panel of Figure 56 the twelve core points of the 2010 6253Å lines occur before the deviation of the blueward section. Thus, within our minimum 12-point limit we see that the radial velocity does not change despite changes in line width (and depth - discussed in the next section).

Before discussing the changes in broadening one should look also at the changes in line depth since an increased line width (due to increased broadening) should be associated with a corresponding reduced line depth. We compare the depths of lines from each of the seasons of observation in Figure 57. Changes in the line depths are observed despite relatively small changes in temperature; the depths of all lines change dramatically, while the changes in line-depth ratio are small by comparison. Compare for example the depth changes between 2008 and 2010 (Figure 57) despite the small differences in temperature between the two seasons (Figure 41). As such the changes in depth can not be accounted for by changes in temperature alone.

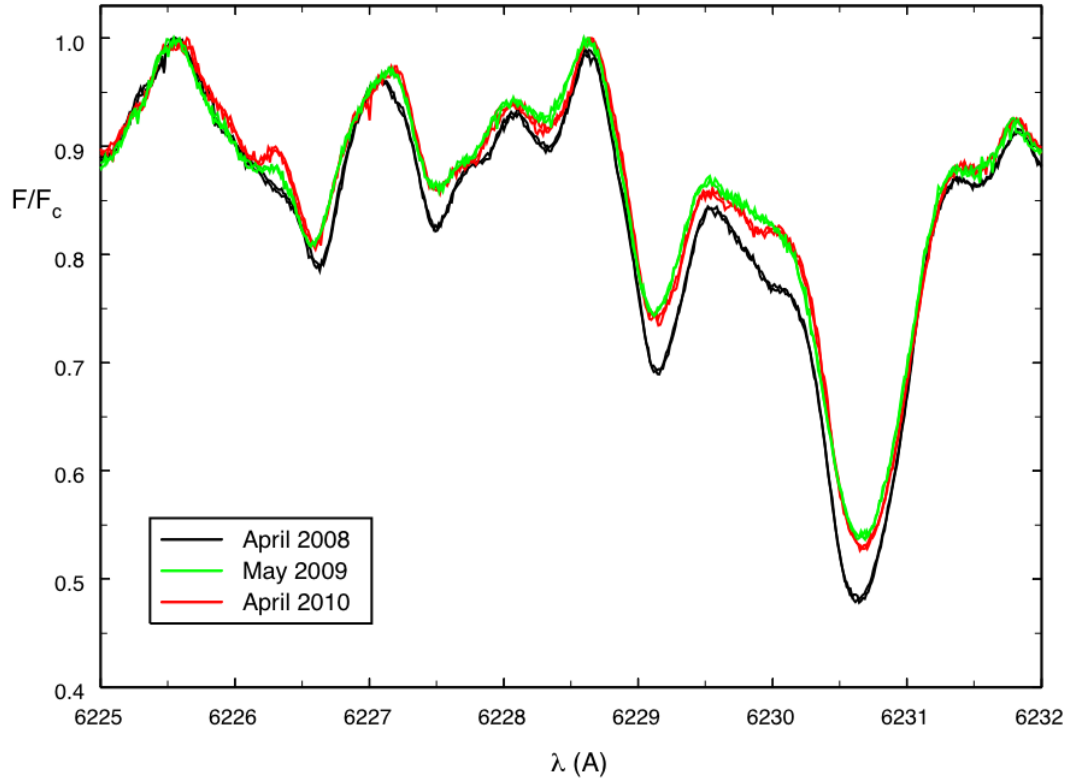


Figure 57: A 7Å window showing two spectra from 2008, 2009, and 2010. We note not only changes in the spectral line depths but also in the sharpness of the features – note the *blurring* of spectral features in the blending region between the 6229Å line and the 6231Åline.

In order to analyze the line broadening we compare the changes in line depth and line width, the changes in temperature and the changes in the sharpness of spectral features. From Figures 56, 57 and 58 we see that as the lines become shallower (2009 and 2010) they also become broader. The broadening is seen most prominently in the steepest parts of the 6253Å line in Figure 56. Such variation indicates changes in the spectral line broadening and thus changes to the turbulent velocity field. Since our normalization technique raises the entire spectrum, blending peaks as well as core

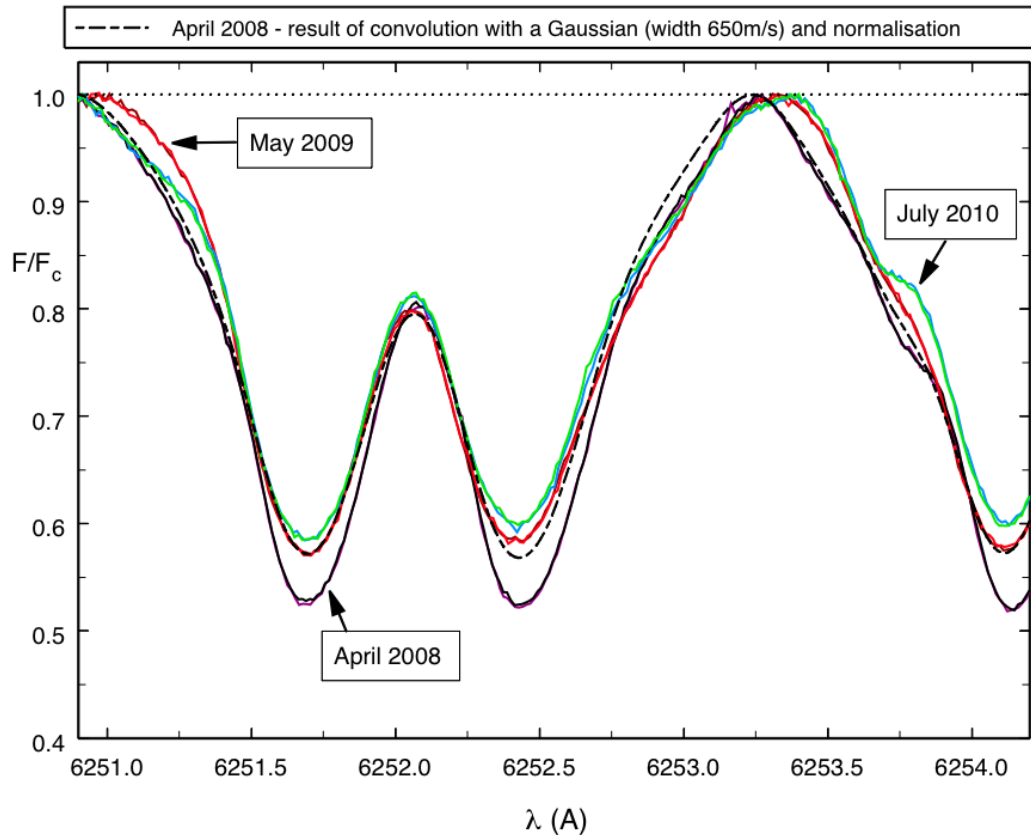


Figure 58: A 5Å window showing two spectra from 2008, 2009 and 2010. The dashed line shows the result of convolving the 2008 data with a gaussian with a width of 650 m/s - closest fit when comparing core and peak widths (ignoring the effects of temperature change). The result of the convolution mimics the more broadened spectra of 2009. The peaks either side of the vanadium-iron pair will vary with the broadening.

positions, we do not observe the usual correlation between shallower lines and deeper blending regions. But we do see that, on average, the difference between the line depths and the depths ($1-F/F_c$) of the blending peaks that are to either side of them is smaller for the broader lines of 2009 and 2010. That is the core depths change more than the depths of the blends. Though our normalization technique does result in inadequacies in this regard, since there is no *true* continuum in this part of the spectra of red supergiants (Chiavassa *et al.* 2010) and we are currently concerned with variations in the spectral

lines rather than absolute measures we deem consistent normalization between all spectra to be more important than modeling to find a true continuum, which would be both time and resource intensive and, due to the complex nature of the spectra of cool stellar atmospheres, no more correct. In Figure 58 we take this analysis a little further and convolve the sharp lines of 2008 with a Gaussian in an attempt to reproduce the less sharp spectral features seen in 2009. The *dashed* line shows the results of convolving the 2008 spectrum with a Gaussian with a FWHM of 650 m/s. The fit is far from perfect but the blend between the 6252Å and 6253Å lines has been reduced to the same level as the spectrum of 2009 and the blended feature in the blue wing of the 6254Å line is blurred to near the same level as observed in 2009.

These small changes in line broadening are consistent with the arguments put forth by Gray (2008) that the observed macroturbulence seen in spectral line shapes stems from the medium convective scale. That is, it stems from the cells within the larger convective cells which dominate the light and radial velocity. If we were instead observing the global macroturbulence one would expect to see large changes in the line shapes, associated with the waxing and waning of the cells through the atmosphere, that are correlated with the radial velocity.

Since the typical large convective element is of order ~5% of the stellar radius (results for Betelgeuse from Gray 2008 and Chiavassa *et al.* 2009) these relatively small changes in line shape suggest that we are only observing one convective cell at a time. This assumption arises since each convective cell should have different internal macroturbulence and a different projection, thus the combination of two different cells will cause much large changes in the shapes of spectral lines as the number and location of cells changes. In extreme cases this could lead to line splitting if, for example, we had two cells on opposite sides of the disk center and in different phases in their convective cycles.

6.4 The Significance of Third Signature Reversal

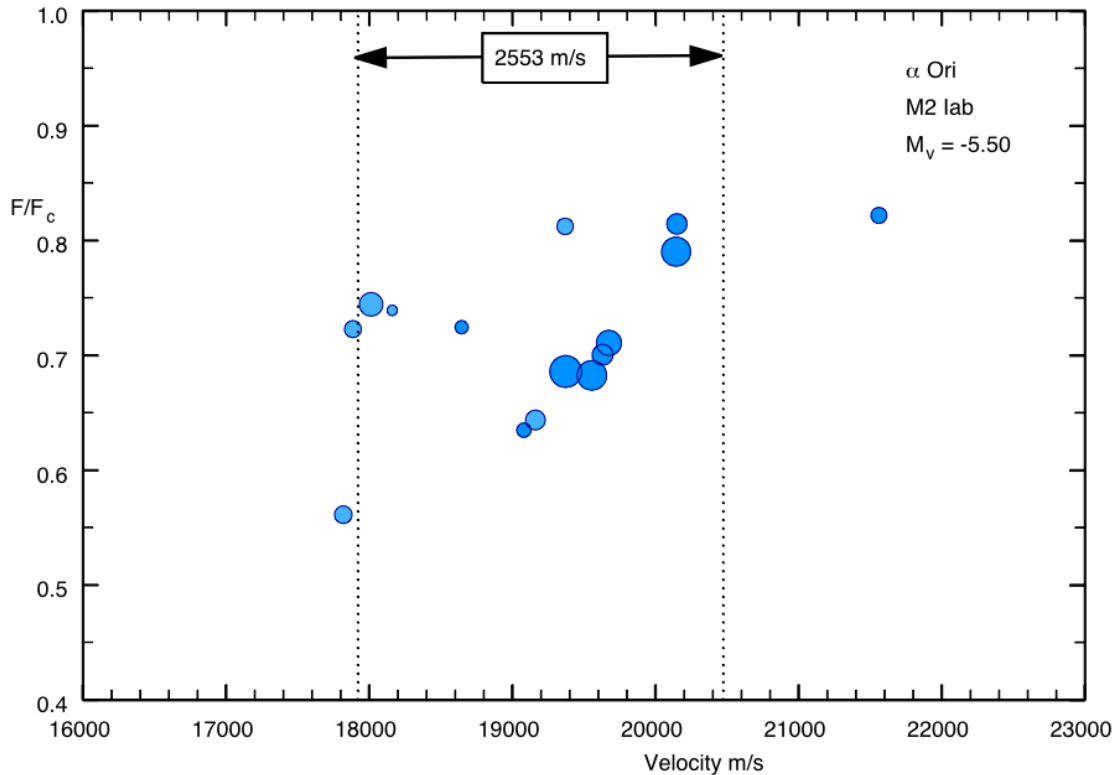


Figure 59: Third signature of Betelgeuse, constructed from the mean of three exposures with a total signal-to-noise ratio of 1810. Symbol sizes indicate the point weight and errors are approximately the size of the largest symbols. *Dotted lines delineate the third signature span based on the weighted average of the three minimum and three maximum radial velocities.*

The reversal of the third signature seen in Antares A (section 6.2.2) was reported by Gray & Pugh (2012) for this star and a number of other bright giant and supergiant stars. Figure 59 shows an example for the M1.5 supergiant Betelgeuse (α Ori) which was made as part of this thesis. Further, some of the stars from Gray & Pugh (2012) were also found to show transitional behavior - shallow lines show reversal and strong lines show a somewhat solar-like distribution. Of the nine supergiant stars in that paper we found that three demonstrated reversal, two were *transitional*, and the remaining four showed a solar-like distribution. If we include the supergiant Betelgeuse then four of ten supergiants show third signature reversal. Given the variation in the third-signature

exhibited by Antares (Figure 53), the interpretation that this is due to differential expansion, and the known variability of cool high luminosity stars, the fact that $\sim 50\%$ of our sample was found to demonstrate reversal should not be surprising. In fact, one might expect that all high luminosity variable stars demonstrate third-signature reversal at one time or another.

In the cases of full third signature reversal, we noticed that the largest range in line core positions occurred for the most luminous stars. To further investigate this trend, we measured the span of the velocities by taking the weighted means of the three redward and the three blueward extreme points, as is shown in Figure 59. This span was interpreted as a proxy for the photospheric velocity gradient. Measures of the radial velocity span were made for each of the stars demonstrating reversal, five in total: Antares, Betelgeuse, the M3 giant μ Gem, the G5 supergiant 22 Vul, and the K2 supergiant 47 Cyg.

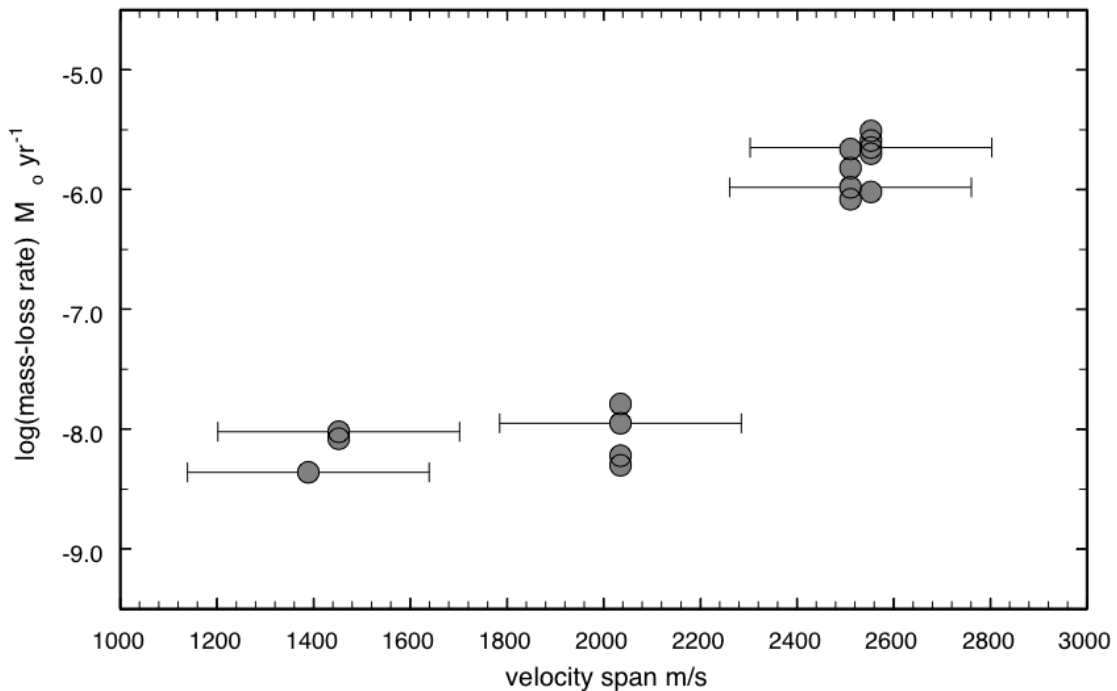


Figure 60: Mass-loss rate as a function of third-signature velocity span. Typical errors due to changes in the third-signature shape are estimated from data of Antares (Figure 55) and Betelgeuse, and are shown by the error bars.

Initially, and mistakenly, the reversal was interpreted as a signature of mass-loss and in fact there is a hint of a trend of the velocity scaling with mass-loss rate (Figure 60). We searched the literature to find observational, as well as analytical, determinations of mass-loss rates. The 6 cm emission from 47 Cyg is known to be anomalously high (Drake *et al.* 1987) and may bias our small sample. It is found to be ~ 3 times higher than that of similar stars. If we adjust for this factor, we find the mass-loss rate shown in Table 6. There is considerable range in the mass-loss rates for each star, as might be anticipated considering the diverse methods that were used. Nevertheless, the range of values is much larger than the scatter and we show in Figure 60 the relation between mass-loss and photospheric velocity span. Larger velocity differential in the photosphere goes with larger mass-loss rate. Span velocities and mass-loss rates are given in Table 7.

Table 7: Photospheric velocity spans and mass-loss rates

Name	Velocity Span (m/s)	$\log \dot{M}$ (M_{\odot}/yr)	Error (%)	Citation
μ Gem	1389	-8.36	not given	Drake & Linsky (1986)
α Sco	2511	-6.08	± 13	de Jager <i>et al.</i> (1988)
		-5.66	not given	Bernay (1977)
		-5.98	± 28	Riemers <i>et al.</i> (2008)
		-5.82	± 20	Schorder & Cuntz (2007)
22 Vul	2035	-8.22	± 26	de Jager <i>et al.</i> (1988)
		-7.95	not given	Schoeder & Reimers (1989)
		-8.30	not given	Ahmed & Stencel (1988)
47 Cyg	1452	-8.02	± 18	Drake <i>et al.</i> (1987)
		-8.08	not given	Mallik (1993)
α Ori	2553	-6.02	± 13	de Jager <i>et al.</i> (1988)
		-4.47	not given	Bernat (1987)
		-5.51	not given	Mauron & Josselin (2011)
		-5.65	± 20	Schorder & Cuntz (2007)
		-4.83	± 41	van Loon <i>et al.</i> (2005)
		-5.70	± 50	Hugins <i>et al.</i> , (1994)

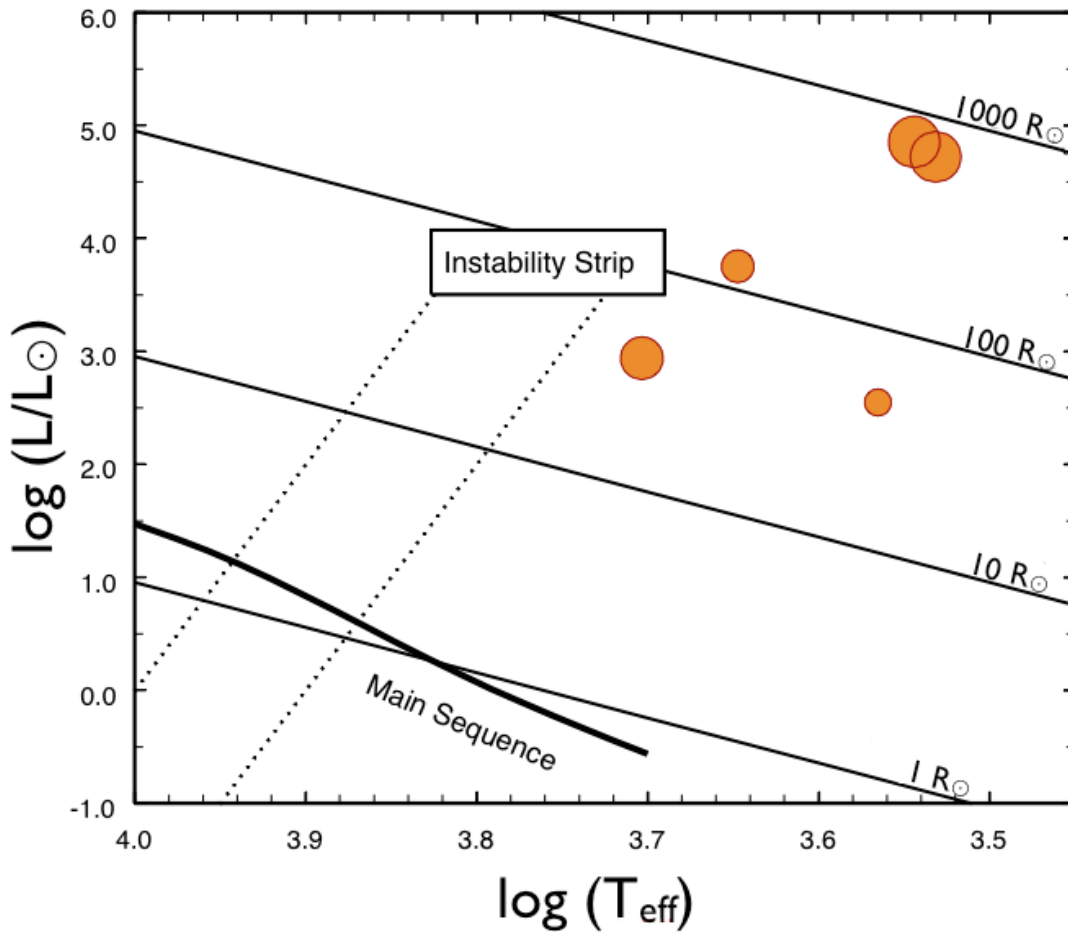


Figure 61: A section of the HR diagram from Figure 1, each orange point represents a star from Table 6. The symbol size represents the third-signature velocity span.

These velocities are smaller than the photospheric escape velocities and larger than we predict from the wind velocities. It seems more feasible that the measured velocity span scales with one or more of the global stellar parameters, which themselves influence the mass-loss rates. In place of the velocity mass-loss plot of Figure 60, we instead plot the stars as individual points on the HR diagram from Figure 1 (shown in Figure 61). The symbol size indicates the size of the velocity span and indeed we see a general trend that the point size increases as we move upward and rightward in the HR diagram. There are certainly small discrepancies, most obviously 22 Vul has a larger velocity span than 47

Cyg, this could arise from either the measurement technique or the star. 22 Vul falls just to the cool side of the Linksy & Haisch dividing line, shown in Figure 2, and as such may be physically different from the other stars considered. 22 Vul has a high wind velocity, a high rotation velocity, is in a close binary system, and has a cool chromosphere (Eaton & Shaw 2007). It has further been suggested that this system has likely undergone mass transfer. Thus, 22 Vul is likely quite different from the other systems considered here, however given the lack of available third-signature spans we include it for completeness. Additionally, without further investigation into the shapes of third-signatures, we can not guarantee that the differences will affect the third-signature.

We have seen that third signature shape changes on a time scale of months (Figure 55). Thus we must admit that the observed differences in velocity span may arise from differences in phase of that variation. Based on the observed shape changes in the third-signature of Antares (Figure 54), we anticipate that the error introduced by such variations is ~ 200 m/s. However, without further observations, we can not dismiss that the variation could be substantially larger than this.

One may interpret the third-signature span, as presented in Figure 59, to be a measure of the scale of the pulsation that is driving differential expansion (see section 6.2.2). In this case, the proximity of 22 Vul to the classical instability strip could explain why its velocity span is increased compared to that of 47 Cyg. Unfortunately, no studies of the variations of 22 Vul, beyond the orbital motion, could be found. Knowing if 22 Vul is subject to greater pulsation velocities than 47 Cyg is impossible without further spectral observations. We currently have very few observations of these two stars, spanning only a number of weeks.

6.5 Differences between Antares and Betelgeuse

Currently the majority of the evidence for giant convection cells is based on observations and models of Betelgeuse. While this gives an understanding of convection and granulation in the upper right of the HR diagram, convection in this regime is extreme

and stellar parameters are highly uncertain such that it is not unlikely that there are large differences between each of these stars. Antares and Betelgeuse are very good stellar analogues to test the robustness of convective theory, since they are of very similar spectral types, have similar masses, luminosities and radii. In Table 8 we review the parameters of these two similar red supergiants.

Table 8: Observational details of Antares and Betelgeuse

	Antares	Betelgeuse
Spectral Type	M1.5 Iab-b	M2 Iab
Mass	$18 \pm 4 M_{\odot}$ (Schröder & Cuntz 2007)	8 - 20 M_{\odot} (Mohamed <i>et al.</i> 2012)
M_v	-5.2 ± 0.9	-5.4 ± 0.8
Radius	$890 \pm 150 R_{\odot}$	$1100 \pm 150 R_{\odot}$
Luminosity	$48,000 \pm 1000 L_{\odot}$ (Schröder & Cuntz 2007)	$120,000 \pm 30,000 L_{\odot}$ (Smith <i>et al.</i> 2009)
B-V	1.82 (Lee 1970)	1.85 (Nicolet 1978)
Temperature (from B-V)	3570 K	3500 K
$\log g$	0.1 ± 0.3 (El Eid 1994)	-0.5 ± 0.3 (Lobel & Dupree 2000)

NOTE – Absolute magnitudes are determined from the Hipparcos parallax. Radii are determined from the parallax and angular diameters. For Antares the diameter is from Richichi & Lisi (1990) for Betelgeuse we use the mean of four measures: Michelson & Pease (1921), Buscher *et al.* (1990), Wilson *et al.* (1992), and Tuthill *et al.* (1997).

We see from Table 8 that in spite of their similarities, Antares and Betelgeuse are relatively different. Despite their similar radii and temperatures (resulting in a R^2T^4 ratio of 1.4), their luminosities are different (ratio in L of 2.5). Additionally there is a large difference in their surface gravities, likely stemming from difference in their mass. Though the errors on their masses imply that they could have similar values, the differences in $\log g$ (caution, within errors these could be the same) and luminosity suggest that these stars actually have quite different masses. The difference in surface

gravity suggests different conditions with the photospheres of these two supergiants. Betelgeuse's lower surface gravity will result in a less contained more tenuous atmosphere. These atmospheric differences will result in slight differences in the nature of their respective atmospheric variations. For example, the same initial perturbations will progress differently through the two atmospheres. In Table 9 we review the observed periods and amplitudes of visual and radial velocity variability.

Table 9: Variability of Antares and Betelgeuse

	Antares	Betelgeuse
Visual Amplitude (mag)	0.3 ¹	1.3 ¹
v_R Amplitude (km/s)	5.4 & 1.5-3 ¹⁰ 6 & 5 ⁷ 4.6 ² 4.2 ³	3 & 3-4 ⁷ 6 ² 4.1 ³
Visual Period (days)	7140±10 & 1260±400 ¹⁰ 1650±640 ⁴ 1733 ⁵ 350 ⁶	2050±460 & 388±30 ⁴ 2200 ⁵ 2000, 200 ⁶
v_R Period (days)	2167±5 & 100±6 ¹⁰ 240±20 ⁷ 2120 ⁸ 2685 ³	420±20 ⁷ 2190 ⁹ 2110 ³

Variability citations:—

- 1) AAVSO
- 2) Lunt (1916)
- 3) Spencer-Jones (1928) - period for Antares is likely in error (Section 6.1.3)
- 4) Kiss *et al.* (2006)
- 5) Stothers & Lueng (1971)
- 6) Percy *et al.* (1996)
- 7) Smith *et al.* (1989)
- 8) Halm (1909)
- 9) Bottlinger (1911)
- 10) This thesis

With the stellar variations tabulated in this manner it becomes apparent that there are a few differences in their variability:

- i. In the case of Antares we found a 7140-day period in the photometry. A similar period has not been reported for Betelgeuse, though given our proposed mechanisms (Section 6.1.4) such periods are likely common amongst red supergiants.
- ii. While the photometric and radial velocity periods of Betelgeuse are similar (2000-2200 days), in Antares we see a marked difference between the two data sets.
- iii. Betelgeuse has substantially larger photometric amplitude than Antares.

As far as we are aware the ~ 2000 day period in the radial-velocity of Betelgeuse has not been shown/found to demonstrate the same stability as we see for Antares. Also, we find convective scales of Betelgeuse to be an order of magnitude larger than for Antares.

With such an interpretation made, we then have to ask if it is possible that the differences in stellar luminosity, $\log g$, and mass could be responsible for these differences or if we must also consider the internal structure of the stars (i.e. shell burning vs. core burning, depth of the convective and so on)? For the most simple of considerations, we look to mixing length theory to provide us with some idea. The height over which a convective cell migrates is termed the mixing length and is proportional to the pressure scale height, H_p , of the atmosphere. The pressure scale height is given by $H_p = kT/mg$. It is likely then that the largest difference in convective cell sizes between these two stars stem from their relative surface gravities and thus their relative masses. Using the above formulation for the pressure scale height, we find that one would expect Antares to have a pressure scale height that is only one quarter the size of that of Betelgeuse. Using the assumptions of Schwarzschild (1975), we assume that the convective cells extend over several pressure scale heights, thus the cells of Antares should be only one quarter as large as the cells in Betelgeuse. This is simply an order of magnitude estimate, Betelgeuse's mass is not well constrained and we can by no means guarantee that the convective cells extend over the same number of pressure scale heights in both cases. Based on such arguments one might expect these two stars to show the kind of observational differences that we see here.

Chapter 7

7 Conclusion

As expected Antares is highly enigmatic and we see many dynamical timescales associated with this system. In this section we review our findings and add a few thoughts on how, in light of these findings, our assumptions about red supergiants might have to be altered. The final section here addresses future work, since this system (and others like it) have many variations that occur over half a decade or more there is a lot more that can still be done to aid our understanding.

7.1 The Variations of Antares A

Antares A is a very dynamically complicated star. In addition to its documented orbital period of 1220 years (Manson *et al.* 2001), we report a photometric period of 7140 days (~ 19 years) the origins of which remain unclear. Pre-whitening of the photometry for this period results in a further period of ~ 1260 days being measured from the resulting Fourier amplitude spectrum. Which we suggest is an analogue of the solar 5-minute oscillation and stems from repeated perturbation of the atmosphere by giant convective cells. Evidence for this argument comes from the measure of multiple periods of approximately this length that stem from various observational windows. No evidence of this variation is apparent in the spectral data.

By combining our data with historical radial velocity measures we determine a period of 2167 ± 5 days, which due to a 70-day phase difference with our line-depth ratio variations, we assumed had a pulsation origin. Based on this interpretation we predict a change in radius of $\sim 165 \pm 22 R_{\odot}$ which should have resulted in a magnitude variation ~ 0.2 mag. Such a variation is not observed in the AAVSO photometry which at this point we cannot explain, though we do note the similarities between this variation and those seen in semi-regular variables with long secondary periods. If this 2167-day variation were to have the same origin as those long secondary periods (which remain unexplained) then one

might not expect to see an associated magnitude change. The photometric amplitudes of typical long secondary periods are several tenths in the visual, though they can be much smaller than this (Nicholls *et al.* 2009). It seems likely that this is a long secondary period, though further long-term high-precision photometry would be required to confirm this speculation.

Observed changes in the third-signature shape from 2008 - 2009 are thought to arise from differential pulsation: the weak lines, which are formed deeper in the photosphere, demonstrate much larger change in radial velocity than the strong lines, implying that the pulsation velocity decreases with altitude.

By using the historic data along with our measurements, we determined the shape of the long-term radial-velocity trend which was then subtracted from our data to highlight the short-term trends. From the residual radial-velocities we determined a period of 100 ± 6 days, for a variation that experiences phase and amplitude changes. These changes suggest a chaotic driving mechanism. We see a small correlation between the radial-velocity and temperature variations. Again we see evidence for an underlying mechanism that is highly chaotic. Additionally we see third signature shape changes in concert with the 100-day radial velocity variation - larger radial velocity amplitude corresponds to a greater change in third-signature shape and the largest changes are seen for shallow lines. Due to the chaotic nature of the radial-velocity and temperature changes on these timescales, we conclude that the 100-day variation in radial velocity, third-signature shape and temperature is the effect of a large convective element penetrating/perturbing the stellar photosphere. Due to the stochastic nature of these convective elements, we see times of large velocity change but very little temperature change and times of large temperature change with little velocity change.

Like Betelgeuse, evidence of convective cycling is apparent, though the scales (temperature and radial velocity) are much reduced by comparison suggesting that the convective motions in Antares are less dramatic and that the convective cells themselves are smaller. This conclusion is supported by the comparison of stellar parameters, due to the dependence of pressure scale height upon surface gravity and hence mass; Antares

should have a smaller pressure scale height which may lead to smaller convective elements.

There is an additional comment we feel it is pertinent to make here. In the past few decades (most recently Stothers 2010) the ~ 6 yr radial velocity period of Antares A was treated as having the same origin as the photometric periods ~ 1000 - 2000 days. The work presented in Section 6.1.3 above and in Pugh & Gray (2013) suggests that this interpretation may be in error. The phasing of the various radial velocity data (Figure 42) is far too good to be explained by the type of chaotic phenomenon that would result in periods ranging from 1000 - 2200 days. Thus, such previous assessments should be reexamined. Additionally, since other red supergiants (usually Betelgeuse and α Her A) have been subject to the same scrutiny as Antares in previous investigations the historical radial velocity data of these stars should be examined in similar fashion to our investigation of Antares (Pugh & Gray 2013).

7.2 Third-Signature Reversal

We have seen that approximately 50% of cool high-luminosity stars demonstrate third-signature reversal. Since, we interpret the long-term variation in third signature shape (and hence third signature reversal) as arising from differential expansion we can make a simple numerical estimate: if all cool and evolved stars show some level of pulsation then at any one time we observe a group of these stars we should expect to see 50% of them in a contraction phase and 50% in an expansion phase. (These numbers will differ slightly for irregular pulsation but still give a good ball park estimate.) Similarly, we should also observe that at any one time approximately 50% of these stars should show third-signature reversal, which is what was reported in Gray & Pugh (2012). During the time of reversal we see a scaling of the velocity-span with the global stellar parameters. We see only one discrepancy from this trend, the hybrid-wind star 22 Vul. This may suggest that the scaling of the third signature depends upon the pulsation parameters, though further investigation is required to determine the true scaling.

7.3 Future Work

In the study of the variability of red supergiants, we inevitably run into the problem of requiring long, well-sampled data sets in order to truly be able to measure the variability. This study of Antares highlights the issue. The detection of a 7140-day period in the photometry stresses this fact. It is vital to the interpretation of this period, and those like it, that long-term spectral observations of red supergiants continue to be made.

Further observations and models are needed for red supergiants beyond Betelgeuse. It is obvious from this study that our understanding of the variability of red supergiants is incomplete. While basing our knowledge on that gained so far is natural, we should be cautious to not allow it to overly colour our judgment. In this thesis we have seen that our understanding of the nature of convection and variability of red supergiants gained from the various studies and models of Betelgeuse is not complete – this is not entirely surprising. Consider the following question: how do evolutionary state and internal structure affect convection and pulsation? The study of a single star or two can not answer such a question. Given the complex evolutionary tracks that lead to red supergiants, it is likely that many of these stars are in very different evolutionary states. Not only are long-term observations of these stars needed but also multi-object studies and, in a perfect world, multi-instrument studies. In addition, photometric errors of bright stars are substantially larger than of stars just a magnitude or two fainter; thus better lightcurves can be produced by observing such red supergiants.

There is currently a difficulty in theoretically explaining the small changes in spectral line shape compared to other spectral features. The differences suggest that large convective elements dominate the line positions, while small convective scales dominate the line shapes. A theoretical/physical understanding of how this arises is not entirely clear. Gray (2008) suggested that one bright convective element dominated the intensity and thus was responsible for the changes in line position and predicted a displacement of $\sim 5\%$ of the stellar radius. Chiavassa *et al.* (2010) suggest two convective scales, consistent with analysis of Schwarzschild (1975), one of order a few percent of the stellar radius and one near 50-60% of the stellar radius. They suggest that the “few percent” variety is what is visible from the photosphere which is consistent with the findings of

Gray (2008) and this thesis. The typical theoretical result however shows more than one bright element on this scale, it is unlikely that such a distribution of cells would result in such small changes in line shape. Theorists in recent decades have worked closely with interferometric observers to explain the pattern of observed bright spots, it is time for a closer relationship between theorists and spectral observers. Stellar spectra grant a window into photospheric physics unlike any other observational technique and it is imperative to our understanding of convection that this tool is utilized to its fullest.

The temporal variations of third-signature plots offer new light into the dynamics of stellar photospheres, in tandem with other observations they offer yet another tool on which to base our interpretations. These plots offer a very valuable tool to constrain models of convection and pulsation in these stars. It is so far though, not a well studied phenomenon and requires further investigation.

Bibliography & References

- Aerts, C., Christensen-Dalsgaard, J., & Kurtz, D. W. (2010). *Asteroseismology*. Springer.
- Ahmed, I. A., & Stencel, R. E. (1988). The stellar wind velocity function for red supergiants determined in eclipsing binaries. *ApJ*, 329, 797-802.
- Allen, C. W. (1973). *Astrophysical Quantities*. London: University of London, Athlone Press.
- Allende Prieto, C., & Garcia Lopez, R.-J. (1998). Fe I line shifts in the optical spectrum of the Sun. *A&A Supplement*, 129, 41-44.
- Allende Prieto, C., Lambert, D. L., Tull, R., & MacQueen, P. J. (2002). Convective Wavelength Shifts in the Spectra of Late-Type Stars. *ApJL*, 566, L93-L96.
- Athay, G. R., & White, O. R. (1978). Chromospheric and coronal heating by sound waves. *ApJ*, 226, 1135-1139.
- Baade, R., & Reimers, D. (2007). Multi-component absorption lines in the HST Spectra of alpha Scorpii B. *A&A*, 474, 229-237.
- Bak, P., Tang, C., & Wiesenfeld, K. (1988). Self-Organized Critically. *Phys. Rev. A*, 38, 364-374.
- Bartolini, C., Blanco, C., Catalano, S., Cerruti-Sola, M., Eaton, J. A., Guarnieri, A., et al. (1983). Remarkable light changes of the active RSCVn system V 711 Tau /equals HR 1099/ during 1979-1981. *A&A*, 117, 149-155.
- Batten, A. H. (1973). *Binary and Multiple Systems of Stars* (Vol. (international series of monographs in natural philosophy; v. 51)). Oxford; New York: Pergamon Press.
- Beckers, J. M. (1981). Dynamics of the solar photosphere. *NASA Special Publications*, 450, 11-64.

Bedding, T. R. (2003). Solar-like Oscillations in Semiregular Variables. *Ap&SS*, 284, 61-64.

Bedding, T. R., Huber, D., Stello, D., Elsworth, Y. P., Hekker, S., Kallinger, T., et al. (2010). Solar-like Oscillation in Low-Luminosity Red Giants: First Results from Kepler. *ApJL*, 713, L176-L181.

Bedding, T., Kiss, L., & Kjeldsen, H. (2003). Solar-Like Oscillations in Red Giants. *IAU Joint Discussion, I2*, p. 52.

Bedding, T. R., Zijlstra, A. A., Jones, A., & Foster, G. (1998). Mode switching in the nearby Mira-like variable R Doradus. *MNRA*, 301, 1073-1082.

Bennett, P. D. (2010). Chromospheres and Winds of Red Supergiants: An Empirical Look at Outer Atmospheric Structure. In C. Leitherer, P. D. Bennett, P. W. Morris, & J. T. Loon (Ed.), *Hot and Cool: Bridging Gaps in Massive Star Evolution*. 425, p. 181. Astronomical Society of the Pacific Conference Series.

Bernat, A. P. (1977). The circumstellar shells and mass loss rates of four M supergiants. *ApJ*, 213, 756-766.

Bersier, D., Burki, G., & Burnet, M. (1994a). Fundamental parameters of Cepheids. I. Photometric data in the Geneva system. *A&AS*, 108, 9-24.

Bersier, D., Burki, G., Mayor, M., & Duquennoy, A. (1994b). Fundamental parameters of Cepheids. II. Radial velocity data. *A&AS*, 108, 25-39.

Bester, M., Danchi, W. C., Hale, D., Townes, C. H., Degiacomi, C. G., Mekarnia, D., et al. (1996). Measurement at 11 Micron Wavelengths of the Diameters of alpha Orionis and alpha Scorpii: Changes in Effective Temperature of alpha Orionis and Very Recent Dust Emission. *ApJ*, 463, 336.

Biermann, L. (1938). Leuchtkraft und Konvektion bei Sternmodellen mit sehrstarker Konzentration der Energiequellen. *AN*, 266, 1.

- Bohm-Vitense, E. (1955). Hydrogen in the Solar Chromosphere and Photosphere. *PASP*, 67, 21.
- Bottlinger, C. F. (1911). Die Bahn des spektroskopischen Doppelsternes alpha Orionis. *AN*, 187, 33.
- Bowen, G. H. (1988). Dynamical modeling of long-period variable star atmospheres. *ApJ*, 329, 299-317.
- Bowen, G. H. (1990). The extended atmospheres of pulsating stars. *Annals of the New York Academy of Sciences*, 617, 104-117.
- Bowen, G. H., & Willson, L. A. (1991). From wind to superwind - The evolution of mass-loss rates for Mira models. *ApJL*, 375, L53-L56.
- Brown, K. I., Gray, D. F., & Baliunas, S. L. (2008). Long-Term Spectroscopic Monitoring of Arcturus. *ApJ*, 679, 1531-1540.
- Burns, D., Baldwin, J. E., Boysen, R. C., Haniff, C. A., Lawson, P. R., Mackay, C. D., et al. (1997). The surface structure and limb-darkening profile of Betelgeuse. *MNRAS*, 290, L11-L16.
- Buscher, D. F., Baldwin, J. E., Warner, P. J., & Haniff, C. A. (1990). Detection of a bright feature on the surface of Betelgeuse. *MNRAS*, 245, 7P-11P.
- Butler, R. P., Marcy, G. W., Williams, E., McCarthy, C., Dosanji, P., & Vogt, S. S. (1996). Attaining Doppler Precision of 3 m s⁻¹. *PASP*, 108, 500.
- Cadmus, R. R., Willson, L. A., Sneden, C., & Mattei, J. A. (1991). Observation of possible mode switching in three semiregular variable stars. *AJ*, 101, 1043-1049.
- Carney, B. W., Latham, D. W., Stefanik, R. P., Laird, J. B., & Morse, J. A. (2003). Spectroscopic Binaries, Velocity Jitter, and Rotation in Field Metal-poor Red Giant and Red Horizontal-Branch Stars. *AJ*, 125, 293-321.

- Castor, J. I., Abbott, D. C., & Klein, R. I. (1975). Radiation-driven winds in Of stars. *ApJ*, 1965, 157-174.
- Catalano, S., Biazzo, K., Frasca, A., & Marilli, E. (2002). Measuring starspot temperature from line depth ratios. I. The method. *A&A*, 394, 1009-1021.
- Chiavassa, A., Haubois, X., Young, J. S., Plez, B., Josselin, E., Perrin, G., et al. (2010). Radiative hydrodynamics simulations of red supergiant stars. II. Simulations of convection on Betelgeuse match interferometric observations. *A&A*, 515, 12-22.
- Chiavassa, A., Plez, B., Josselin, E., & Freytag, B. (2006). Radiative transfer in snapshots of 3D radiative hydrodynamic models of red supergiants. In P. Stee (Ed.), *EAS Publication Series*, 18, pp. 177-189.
- Chiavassa, A., Plez, B., Josselin, E., & Freytag, B. (2009). Radiative hydrodynamics simulations of red supergiants. I. interpretation of interferometric observations. *A&A*, 506, 1351-1365.
- Chugainov, P. F. (1966). On the Variability of HD 234677. *IBVS*, 122, 1.
- Cox, J. P. (1980). *Theory of stellar pulsation*. Princeton University Press.
- Cranmer, S. R., & Saar, S. H. (2011). Testing a Predictive Theoretical Models for the Mass Loss rates of Cool Stars. *ApJ*, 741, 54.
- Cruzalebes, P., Lopez, B., Bester, M., Gendron, E., & Sams, B. (1998). Near-infrared adaptive optics imaging of dust shells around five late-type stars with COME-ON+. *A&A*, 338, 132-138.
- Cummings, I. N. (1998). *PhD. Thesis*. University of Canterbury.
- Danchi, W. C., Greenhill, L., Bester, M., Degiacomi, C. G., & Townes, C. H. (1992). Long Baseline Interferometric Observations of the Spatial Distribution of Dust Surrounding Late-Type Stars at 11 microns. *American Astronomical Society Meeting Abstracts*. 24, p. #114.05. Bulletin of the American Astronomical Society.

- de Jager, C., Nieuwenhuijden, H., & van der Hucht, K.-A. (1988). Mass loss rates in the Hertzsprung-Russell diagram. *A&AS*, 72, 259-289.
- Demarque, P., & Guenther, D. B. (1999). Heliosismology: Probing the Interior of a Star. *Proceedings of the NAS*, 96, 5356-5359.
- Deutsch, A. J. (1956). The Circumstellar Envelope of Alpha Herculis. *ApJ*, 123, 210.
- Doppler, C. (1846). *Beitrage zur fixsternenkunde*. Prag: Druck von G. Hasse sohne, 1846.
- Drake, S. A., & Linsky, J. L. (1986). Radio continuum emission from winds, chromospheres, and coronae of cool giants and supergiants. *AJ*, 91, 602-620.
- Drake, S. A., Brown, A., & Reimers, D. (1987). Radio Continuum Emission from the Ionized Stellar Winds of the Cool Supergiants in Zeta Aurigae-Like Systems. In J. L. Linsky, & R. E. Stencel (Ed.), *Cool Stars, Stellar Systems, and the Sun*. 291, p. 322. Lecture Notes in Physics, Berlin: Springer Verlag.
- Dravins, D., & Nordlund, A. (1986). Stellar Granulation: Photospheric Line Asymmetries and Hydrodynamic Model Atmospheres. *Bulletin of the American Astronomical Society*, 18, p. 1002.
- Dravins, D., Lindgreen, L., & Nordlund, A. (1981). Solar granulation: Influence of convection on spectral line asymmetries and wavelength shifts. *A&A*, 96, 345-364.
- Eaton, J. A., & Shaw, F. G. (2007). Properties of the zeta Aur-Type Binary System 22 Vul = QS Vul. *AJ*, 133, 2669-2678.
- Eaton, J. A., Henry, G. W., & Odell, A. P. (2008). Orbits and Pulsations of the Classical 'zeta' Aurigae Binaries. *ApJ*, 679, 1490-1498.
- El Eid, M. F. (1994). CNO isotopes in red giants: theory versus observations. *A&A*, 285, 915-928.
- Etoka, S., & Le Squeren, A. M. (1997). OH eruptive Mira stars. *A&A*, 321, 877-887.

- Evans, D. S. (1957). Antares: a discussion of the observations. *AJ*, 62, 83-88.
- Evans, D. S. (1961). Observations of twenty-four single-lined variables. *Royal Greenwich Observatory Bulletins*, 44, 351-363.
- Franks, W. S. (1907). The relation between star colours and spectra. *MNRAS*, 67, 539.
- Fredrick, L. W. (1960a). Observations of epsilon Aurigae. *AJ*, 65, 97-100.
- Fredrick, L. W. (1960b). The system of VV Cephei. *AJ*, 65, 628-643.
- Freytag, B. (2006). Convection in giant stars. In M. Rieutord, & B. Dubrulle (Ed.), *EAS Publication Series*, 21, pp. 325-333.
- Freytag, B., & Hofner, S. (2008). Three-dimensional simulations of the atmosphere of an AGB star. *A&A*, 483, 571-583.
- Freytag, B., Steffen, M., & Dorch, B. (2002). Spots on the surface of Betelgeuse -- Results from new 3D stellar convection models. *AN*, 323, 213-219.
- Gray, D. F. (1978). Turbulence in stellar atmospheres. *SoPh*, 59, 193-236.
- Gray, D. F. (1980). Analysis of high resolution stellar line profiles. In D. F. Gray, & J. L. Linsky (Ed.), *IAU Colloq. 51: Stellar Turbulence* (pp. 75-84). Lecture Notes in Physics, Berlin: Springer Verlag.
- Gray, D. F. (1981). Asymmetries in the spectral lines of Procyon. *ApJ*, 251, 583.
- Gray, D. F. (1982). Observations of spectral line asymmetries and convective velocities in F, G, and K stars. *ApJ*, 255, 200-209.
- Gray, D. F. (1988). *Lectures on spectral-line analysis: F, G, and K stars*. Arva: Onatrio Gray, 1988.
- Gray, D. F. (2000). Betelgeuse and Its Variations. *ApJ*, 532, 487-496.

- Gray, D. F. (2005). *The Observation and Analysis of Stellar Photospheres* (3rd ed.). UK: Cambridge University Press, 2005.
- Gray, D. F. (2008). Mass Motions in the Photosphere of Betelgeuse. *AJ*, *135*, 1450-1458.
- Gray, D. F. (2009). The Third Signature of Stellar Granulation. *ApJ*, *697*, 1032-1043.
- Gray, D. F. (2010). Empirical Decoding of the Shapes of Spectral-Line Bisectors. *ApJ*, *710*, 1003-1008.
- Gray, D. F., & Brown, K. (2001). Line-Depth Ratios: Temperature Indices for Giant Stars. *PASP*, *113*, 723-735.
- Gray, D. F., & Brown, K. I. (2006). Precise Spectroscopic Radial Velocity Measurements Using Telluric Lines. *PASP*, *118*, 399-404.
- Gray, D. F., & Pugh, T. (2012). The Third Signature of Granulation in Bright-giant and Supergiant Stars. *AJ*, *143*, 92.
- Gray, D. F., & Stevenson, K. B. (2007). Spectroscopic Determination of Radius Changes of Cepheid Variable Stars. *PASP*, *119*, 398-406.
- Gray, D. F., & Toner, C. G. (1986). The remarkable spectral line asymmetries of F and G Ib supergiant stars. *PASP*, *98*, 499-503.
- Gray, D. F., Carney, B. W., & Yong, D. (2008). Asymmetries in the Spectral Lines of Evolved Halo Stars. *AJ*, *135*, 2033-2037.
- Griffin, R., & Griffin, R. (1973). Accurate wavelengths of stellar and telluric absorption lines near lambda 7000 Angstroms. *MNRAS*, *162*, 255.
- Grunhut, J. H., Wade, G. A., Hanes, D. A., & Alecian, E. (2010). Systematic detection of magnetic fields in massive, late-type supergiants. *MNRAS*, *408*, 2290-2297.
- Gunn, J. E., & Griffin, R. F. (1979). Dynamical studies of globular clusters based on photoelectric radial velocities of individual stars. I - M3. *AJ*, *84*, 752-773.

- Guo, J. H., & Li, Y. (2002). Evolution and Pulsation of Red Supergiants at Different Metalicities. *ApJ*, *565*, 559-570.
- Hale, G. E. (1908). The Zeeman Effect in the Sun. *PASP*, *20*, 287.
- Halm, J. (1909). *Cape Annals*, *10*, 56.
- Hamilton, D., & Lester, J. B. (1999). A Technique for the Study of Stellar Convection: The Visible Solar Flux Spectrum. *PASP*, *111*, 1132-1143.
- Hansen, C. J., & Kawaler, S. D. (1994). *Stellar Interiors - Physical Principles, Structure, and Evolution*. Berlin: Springer.
- Harper, G. M., Brown, A., & Lim, J. (2001). A Spatially Resolved, Semiempirical Model for the Extended Atmosphere of alpha Orionis (M2 Iab). *ApJ*, *551*, 1073-1098.
- Hartmann, L., & MacGregor, K. B. (1980). Momentum and energy deposition in late-type stellar atmospheres and winds. *ApJ*, *242*, 260-282.
- Hayes, D. P. (1984). Variation of Betelgeuse's optical linear polarization over four consecutive observing seasons - 1979-1983. *ApJ S.*, *55*, 179-188.
- Heger, A., Jeannin, L., Langer, N., & Baraffe, I. (1997). Pulsations in red supergiants with high L/M ratio. Implications for the stellar and circumstellar structure of supernova progenitors. *A&A*, *327*, 224-230.
- Henry, G. W., Fekel, F. C., & Hall, D. S. (1995). An Automated Search for Variability in Chromospherically Active Stars. *AJ*, *110*, 2926.
- Hinkle, K. H., Lebzelter, T., Joyce, R. R., & Fekel, F. C. (2002). Velocity Observations of Multiple-Mode Asymptotic Giant Branch Variable Stars. *AJ*, *123*, 1002-1012.
- Hoefner, S. (1999). A new generation of dynamic model atmospheres for AGB stars: first results. *A&A*, *346*, L9-L12.

- Hoefner, S. (2008). Winds of M-type AGB stars driven by micron-sized grains. *A&A* , 491, L1-L4.
- Hoefner, S., Jorgensen, U. G., Loidl, R., & Aringer, B. (1998). Dynamic model atmospheres of AGB stars. I. Atmospheric structure and dynamics. *A&A* , 340, 497-507.
- Holenstein., B. D. (1993). Elliptical Polarimetry of Eleven Luminous Late-Type Variables. *PASP* , 105, 322.
- Houk, N. (1963). V1280 Sagittarii and other long-period variables with secondary period. *AJ* , 68, 253-257.
- Houk, N. (1982). *Catalogue of the two-dimensional spectral types for the HD stars, Volume 3. Declination -40 to -26*. AnnArbor: MI, Houk, 1982.
- Huang, S. -S., & Struve, O. (1960). Stellar Rotation and Atmospheric Turbulence. In J. L. Greenstein (Ed.), *Stellar Atmospheres* (p. 321). University of Chicago Press.
- Huber, D., Bedding, T. R., Stello, D., Hekker, S., Mathur, S., Mosser, B., et al. (2011). Testing Scaling Relations for Solar-like Oscillations from the Main Sequence to Red Giants Using Kepler Data. *ApJ* , 743, 143.
- Huggins, P. J., Bachiller, R., Cox, P., & Forveille, T. (1994). Neutral carbon in the circumstellar envelope of alpha Orionis. *ApJ L* , 424, L127-L130.
- Huggins, W., & Miller, W. -A. (1864). On the Spectra of Some Fixed Stars. *Royal Society of London Philosophical Transactions Series I* , 154, 413-435.
- Humphreys, R. M., & Davidson, K. (1979). Studies of luminous stars in nearby galaxies. III - Comments on the evolution of the most massive stars in the Milky Way and the Large Magellanic Cloud. *ApJ* , 232, 409-420.
- Iben, J. I. (1974). POST main sequence evolution of single stars. *Annual Review of A&A* , 12, 215-256.
- Janssen, M. (1878). M. Janssen's photographs of the Sun. *MNRAS* , 38, 202.

- Johnson, H. L., Mitchell, R. I., Iriarte, B., & Wisniewski, W. Z. (1966). Ubvrijkl Photometry of the Bright Stars. *Communications of the Lunar and Planetary Laboratory*, 4, 96.
- Josselin, E., & Plez, B. (2007). Atmospheric dynamics and mass loss process in red supergiant stars. *A&A*, 469, 671-680.
- Judge, P. G., & Stencel, R. E. (1991). Evolution of the chromospheres and winds of low- and intermediate-mass giant stars. *ApJ*, 371, 357-379.
- Kerschbaum, F., & Hron, J. (1992). Semiregular variables of types SRa and SRb - Basic properties in the visual and the IRAS-range. *A&A*, 263, 92-112.
- Kerschbaum, F., Lebzelter, T., & Lazaro, C. (2001). Multi-colour light variation of AGB stars observed with ISO. *A&A*, 375, 527-538.
- Kippenhahn, R., & Weigert, A. (1994). *Stellar Structure and Evolution*. Berlin, Heidelberg, New York: Springer-Verlag. A&A Library.
- Kiss, L. L. & Percy, J. R. (2012). Non-Mira Pulsating Red Giants and Supergiants. *JAAVSO*, 40, 528.
- Kiss, L. L., Szabo, G. M., & Bedding, T. R. (2006). Variability in red supergiant stars: pulsations, long secondary periods and convection noise. *MNRAS*, 372 (4), 1721-1734.
- Kiss, L. L., Szatmary, K., Cadmus, R. R., & Mattei, J. A. (1999). Multiperiodicity in semiregular variables. I. General properties. *A&A*, 346, 542-555.
- Kiss, L. L., Szatmary, K., Szabo, G., & Mattei, J. A. (2000). Multiperiodicity in semiregular variables. II. Systematic amplitude variations. *A&A S*, 145, 283-292.
- Klueckers, V. A., Edmunds, M. G., Morris, R. H., & Wooder, N. (1997). Reality and the speckle imaging of stellar surfaces - II. The asymmetry of Alpha Orionis. *MNRAS*, 284, 711-716.

Kramida, A., Ralchenko, Yu., Reader, J., & NIST ASD Team. (2012). *NIST Atomic Spectra Database (version 5.0)*. Available: <http://physics.nist.gov/asd>. National Institute of Standards and Technology, Gaithersburg, MD.

Kron, G. E. (1947). The Probable Detecting of Surface Spots on AR Lacertae B. *PASP*, 59, 261.

Kron, G. E. (1952). A Phtotelectric Study of the Dwarf M Eclipsing Variable YY Geminorum. *ApJ*, 115, 301.

Leblanc, F. (2010). *An Introduction to Stellar Astrophysics*. Wiley.

Lebzelter, T., & Hinkle, K. H. (2002). Velocity variability of semiregular variables and irregular variables. *A&A*, 393, 563-571.

Lebzelter, T., & Kiss, L. L. (2001). Monitoring of LPVs with an automatic telescope. II: A comparison of APT data and visual observations. *A&A*, 380, 388-396.

Lebzelter, T., Kerschbaum, F., & Hron, J. (1995). Semiregular variables of types SRa and ARb. Variability classification in the GCVS. *A&A*, 298, 159.

Lebzelter, T., Kiss, L. L., & Hinkle, K. H. (2000). A comparison of light and velocity variations in semiregular variables. *A&A*, 361, 167-174.

Lee, T. A. (1970). Photometry of high-luminosity M-type stars. *ApJ*, 162, 217.

Lenz, P., & Breger, M. (2005). Period04 User Guide. *Comminications in Asteroseismology*, 146, 53-136.

Linsky, J. L., & Haisch, B. M. (1979). Outer atmospheres of cool stars. I - The sharp division into solar-type and non-solar-type stars. *ApJ L*, 229, L27-L32.

Llyod Evans, T. (1975). Red Variables of the Halo and Globular Clusters (review). In V. E. Sherwood, & L. Plaut (Ed.), *Variable Stars and Stellar Evolution*. 67, p. 531. IAU Symposium.

- Lobel, A., & Dupree, A. K. (2000). Modeling the Variable Chromosphere of alpha Orionis. *ApJ*, 545, 454-474.
- Lunt, J. (1916). On the orbits of the spectroscopic binaries alpha Orionis and alpha Scorpii. *ApJ*, 44, 250-259.
- Maas, T., Van Winckel, H., & Waelkens, C. (2002). RU Cen and SX Cen: Two strongly depleted RV Tauri stars in binary systems. The RV Tauri photometric b phenomenon and binarity. *A&A*, 386, 504-516.
- Maeder, A., & Meynet, G. (2012). Rotating massive stars: From first stars to gamma ray bursts. *Reviews of Modern Physics*, 84, 25-63.
- Mahler, T. A., Wasatonic, R., & Guinan, E. F. (1997). Radius and Luminosity Variations of Mira from Wing Near-Ir Photometry. *Information Bulletin on Variable Stars*, 4500, 1.
- Mais, D. E., Stencel, R. E., & Richards, D. (2004). Automated Photometry, period analysis and flare-up constraints for selected Mira Variable Stars. In *AAS Meeting Abstracts*, 36, p. 1428. Bulletin of the AAS.
- Mallik, S. V. (1993). CCD observations of the H-alpha line in late G and K supergiants and their interpretation. *ApJ*, 402, 303-310.
- Marsh, K. A., Bloemhof, E. E., Koerner, D. W., & Ressler, M. E. (2001). Mid-Infrared Images of the Circumstellar Dust around alpha Scorpii. *ApJ*, 548, 861-867.
- Mason, B. B., Wycoff, G. L., Hartkopf, W. I., Douglass, G. G., & Worley, C. E. (2001). The 2001 Naval Observatory Double Star CD-ROM. I. The Washington Double Star Catalog. *AJ*, 122, 3466-3471.
- Massey, P. (2003). Observational constraints on massive star evolution. In K. v. Hucht, A. Herrero, & C. Esteban (Ed.), *A Massive Star Odyssey: From Main Sequence to Supernova*. 212, p. 316. IAU Symposium.

Massey, P., Plez, B., Levesque, E. M., Olsen, K. A., Clayton, G. C., & Josselin, E. (2005). The Reddening of Red Supergiants: When Smoke Gets in Your Eyes. *ApJ*, *634*, 1286-1292.

Mattei, J. A. (1983). AAVSO Report 38: Observations of Long Period Variables. *American Association of Variable Stars Observers Report*, *38*, 1.

Mattei, J. A., Foster, G., Hurwitz, L. A., Malatesta, K. H., Willson, L. A., & Mennessier, M. O. (1997). Classifications of Red Variables. In R. M. Bonnet, E. Hog, L. E. P. L. Bernacca, A. Blaauw, C. Turon, J. Kovalevsky, et al. (Ed.), *Hipparcos - Venice '97*. *402*, pp. 269-274. ESA Special Publications.

Mauron, N., & Josselin, E. (2011). The mass-loss rates of red supergiants and the de Jager prescription. *A&A*, *526*, A156.

Meynet, G., Georgy, C., Hirschi, R., Maeder, A., Massey, P., Przybilla, N., et al. (2011). Red Supergiants, Luminous Blue Variables and Wolf-Rayet stars: the single massive star perspective. *Bulletin de la Societe Royale des Sciences de Liege*, *80*, 266-278.

Michelson, A. A., & Pease, F. G. (1921). Measurement of the diameter of alpha Orionis with the interferometer. *ApJ*, *53*, 249-259.

Mohamed, S., Mackey, J., & Langer, N. (2012). 3D simulations of Betelgeuse's bow shock. *A&A*, *541*, A1.

Morris, S. L. (1978). The ellipsoidal variable stars. *ApJ*, *295*, 143-152.

Nave, G., Johansson, S., Learner, R. C., Thorne, A. P., & Brault, J. W. (1994). A new multiplet table for Fe I. *ApJ S*, *94*, 221-459.

Nicholls, C. P., Wood, P. R., Cioni, M. R., & Soszynki, I. (2009). Long Secondary Periods in variable red giants. *MNRAS*, *399*, 2063-2078.

Nicolet, B. (1978). Catalogue of homogeneous data in the UBV photoelectric photometric system. *A&A S*, *34*, 1-49.

- Nordlund, A., & Stein, R. F. (1989). Simulating Magnetoconvection. In R. J. Rutten, & G. Severino (Ed.), *NATO ASIC Proc. 263: Solar and Stellar Granulation*, (p. 453).
- Nordlund, A., & Stein, R. F. (1999). Convection Simulations. In A. Gimenez, E. F. Guinan, & B. Montesinos (Ed.), *Stellar Structure: Theory and Test of Convective Energy Transport. 173*, p. 91. Astron. Society of the Pacific Conf. Series.
- Nordlund, A., & Stein, R. F. (2001). Solar Oscillations and Convection. I. Formalism for Radial Oscillations. *ApJ*, *546*, 576-584.
- Olah, K., Hall, D. S., Boyd, L. J., Genet, R. M., & Fried, R. E. (1986). Starspots on HK Lacertae. *Ap Lett*, *25*, 133-138.
- Olah, K., Kovari, Z., Bartus, J., Strassmeier, K. G., Hall, D. S., & Henry, G. W. (1997). Time-series photometric SPOT modeling. III. Thirty years in the life of HK Lacterae. *A&A*, *321*, 811-821.
- Olivier, E. R., & Wood, P. R. (2003). On the Origin of Long Secondary Periods in Semiregular Variables. *ApJ*, *584*, 1035-1041.
- Ostlie, D. A., & Cox, A. N. (1986). A linear survey of the Mira variable star instability region of the Hertzsprung-Russell diagram. *ApJ*, *311*, 864-872.
- Paczynski, B. (1970). Evolution of Single Stars. I. Stellar Evolution from Main Sequence to White Dwarf or Carbon Ignition. *ACTAA*, *20*, 47.
- Payne-Gaposchkin, C. (1954). The Red Variable Stars. *Annals of the Harvard College Observatories*, *113*, 189-208.
- Percy, J. R., & Desjardins, A. (1996). Pulsation Mode Switching in the Small-Amplitude Red Variable W Bootis. *PASP*, *108*, 847.
- Percy, J. R., & Mattei, J. A. (1993). The AAVSO database of variable star observations. *ApSS*, *210*, 137-138.

Percy, J. R., & Parkes, M. (1998). Pulsation Modes in Small-Amplitude Red Variable Stars. *PASP*, *110*, 1431-1433.

Percy, J. R., & Terziev, E. (2011). Studies of "Irregularity" in Pulsating Red Giants. III. Many More Stars, an Overview, and Some Conclusions. *JAAVSO*, *39*, 1.

Percy, J. R., Desjardins, A., Yu, L., & Landis, H. J. (1996). Small Amplitude Red Variables in the AAVSO Photometric Program: Light Curves and Periods. *PASP*, *108*, 139.

Percy, J. R., Wilson, J. B., & Henry, G. W. (2001). Long-Term VRI Photometry of Small-Amplitude Red Variables. I. Light Curves and Periods. *PASP*, *113* (786), 983-996.

Perryman, M. A. (1997). The HIPPARCOS and TYCHO catalogues. Astrometric and photometric star catalogues derived from the ESA HIPPARCOS Space Astrometry Mission. In M. A. Perryman, & ESA (Ed.), *ESA Special Publications*, *1200*.

Plaskett, H. H. (1936). Solar granulation. *MNRAS*, *96*, 402.

Press, W. H. (1978). Flicker noises in astronomy and elsewhere. *Comments on Astrophysics*, *7*, 103-119.

Pryor, C. P., Latham, D. W., & Hazen, M. L. (1988). A search for spectroscopic binaries in the globular cluster M3. *AJ*, *96*, 123-138.

Pugh, T., & Gray, D. F. (2013). On the Six-year Period in the Radial Velocity of Antares A. *AJ*, *145*, 38.

Rabello-Soares, M. C., Roca Cortes, T., Jimenez, A., Andersen, B. N., & Appourchaux, T. (1997). An estimate of the solar background irradiance power spectrum. *A&A*, *318*, 970-974.

Reimers, D., Hagen, H. J., Baade, R., & Braun, .. K. (2008). The Antares emission nebula and mass loss of alpha Scorpii A. *A&A*, *491*, 229-238.

- Renzini, A., Cacciari, C., Ulmschneider, P., & Schmitz, F. (1977). Theoretical chromospheres of late type stars. I - Acoustic energy generation. *A&A* , 61, 36-45.
- Rest, A., Prieto, J. L., Walborn, N. R., Smith, N., Bianco, F. B., Chornock, R., et al. (2012). Light echoes reveal an unexpectedly cool eta Carinae during its nineteenth-century Great Eruption. *Nature* , 7385, 375-378.
- Richichi, A., & Lisi, F. (1990). A new accurate determination of the angular diameter of Antares. *A&A* , 230, 355-362.
- Rupperecht, G., Pepe, F., Mayor, M., Queloz, D., Bouchy, F., & al., e. (2004). The exoplanet hunter HARPS: performance and first results. In A.-F.-M. Moorwood, & M. Iye (Ed.), *Society of Photo-Optical Instrumentation Engineers (SPIE) Conference Series*, 5492, pp. 148-159.
- Ryan, S. G., & Norton, A. J. (2010). *Stellar Evolution and Nucleosynthesis*. Cambridge University Press, 2010.
- Samus, N. N., Kazarovets, E. V., Pastukhova, T. M., & Durlevich, O. V. (2012). General Catalogue of Variable Stars - GCVS. *VizieR On-line Data Catalog: B/gcvs* .
- Schroder, K.-P., & Cuntz, M. (2007). A critical test of empirical mass loss formulas applied to applied giants and supergiants. *A&A* , 465, 593-601.
- Schroder, K. P., & Reimers, D. (1989). A study of ultraviolet of Zeta Aurigae/VV Cephei systems. XI - 22 Vulpeculae: IUE observations of its extended chromosphere and wind with spacial resolution. *A&A* , 208, 223-229.
- Schwarzschild, M. (1975). On the scale photometric convection in red giants and supergiants. *ApJ* , 195, 137-144.
- Secchi, A. (1866). Spectrum of alpha Orionis. *MNRAS* , 26, 274.
- Shine, R., Strous, L., Simon, G., Berger, T., Hurlburt, N., Tarbell, T., et al. (1997). Comparison of Granulation Correlation Tracking (CT) and Feature Tracking (FT) Results

from SOHO/MDI and the Swedish Vacuum Solar Telescope on La Palma. *AAS Solar Physics Division Meeting #28. 29*, p. 904. Bulletin of the American Astronomical Society.

Smartt, S. J., Crockett, R. M., Eldridge, J. J., & Maund, J. R. (2008). The Progenitors Stars of Core-Collapse Supernovae. In F. Bresolin, P. A. Crowther, & J. Puls (Ed.), *IAU Symposium, 250*, pp. 201-208.

Smith, H. A. (1995). *Rr-Lyrae Stars*.

Smith, M. A., Patten, B. M., & Goldberg, L. (1989). Radial-velocity variations in Alpha Ori, Alpha Sco, and Alpha Her. *AJ*, *98*, 2233-2248.

Smith, N., Hinkle, K. H., & Ryde, N. (2009). Red Supergiants as Potential Type II_n Supernova Progenitors: Spatially Resolved 4.6 μm CO Emission Around VY CMa and Betelgeuse. *AJ*, *137*, 3558-3573.

Spencer-Jones, H. (1928). The radial velocity variations of a Orionis and a Scorpii. *MNRAS*, *88*, 660.

Stothers, R. (1969). On the Pulsation Hypothesis of Massive Red Supergiants. *ApJ*, *156*, 541.

Stothers, R. B. (2010). Giant Convection Cell Turnover as an Explanation of the Long Secondary Periods in Semiregular Red Variable Stars. *ApJ*, *725*, 1170-1174.

Stothers, R., & Leung, K. C. (1971). Luminosities, masses and periodicities of massive red supergiants. *A&A*, *10*, 290-300.

Strasmeier, K., & Bopp, B. W. (1992). Time-series photometric SPOT modeling. I - Parameter study application to HD 17433 = VY ARIETIS. *A&A*, *259*, 183-197.

Tuthill, P. G., Haniff, C. A., & Baldwin, J. E. (1997). Hotspots on late-type supergiants. *MNRAS*, *285*, 529-539.

- Ulmschneider, P. (1998). Heating of Chromospheres and Coronae. *Highlights of Astronomy*, *11*, 831.
- van Leeuwen, F. (2007). Validation of the new Hipparcos reduction. *A&A*, *474*, 653-664.
- van Loon, J. T., Cioni, M. R., Zijlstra, A. A., & Loup, C. (2005). An empirical formula for the mass-loss rates of dust-enshrouded red supergiants and oxygen-rich Asymptotic Giant Branch stars. *A&A*, *438*, 273-289.
- Van Winckel, H. Waelkens, C., Fernie, J. D., & Waters, L. B. F. M. (1999). The RV Tauri phenomenon and binarity. *A&A*, *343*, 202-212.
- Vogt, S. S. (1981). Starspots - A review of observations and theory. In L. E. Cram, & J. H. Thomas (Ed.), *The Physics of Sunspots*, (pp. 455-479).
- Vogt, S. S., Penrod, G. D., & Hatzes, A. P. (1987). Doppler images of rotating stars using maximum entropy image reconstruction. *ApJ*, *321*, 496-515.
- Wallerstein, G. (2002). The Cepheids of Population II and Related Stars. *PASP*, *114*, 689-699.
- Walraven, T., Muller, A. B., & Oosterhoff, P. T. (1958). Photoelectric magnitudes and colours at maximum brightness for 184 Cepheids. *BAN*, *14*, 81.
- Wesselink, A. J. (1946). The observations of brightness, colour and radial velocity of delta Cephei and the pulsation hypothesis. *BAN*, *10*, 91.
- Weymann, R. (1962). Physical Conditions in the Circumstellar Envelope of alpha Orionis. *ApJ*, *136*, 844.
- Willson, L. A., & Marengo, M. (2012). Miras. *JAASO*, *40*, 516.
- Wilson, R. W., Baldwin, J. E., Buscher, D. F., & Warner, P. J. (1992). High-resolution imaging of Betelgeuse and Mira. *MNRAS*, *257*, 369-376.

Wilson, R. W., Dhillon, V. S., & Haniff, C. A. (1997). The changing face of Betelgeuse. *MNRAS*, *291*, 819.

Winters, J. M., Fleischer, A. J., Le Bertre, T., & Sedlmayr, E. (2000). Optical Appearance of Dynamical Models for Circumstellar Dust Shells around Long-Period Variables: AFGL 3068. In R. F. Wing (Ed.), *The Carbon Star Phenomenon* (p. 590). IAU Symposium.

Wood, P. R. (1995). Mira Variables: Theory versus Observation. In R. S. Stobie, & P. A. Whitelock (Ed.), *IAU Colloq. 155: Astrophysical Applications of Stellar Pulsation*. 83, p. 127. Astron. Society of the Pacific Conf. Series.

Wood, P. R. (2000). Variable red giants in the LMC: Pulsating stars and binaries? *PASA*, *17*, 18-21.

Wood, P. R., Olivier, E. A., & Kawaler, S. D. (2004a). Long Secondary Periods in Pulsating Asymptotic Giant Branch Stars: An Investigation of their Origin. *ApJ*, *604*, 800-816.

Wood, P. R., Olivier, E. A., & Kawaler, S. D. (2004b). The long secondary periods in semi-regular variables. In D. W. Kurtz, & K. R. Pollard (Ed.), *IAU Colloq. 193: Variable Stars in the Local Group*. 310, p. 322. Astron. Society of the Pacific Conf. Series.

Wood, P., Alcock, C., Allsman, R. A., Alves, D., Axelrod, T. S., Becker, A. C., et al. (1999). MACHO observations of LMC red giants: Mira and semi-regular pulsators, and contact and semi-detached binaries. In T. L. Bertre, A. Lebre, & C. Waelkens (Ed.), *Asymptotic Giant Branch Stars*. 191, p. 151. IAU Symposium.

Wood, R. W. (1946). Large diffraction gratings for Schmidt telescopes. *PASP*, *10*, 218.

Worley, C. E., & Heintz, W. D. (1983). Fourth catalog of orbits of visual binary stars. *Publications of the U.S. Naval Obs. 2nd Series*, *24*, 1.

Wright, W. H. (1906). The variable radial velocity of Antares. *Lick Obs. Bulletin*, *4*, 98.

Young, J. S., Baldwin, J. E., Boysen, R. C., Haniff, C. A., Lawson, P. R., Mackay, C. D., et al. (2000). New views of Betelgeuse: multi-wavelength surface imaging and implications for models of hotspot generation. *MNRAS*, *315*, 635-645.

Appendices

Appendix A: The Richardson Image Slicer

[Much of the information in this description comes from Richardson (1966, 1968) and Gray (2005).]

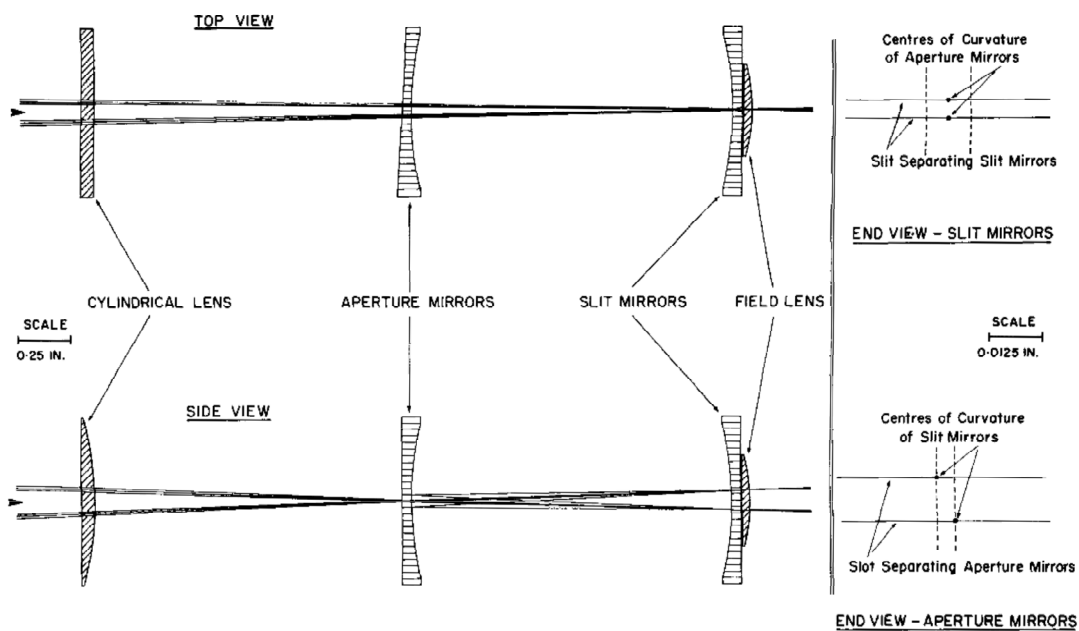


Figure A 1: The optical layout of an image slicer. Center rays pass through the slit without reflection. The edge rays are reflected back and forth between the mirrors, only the final reflection is shown in the side view. From Richardson (1966)

An image slicer can be used effectively when the disk image is wider, but not longer, than the entrance slit to the spectrograph. Under these circumstances the image slicer allows more light to be passed into the spectrograph than a naked slit would. A Richardson image slicer results in slices which are constant in length and illuminate the

full length of the slit. The result is cleaner spectra (less scattering) and spectra whose dispersion does not vary with seeing. As is shown in Figure A1, the image slicer is composed of a series of lenses and mirrors that focus and reflect the light in such a way that only the light which will fill the slit is passed through. The remaining light, rather than being allowed to scatter into the spectrograph is reflected and refocused again until it too falls incident on the gap between the slit mirrors and thus is allowed to pass into the spectrograph.

The light enters through a cylindrical lens, this lens split the beam into a horizontal and a vertical component. The horizontal component passes through the slot separating the aperture mirrors and is either reflected by the slit mirrors or focused onto the grating by the field lens. The purpose of the multiple reflections is to direct light to regions of the grating that were not illuminated by the unreflected light. The aperture and slit mirrors have a common radius of curvature, by which they are separated. Their centers of curvature (see Figure A1) are arranged such that light reflected onto the aperture mirror does not escape from the image slicer and that light reflected on the slit mirror is reflected through a point at the very edge of that mirror. Thus, some light is allowed to pass onto the grating and the rest is reflected again back to the aperture mirror. Each slice that successfully passes through to the grating is superimposed upon the previous slices.

Appendix B: Fourier analysis of Spectral Lines

Many line broadening mechanisms cause subtle changes in spectral line shapes. In cases where this signal varies in different sections of the line (i.e. Zeeman broadening and line asymmetries) modeling of spectral lines and direct comparison in the wavelength domain are necessary. However, when one is dealing with signal that is distributed almost equally across a spectral line, it is advantageous to study the line in the Fourier domain. However, the real advantage of using the Fourier domain is that; 1) the instrumental profile can be easily removed from the data and 2) the noise level of the data is easily recognizable. Here we review the technique of Fourier analysis.

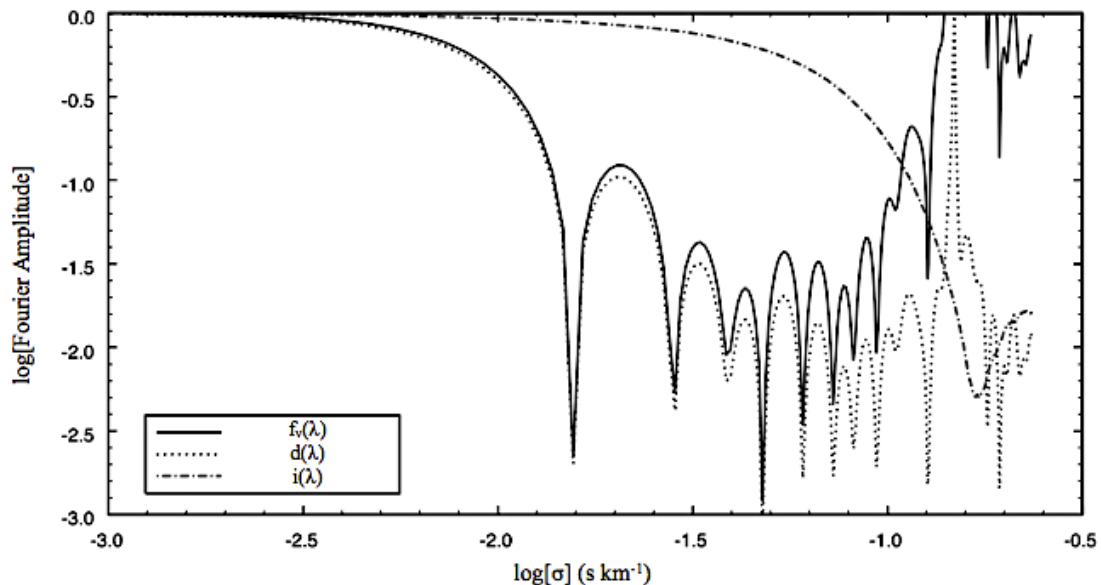


Figure A 2: An example of instrumental profile division in Fourier space using a mean spectral line from the solar-like dwarf star β Delphini. The spike at 0.14 s/km (-0.85 on the log scale) is an artifact from the thermal profile removal. The solid line is the Fourier spectrum. Note the noise amplification above 0.04 s/km (-1.40 on the log scale) caused by the division.

Measured spectral lines consist of both a stellar component and an instrumental component. The instrumental profile acts to smear the stellar lines and is treated as a convolution. If $D(\lambda)$ is the measured spectrum, $F_v(\lambda)$ is the original spectrum and $I(\lambda)$ is the instrumental profile, then:

$$D(\lambda) = I(\lambda) * F_v(\lambda). \quad \text{Equation A 1}$$

In the Fourier domain this leads to:

$$d(\lambda) = i(\lambda) \cdot f_v(\lambda), \quad \text{Equation A 2}$$

a simple product. Thus, the reduction in the amplitude of Fourier spectrum side-lobes due to instrumental smearing can be undone by a division. Since the instrumental profile is sharp compared to the spectral lines, in Fourier space it is much broader [units transform from \AA to cycles/\AA (or from km/s to s/km)], but falls off quickly at high frequencies. So, while this division undoes the instrumental smearing at low frequencies at high frequencies it acts to amplify the noise, see Figure A2 for example. Because of this it is normal practice to use a noise filter prior to spectral reconstruction, such that the high-frequency amplified noise is excluded from the final signal, giving:

$$f_v(\lambda) = d(\lambda) \phi(\lambda) / i(\lambda), \quad \text{Equation A 3}$$

where $\Phi(\lambda)$ is the noise filtering function. For details on the selection and computation of noise filters see Gray (2005) Chapter 12.

There are a variety of different broadening mechanisms that can be easily identified in the Fourier domain. Figure A3 shows the extreme difference caused by rotation dominated or macroturbulence dominated spectral lines and the minor difference introduced by microturbulence. Thus we see that in the Fourier domain it is very simple to distinguish between the two major line broadeners (rotation and macroturbulence). Modeling allows us to gain a handle on a number of stellar parameters; for example, if rotation dominates the lines, then the position of the first zero is a measure of the $v \sin i$, further the side-lobe

amplitudes and widths can be fit to deduce the value of the macroturbulence dispersion, and in cases of very good data, third order effects can be measured. In the case of macroturbulence dominated stars, fitting is not so simple and in general one finds a series of fits corresponding to the same ratio of $\zeta_{RT} = v \sin i$ and so actual numbers are only achievable if we have another way of estimating the $v \sin i$. In Figure A3 we show a typical Fourier transform with its model fit and the values determined from the fit. A full review of the techniques, advantages and uses of the Fourier analysis can be found in Gray (2005) and in Gray (1975).

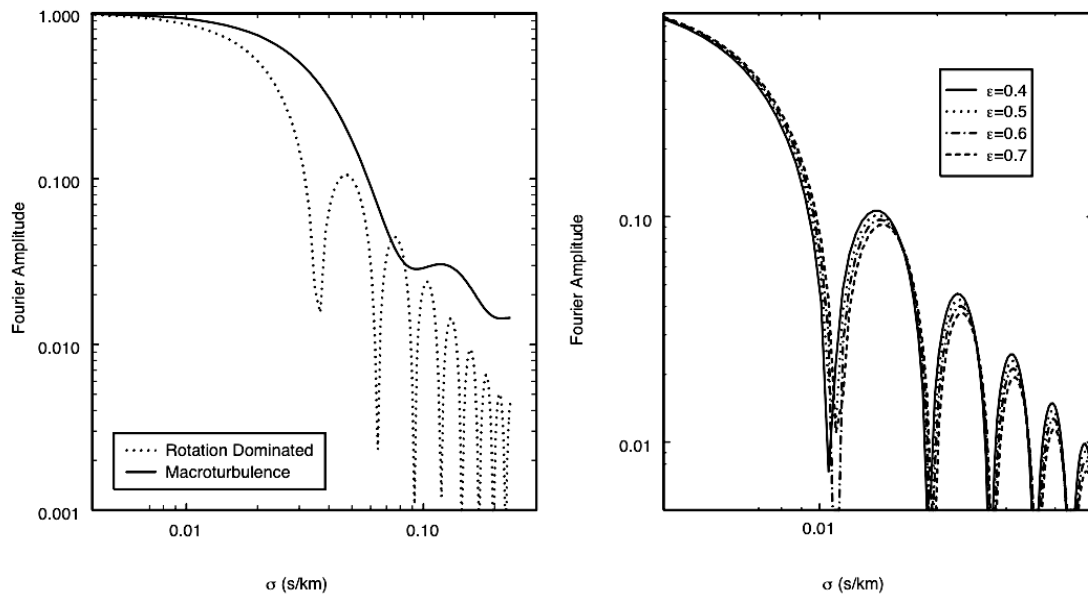


Figure A 3: Fourier transforms of model spectral lines. *Left* – Shows the difference between rotationally dominated lines and macroturbulence dominated lines. Note the distinct peaks exhibited by the rotationally dominated line. *Right* – Shows the variation in the lobe widths with increasing limb darkening.

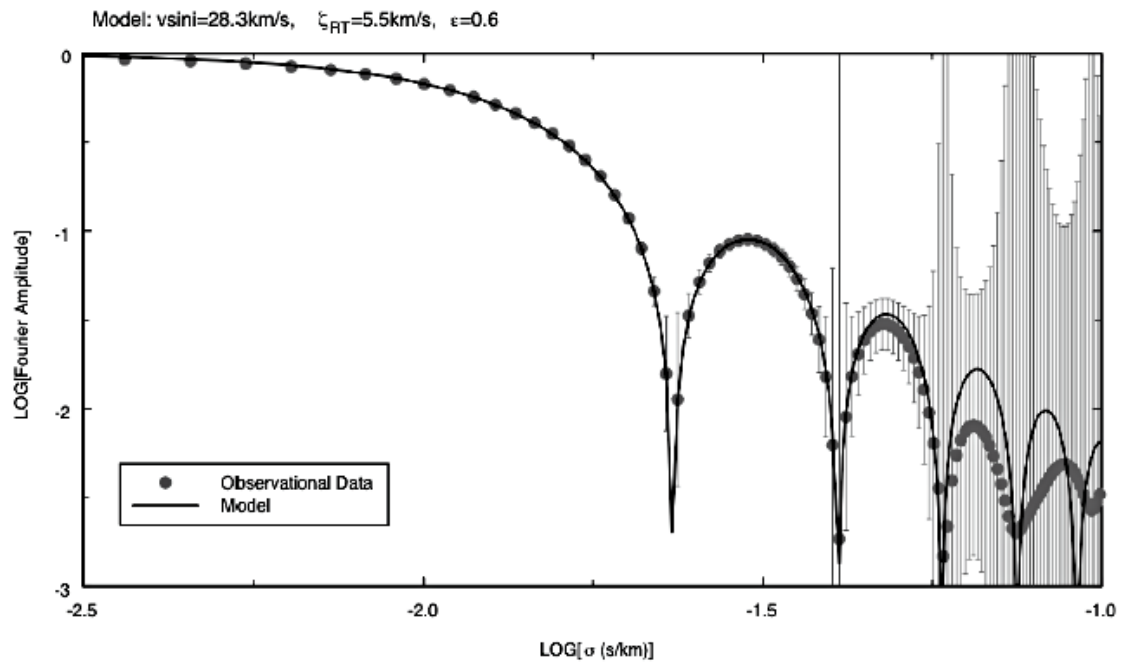


Figure A 4: Best fit model for the F8 IV star θ Draconis. From the best fit model we determine a $v \sin i$ of 28.3 ± 0.1 km/s and ζ_{RT} of 5.5 ± 0.5 km/s, both of these values compare well with those published by Gray (1982). Error bars are inversely proportional to the height above the noise level.

Appendix C: Spectral Line Bisectors

Spectral line bisectors are a valuable tool in the observation and analysis of spectral line asymmetries since they magnify and simplify the shape changes. The computation of a bisector is a conceptually trivial task.

1. The spectral line is sectioned into horizontal slices of equal depth. Typically one desires between 10 and 40 bisector points, thus 10-40 horizontal slices are used. While there is no requirement that these sections be of equal depth, the computation is simplified by making them so.
2. Secondly, within each horizontal section, we determine the wavelength, velocity or pixel position of the line flux on both the blue and red edges of the line for a single flux depth. Figure A5 shows five such pairs of flux points for the synthetic spectral line from Figure 19.
3. Midpoints of the computed horizontal lines connecting each flux pair are computed. These midpoints have the same normalized flux as the pairs which they are computed from and a wavelength, velocity, or pixel number that corresponds to the mean wavelength, velocity, or pixel number of the blueward and redward points.
4. The wavelength, velocity or pixel axis is magnified to high-light the shape.

For the bisectors found in publications that stem from observations made at the Elginfield Observatory, such as those found in Gray (2008) we use the Fortran algorithm named BISM which is supplied by D. F. Gray. This algorithm outputs a number of measurements of the computed bisector in addition to the bisector itself. A typical interface screen is shown in Figure A6.

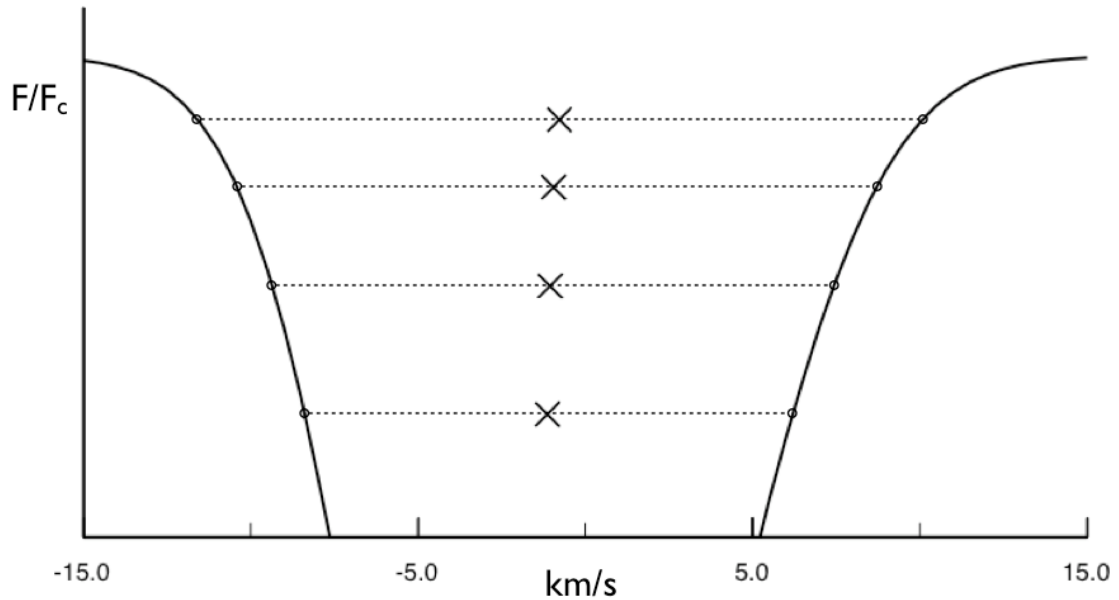


Figure A 5: Four pairs of flux points and their corresponding bisector point. Each pair is connected with a dashed line. The spectral line used is synthetic and can be seen in full in Figure 19.

In the input file BIIN.sc one places the line for which a bisector is to be computed in column format, or a list of file names if multiple lines are required for which the same velocity dispersion can be used. Within the key file BIkeys one is able to set three depth positions (hi, mid, and low). Providing that each of these is within the line depth, upper and lower velocity spans will be computed using those as the reference positions. Additionally, BISM outputs the line core position and the bisector position at one other selectable line depth position. In this case, the depth is chosen as a fraction of the line-depth. This allows us to select a constant position within lines of varying depth. In the case shown in Figure A6 a single line was input in a two column format on a velocity scale. The core position is given in km/s, the velocity spans and the velocity at a depth of 80% of the line depth are given in m/s. A list of the output files is given at the end of the interface. When more than one line is computed each bisector is placed in different file, the names of which are given to the algorithm through the BNout.sc file.

```

----- BISM is in,-----
The input file is BIIN.sc.
  It has file names when running as a batch file.
  It has a line profile in it when running one line.
The parameter-key input file is BIkeys.
The output name file for batch mode is: BNOUT.sc.

--- Reading BIIN.sc (single file mode).
  There are 138 points.
  Velocities read in with profile.

      Tapering red wing to continuum.
      Tapering red wing to continuum.
      Tapering red wing to continuum.
      Tapering red wing to continuum.
      Tapering red wing to continuum.
      Tapering red wing to continuum.
      Tapering red wing to continuum.
      Tapering red wing to continuum.
  Bisector core is at  -5.422

Type <RETURN> for next page:

Velocity Spans:
  Dhi =   0.820  Dmid =   0.710  Dlow =   0.600
  VSlow =   525.  VShi =   430.  Curv =  -95.

      frac = 0.80  Dfrac = 0.6616  Vfrac =  -4947.44
  Bisector is in file Blout.SC.
  Velocity spans & velocities are in VS.sc.
  Core points are in CP.sc

```

Figure A 6: Screen shot of the BISM interface as seen run in a bash shell.

From our bisectors we have a line-core position (depth and velocity etc), an upper and lower velocity span, a curvature and a set fractional depth position. The curvature measure is not particularly important given the subject of this thesis, the others however could be used to provide all the measurement used in this thesis provided that bisectors could be computed and where computed for the required lines. The curvature gives an idea of the amount of shape change that is seen between bisectors and in a thesis such as this is most useful for determining the temporal changes in line shape. In less variable stars, it can also be used to determine the bisector trends as a function of position in the HR diagram, such as those demonstrated in Figure 24.

Curriculum Vitae

Name: Teznie Pugh

Post-secondary Education and Degrees: University of York
York, North Yorkshire, United Kingdom
2004-2006 B.Sc. Hons.

Western University
London, Ontario, Canada
2007-2008 M. Sc.

Western University
London, Ontario, Canada
2008-2013 Ph.D.

Honours and Awards: Western Graduate Research Scholarship (2007-2012)

Western TA Award of Excellence (2012)

CASCA Conference Travel Grant (2012)

Related Work Experience Teaching Assistant & Research Assistant
Western University
2007-2013

Publications:

Pugh, T. & Gray, D. F. 2013, *On the Six Year Period in the Radial Velocity of Antares A*, AJ, 145, 38.

Gray, D. F. & Pugh, T. 2012, *The Third Signature of Granulation in Bright-Giant and Supergiant Stars*, AJ, 143,92.

Talks:

Pugh, T. *The Variability of Antares A – A Spectroscopic Review*, Invited talk, Queen's University, Kingston, Ontario. September 2012.

Pugh, T. & Gray, D. F. *The Third Signature of Granulation in Bright-Giant and Supergiant Stars*. CASCA Meeting, University of Calgary, Calgary, Alberta. June 2012.

Posters:

Pugh, T. & Gray, D. F. *The Variability of a Scorpii A*. CASCA Meeting, Western University, London, Ontario. June 2011.

Pugh T. *Spectral Analysis of Late-Type Supergiants in Close Binary Systems*. CASCA Meeting. Toronto, Ontario. June 2009.